المملكة العربية السعودية
مدينة الملك عبدالعزيز للعلوم والتقنية
الإدارة العامة لبرامج المنح البحثية

المشروع البحثي التطبيقي أت -٢٣ -٤٠

التراكيب القشرية والوشاح العلوي تحت الدرع العربي والبحر الأحمر

التقرير النهائي المنقح

أ.د. عبدالله بن محمد العمري (الباحث الرئيسي)
أ.د. طارق بن علي الخليفة (الباحث المشارك)

جامعة الملك سعود

ربيع الثاني ١٤٢٨ هـ - مايو ٢٠٠٧ م

Kingdom of Saudi Arabia
King Abdulaziz City for Science and Technology
General Directorate of Research Grants Programs

AR – 23 – 40

REVISED FINAL REPORT

CRUSTAL AND UPPER MANTLE STRUCTURES BENEATH THE ARABIAN SHIELD AND RED SEA

Dr. Abdullah M. Al-Amri, KSU (P-I)
Dr. Tariq A. Alkhalifah, KACST (CO-I)

KING SAUD UNIVERSITY

RABI II 1428 – MAY 2007

ACKNOWLEDGMENTS

This is the final report of the research project AR-23-40. The authors would like to express their thanks and gratitude to King Abdulaziz City for Science and Technology for funding this project. This work would not have been possible without the generous assistance of KACST and KSU.

Dr. Arthur Rodgers and Andrew Nyblade, the project consultants, whose expert guidance and continuing advice made this work possible. Their willingness to devote their time greatly facilitated the completion of the project. We owe them a deep debt of gratitude and a great deal of thanks.

Finally and most importantly, we would like to extend our sincerest thanks to Dr. Samantha Hansen, Hrvohe Tkalcic, Yongchoel Park and Mohammed Fnais who performed tomographic images and receiver functions and to Moustafa Hameda from KACST and Ahmed R. Khalil from KSU for collecting earthquake data.

الخـــلاصـــه

يشتمل التقرير النهائي المنقح من المشروع البحثي التطبيقي أت-٢٣-٤٠ على نتائج التقارير الدورية الثلاثة السابقة بالإضافة إلى نتائج المرحلة النهائية من هذه الدراسة. تعتبـــر منطقـــة الدرع العربي والبحر الأحمر من الأماكن القليلة في العالم التي خضعت لشد قاري نشط وتكون قشرة بحرية حديثة. وعلى الرغم من قلة النشاط الزلزالي في معظم مناطق المملكة وخاصـــة الدرع العربي والمسطح العربي إلا أن قربها من المناطق النشطة زلزاليًا في إيران وتركيا من ناحية الشمال الشرقي والبحر الأحمر والدرع العربي من جهة الغرب والجنوب الغربي وصدع البحر الميت التحولي شمالاً يتطلب دراسة التراكيب القشرية تحت الدرع العربي والبحر الأحمر للإستفادة منها في تحديد مواقع الزلازل بدقة عاليه وتحديد مناطق الخطر الزلزالي المحتمل .

تهدف هذه الدراسة إلى تحديد تراكيب السرع السيزمية للقشرة والجزء العلوي مـــن الوشـــاح تحت هذه المنطقة بإستخدام المعلومات الزلزالية واسعة المدى والمسجلة على شبكة الرصـــد الزلزالي التابعة لمدينة الملك عبدالعزيز للعلوم والتقنية. تـــشتمل الـــشبكة علـــى ٣٧ محطـــة زلزالية معظمها يتركز في الدرع العربي معطية نموذج ممتاز لدراسة الدرع العربـــي والبحـــر الأحمر. وتتميز محطات هذه الشبكه بقدرتها العاليه على إلتقاط الإشارات الزلزاليـــه المحليـــة والاقليميه وهذا يعود إلى هدوء مواقع المحطات الحقليه.

قامت هذه الدراسة بإجراء تقنيات زلزالية حديثة على معلومات الشبكة ومن هذه التقنيات التي تم إجراؤها النمذجة الثلاثية البعد Tomography للمسارات الموجية الطولية و القصيرة للزلازل البعيدة المدى بإستخدام طريقة المضاهاة المتقاطعة متعددة القنوات MCCC والتي أعطت صورة واضحة image للسرع الطولية والقصيرة للجزء العلوي من الوشاح والمرتبطة بالتغيرات الحرارية. أما النمذجة الثلاثية البعد للموجات الإقليمية المنكسرة من الموهو P_n فقد أستفيد منها في رسم تراكيب الموجات التضاغطية للوشاح الضحل.

تمت نمذجة الموجات الطولية البعيدة المدى بواسطة دالة المستقبل Receiver Functions لتقدير عدم التوافق بين القشرة والجزء العلوي من الوشاح. تم تقدير دالة المستقبل من بيانات الشكل الموجي العالية الدقة من السجلات الزلزالية واسعة المدى ثلاثية الأبعاد والتي بلغ قدرها الزلزالي أكبر من 5.8 والمسافة الزلزالية مابين ٣٠و٩٠ درجة.

تم في هذه الدراسة إستخدام الطرق متعددة المراحل MSA4 وذلك لنمذجة منحنيات تشتت السرع الجماعية السطحية (من ٧ إلى١٠٠ ثانية لموجات ريلي ومن٢٠ إلى٧٠ ثانية لموجات لوف) مع دوال المستقبل لتحديد تراكيب سرع الغلاف الصخري. تتكون الطريقة من أربع مراحل وتعتمد هذه الطريقة على بحث شبكي أولي لتركيب قشري بسيط وبعد ذلك تستخدم الطرق العكسية وبحث شبكي اخر لسرع موجات القص في الوشاح وأخيرا تم تطبيق

النمذجة التقدمية لتحليل الإختلاف في تشتت الموجات السطحية. وحيث أن الطـرق العكـسية لدوال المستقبل لها حساسية ضعيفة للسرع المضبوطة وللتغلب على هذه المشكلة فقد تم دمج سرع الموجات الجماعية في دوال المستقبل في شكل عكسي مـع سـرع القـشرة والوشـاح العلوي.

أعطت نماذج السرع الزلزالية في هذه الدراسة تحفظات جديدة على تراكيب القشرة والوشـاح العلوي لشبه الجزيرة العربية وحيث أن سماكة القشرة وسرعها في هذه الدراسة متشابه مـع الدراسات السابقة إلا أن نتائج تراكيب الوشاح وخواصه السيزمية يعتبر جديد تماما ولم يسبق إجراؤه في المنطقة.

وأخيرا تم فصل موجات القص للزلازل بعيدة المدى لتقدير خواص الوشـاح العلـوي . دلـت التحليلات على أن محطات منطقة خليج العقبة تشكل إتجاهات سريعة موازية لـصدع البحـر الميت التحولي ومرتبطة مع الحركة المضربية بين أفريقيا وشبه الجزيـرة العربيـة . بينمـا أعطت بقية المحطات في الدرع العربي نتائج إحصائية متشابهه وتأخذ شكلا متطابقـا بإتجـاه سريع شمال-جنوب مع معدل أزمنة تأخير قدرها ١،٤ثانية . وبدمج الإنسياب الذي يأخذ إتجاه شمال شرق والمرتبط بحركة الصفيحة المضبوطة مع الإنسياب الذي يأخذ إتجاه شمال غـرب والمرتبط بمثلث عفار على إمتداد البحر الأحمر تم إستنتاج محصلة تأخذ إتجاه شمال- جنوب مشابهه لنتائج الفصل وتؤيد نماذج الشد النشط ومراحل الإنفصال القاري.

يتغير تمدد قاع البحر الأحمر من شماله إلى جنوبه حيث يزداد التمدد كلما اتجهنا جنوبا ليصل إلى ١٤ ملم في السنة. يتضح من قراءة المقاطع التركيبية أن عمق الموهو والحد الفاصل بين الغلافين الصخري والوهن LAB أضحل بالقرب من البحر الأحمر ويزداد عمقها باتجاه المسطح العربي. يصل عمق الحد الفاصل بين الغلافين الصخري والوهن LAB إلى ٥٥ كم تقريبا بالقرب من ساحل البحر الأحمر ومابين ١٠٠-١١٠ كم تحت الدرع العربي أما عند حدود الدرع والمسطح العربي وصل عمق ال LAB إلى ١٦٠ كم. تؤيد هذه الدراسة مبدأ النموذج المتعدد والذي يقترح أن هناك مجريين ريشيين تحت الدرع العربي وأن المناطق منخفضة السرعة (مناطق ذات درجة الحرارة الأعلى) مرتبطة بالنشاطات البركانية والخواص الطبوغرافية على سطح الدرع العربي.

علاوة على ذلك تقترح نتائج هذه الدراسة وجود مرحلتين من الشّد في البحر الأحمر حيث التمدد والتعرية بالانسياب في الغلاف الوهن مسؤولة عن التغيرات في عمق ال LAB . دلت طبوغرافية ال LAB على انسياب الغلاف الوهن تحت الدرع العربي والبحر الأحمر والتي تلعب دوراً في التغيرات الحرارية للبيئة التكتونية .

وأخيرا توصي هذه الدراسة بإجراء عدد من الأبحاث الزلزالية الدقيقة لتخفيف مستوى الخطر الزلزالي في شبه الجزيرة العربية ومن هذه الدراسات على سبيل المثال لا الحصر ما يلي :

- ❖ تحديث شبكة الرصد الزلزالي في جامعة الملك سعود من بيانية إلى رقمية وربطها بشبكتي مدينة الملك عبدالعزيز للعلوم والتقنية وهيئة المساحة الجيولوجية وتوحيد برامج التشغيل بينها وذلك لتسهيل تبادل المعلومات و تحديد المعاملات الزلزالية بدقة عالية .
- ❖ إجراء تراكيب قشرية باستخدام معطيات الجاذبية الأرضية والمغناطيسية الجوّية في المناطق التي تفتقر إلى محطات رصد زلازل ومقارنة نتائج هذه التراكيب بما التوصل إليه من الطرق السيزمية الإنكسارية والزلزالية .
- ❖ تركيب راصدات الحركات الأرضية القوية في المناطق النشطة زالزالياً لحساب معدلات تعتيم الحركة الأرضية للاستفادة منها في تحديد معاملات الخطر الزلزالي وعمل خرائط التمنطق الزلزالي وتطوير كود البناء.

ABSTRACT

This final report of the research project AR-23-40 culminates the study reported in the previous three reports to estimate crustal and upper mantle structure. While there have been many studies of this topic using a wide variety of techniques, many questions about the structure of the Arabian Peninsula remain unanswered.

While for the most parts of Saudi Arabia, particularly, Arabian Shield and Arabian Platform a aseismic, the area is ringed with regional seismic sources in the tectonically active areas of Iran and Turkey to the northeast, the Red Sea Rift bordering the Shield to the southwest, and the Dead Sea Transform fault zone to the north.

The Arabian Shield and Red Sea region is considered one of only a few places in the world undergoing active continental rifting and formation of new oceanic lithosphere. We aim to determine the seismic velocity structure of the crust and upper mantle beneath this region using broadband seismic waveform data recorded by KACST seismic network. The network is operated by King Abdulaziz City for Science and Technology (KACST), Saudi Arabia and has 37 stations on the Arabian Shield and provides excellent sampling Shield and the adjacent Red Sea.

We estimate teleseismic receiver functions from high-quality waveform data. A raw data for RF analysis consist of 3-component broadband velocity seismograms for earthquakes with magnitudes $M_w > 5.8$ and epicentral distances between 30° and 90°. We performed several modern seismic analyses of KACST data. Teleseismic P- and S-wave travel time tomography provide an image of upper mantle compressional and shear velocities related to thermal variations. We present a multiple step procedure for jointly fitting surface wave group velocity dispersion curves (from 7 to 100 seconds for Rayleigh and 20 to 70 seconds for Love waves) and teleseismic receiver functions for lithospheric velocity structure. The method relies on an initial grid search for a simple crustal

structure, followed by a formal iterative inversion, an additional grid search for shear wave velocity in the mantle and finally forward modeling of transverse isotropy to resolve surface wave dispersion discrepancy.

Inversions of receiver functions have poor sensitivity to absolute velocities. To overcome this shortcoming we have applied the method of *Julia et al.* (2000) that combines surface wave group velocities with receiver functions in formal inversions for crustal and uppermost mantle velocities. The resulting velocity models provide new constraints on crustal and upper mantle structure in the Arabian Peninsula. While crustal thickness and average crustal velocities are consistent with many previous studies, the results for detailed mantle structure are completely new.

Finally, teleseismic shear-wave splitting was measured to estimate upper mantle anisotropy. These analyses indicate that stations near the Gulf of Aqabah display fast orientations that are aligned parallel to the Dead Sea Transform Fault, most likely related to the strike-slip motion between Africa and Arabia. The remaining stations across Saudi Arabia are statistically the same, showing a consistent pattern of north-south oriented fast directions with delay times averaging about 1.4 s. The uniform anisotropic signature across Saudi Arabia is best explained by a combination of plate and density driven flow in the asthenosphere. By combining the northeast oriented flow associated with absolute plate motion with the northwest oriented flow associated with the channelized Afar plume along the Red Sea, we obtain a north-south oriented resultant that matches our splitting observations and supports models of active rifting processes. This explains why the north-south orientation of the fast polarization direction is so pervasive across the vast Arabian Plate.

Seafloor spreading in the Red Sea is non-uniform, ranging from nearly 0 cm/yr in the north to about 2 cm/yr in the south. Given the configuration of stations, we focused our examination along profile AA', which extends from the southern Red Sea Rift axis inland to station HASS. This allowed us to examine the most extensively rifted portion of the lithosphere as well as the structure beneath both

the Arabian Shield and Platform. However, for comparison, we also examined the more northern profile BB', which extends from the northern rift axis across the Arabian Shield to station ARSS.

The Moho and LAB are shallowest near the Red Sea and become deeper towards the Arabian interior. Near the coast, the Moho is at a depth of about 22-25 km. Crustal thickening continues until an average Moho depth of about 35-40 km is reach beneath the interior Arabian Shield. The LAB near the coast is at a depth of about 55 km; however it also deepens beneath the Shield to attain a maximum depth of 100-110 km. These boundary depths are comparable to those at similar distances along profile AA'. At the Shield-Platform boundary, a step is observed in the lithospheric thickness where the LAB depth increases to about 160 km.

This study supports multi plume model which is that there are two, separated plumes beneath the Arabian Shield, and the lower velocity zones (higher temperature zones) are related with volcanic activities and topographic characteristics on the surface of the Arabian Shield. In addition, our results suggest a two-stage rifting history, where extension and erosion by flow in the underlying asthenosphere are responsible for variations in LAB depth. LAB topography guides asthenospheric flow beneath western Arabia and the Red Sea, demonstrating the important role lithospheric variations play in the thermal modification of tectonic environments.

In order to fully understand the detail geophysical, seismological and seismic hazard picture of the Arabian Peninsula, this study recommends an extensive research covering :

A. An expensive but potentially insightful line of research is to carry out a detailed seismic deep refraction and gravity profiles in the Arabian Platform and along the coast of the Gulf of Aqabah to obtain a precise bulk composition of crustal layers and improve velocity model.

B. Upgrading of the existing system at King Saud University from analog to digital broadband recordings is strongly recommended for getting better quality signals.

C. Linking of KACST and KSU seismic networks with the national seismographic network at the Saudi Geological Survey is of great importance for getting better and dense station coverage as well as in facilitating data exchanges.

D. Installation of strong motion accelerographs in various areas of the Arabian Shield to precisely estimate the attenuation characteristics of the region and to improve seismic hazard parameters.

E. Assessment of seismic hazard in seismically active zones by construeting a probabilistic ground-shaking hazard map. This map will provide an estimate of the level of ground shaking at all sites expected from earthquake sources throughout the region (both local and regional). The map integrates the seismicity, attenuation and sit response factors.

F. A comprehensive study of the geotechnical engineering aspects should be done to account for local site effects and soil amplification.

G. A comprehensive study of seismogenic and faulting sources is needed for seismic zonation and microzonation of the Arabian Penninsula.

TABLE OF CONTENTS

Page No.

LIST OF TABLES

LIST OF FIGURES

I. INTRODUCTION

The Arabian Peninsula presents several interesting seismological problems. On the west, rifling in the Red Sea has split a large Precambrian Shield. Active rifling is responsible for the geometry of the plate margins in the west and southwest. To the south, similar rifling running in a more east-west direction through the Gulf of Aden has separated the Arabian Peninsula from Africa. In the northwest, the Gulf of Aqabah forms the southernmost continuation of the Dead Sea transform. The northern and northeastern boundaries of the Arabian Plate are areas of continental collision, with the Arabian Plate colliding with the Persian Plate.

King Saud University (KSU) and King Abdulaziz City for Science and Technology (KACST) operate the networks in Saudi Arabia since 1985 (*Al-Amri and Al-Amri*,1999). Both networks feature the Boulder Real Time Technologies (BRTT) Antelope system, however the networks operate independently. Data is collected and transmitted in real time to the central processing facilities in Riyadh. Events are automatically detected and located and waveforms are excerpted for later analysis while continuous data are archived. The KACST network features 37 stations (26 BB STS-2 and 11 SP sensors). The system uses the iasp91 earth model to locate events. Figure 1.1 shows all events with magnitude greater than 5.5 recorded by KACST stations between 2000-2004. Events we had access to are shown in red. The large number of new events in the proper distance range for S and SKS splitting analysis should be sufficient to allow us to investigate patterns of splitting parameters with arrival direction and determine if more complex anisotropic models are required below the Red Sea Rift.

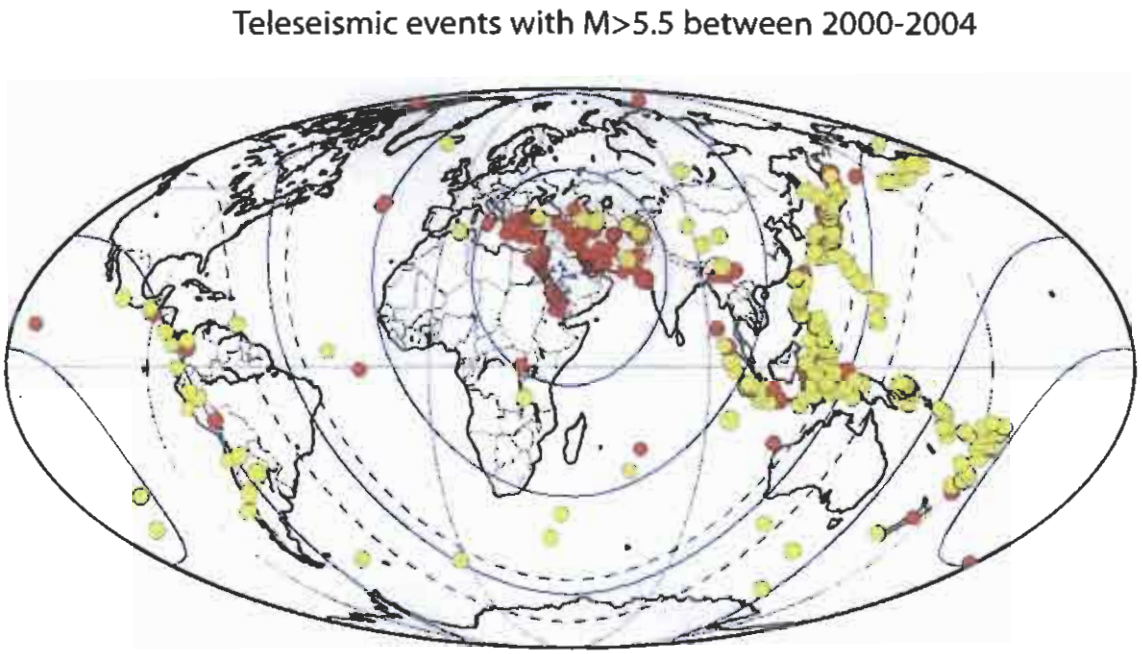

Figure 1.1 Map of the world centered on the Red Sea showing events recorded by SANSN broadband stations between 2000-2001 (red) and 2002-2004 (yellow). Events outside the first contour (30°) are at teleseismic distances and all have magnitude >5.5. Some events within the 30° contour have magnitudes <5.5. Many of the red events (2000-2001) in the western Pacific subduction zones are hidden beneath the more recent events (yellow).

The Saudi Arabian Broadband Deployment (SABD, *Vernon et al.*, 1996) provided the first data set of broadband recordings of this region. This deployment consisted of 9 broadband three-component seismic stations along a similar transect an early seismic refraction study (*Mooney et al.*, 1985; *Gettings et al.*,1986; *Mechie et al.*,1986). Data from the experiment resulted in several studies and models of the seismic structure of the Arabian Shield (*Sandvol et al.*, 1998; *Mellors et al.*, 1999; *Rodgers et al.*, 1999; *Benoit et al.*, 2002; *Al-Amri et al.*,2004; *Al-Damegh et al.*,2004). These studies provided new constraints on crustal and upper mantle structure. The crustal model of the western Arabian Platform shows a little higher P-velocity for the upper crust in the Shield than in the Platform and the crustal Platform seems to have a greater thickness than in the Shield by about 3

km. The Moho discontinuity beneath the western Arabian Platform indicates a velocity of 8.2 km/sec of the upper mantle and 42 km depth (*Al-Amri*, 1998;1999).

Generally the crustal thickness in the Arabian Shield area varies from 35 to 40 km in the west adjacent to the Red Sea to 45 km in central Arabia (*Sandvol et al.*, 1998; *Rodgers et al.*, 1999). Not surprising the crust thins nears the Red Sea (*Mooney et al.*, 1985; *Gettings et al.*, 1986; *Mechie et al.*, 1986). High-frequency regional S-wave phases are quite different for paths sampling the Arabian Shield than those sampling the Arabian Platform (*Mellors et al.*, 1999; *Sandvol et al.*, 1998). In particular the mantle Sn phase is nearly absent for paths crossing parts of the Arabian Shield, while the crustal Lg phase is extremely large amplitude. This may result from an elastic propagation effect or extremely high mantle attenuation and low crustal attenuation occurring simultaneously, or a combination of both.

Previous reports of large scale seismic structure (e.g. *Ritsema et al.*, 1999 and *Debayle et al.*, 2001) suggest that a low velocity anomaly in the upper mantle extends laterally beneath the Arabian Shield from the Red Sea in the west to the shield – platform boundary in the east. Additionally, *Debayle et al.* (2001) observe a narrow region of low velocity beneath the Red Sea and western edge of the Arabian Shield, extending to 650 km depth. A recent tomographic velocity model and receiver function analysis by *Benoit et al.* (2002) suggests the upper mantle low velocity anomaly is smaller in extent, laterally and vertically, than imaged in previous studies.

The Red Sea is a region of current tectonic activity where continental lithosphere is being rupture to form oceanic lithosphere. Opening of the Red Sea split the Arabian-Nubian Shield. While much work has been done to understand the uplift and volcanism of the Arabian Shield little is known about the structure of the underlying upper mantle. The Arabian Shield consists of at least five Precambrian terranes separated by suture zones (*Schmidt et al.*, 1979). During the late Oligocene

and early Miocene, the Arabian Shield was disrupted by the development of the Red Sea and Gulf of Aden rifts, and from the mid-Miocene to the present, the region experienced volcanism and uplift (*Bohannon et al.,* 1989). The uplift and volcanism are generally assumed to be the result of hot, buoyant material in the upper mantle that may have eroded the base of the lithosphere (*Camp and Roobol*, 1992). However details about the nature of the upper mantle, such as its thermal and compositional state, are not known.

Saudi Arabia and the Red Sea Rift zone offer an excellent environment in which to study the seismic anisotropy associated with rifting and extension. Several different types of models have been proposed to explain how continental rifting in the Red Sea developed. The passive rifting model assumes simple shear conditions where extensional stresses are accommodated on large-scale detachment planes extending through the entire lithosphere below the rift. Flow beneath the rift is parallel to the direction of extension as the underlying asthenosphere is passively upwelled, which would predict a rift-perpendicular φ. The active rifting model involves thinning of the lithosphere by flow in the underlying asthenosphere and requires the presence of hot, ascending material (*Camp and Roobol,* 1992; *Ebinger and Sleep,* 1998; *Daradich,* 2003). In this case, local convection may lead to more complicated flow patterns and therefore more complex anisotropy at depth. Several studies have suggested that these two end-member models may not be mutually exclusive; rifting in the Red Sea may have been initiated by far-field collision and passive processes, followed by more recent active processes associated with a mantle plume (*Camp and Roobol*, 1992; *Ebinger and Sleep,* 1998; *Daradich et al.*, 2003).

Several previous studies have examined the anisotropic characteristics in the vicinity of the Red Sea Rift and show a fairly consistent pattern. Using 8 PASSCAL stations across the Arabian Shield, *Wolfe et al.* (1999) performed shear-wave splitting analysis and found δt of 1.0-1.5 s and φ oriented

approximately north-south. Using receiver functions, *Levin and Park* (2000) found evidence for a more complex anisotropic structure beneath PASSCAL station RAYN consisting of two dipping layers at depth, but again with a resultant φ oriented north-south. Further north, *Schmid et al.* (2004) and *Levin et al.* (2006) examined splitting at several stations near the Gulf of Aqabah and the Dead Sea Transform Fault, where they found average δt of about 1.3 s and φ slightly east of north, with some evidence for a more complex, two-layer anisotropic model. However, each of these studies was somewhat limited in their station distribution and data availability.

Recently, *Hansen et al.* (2006) presented a more comprehensive analysis of the anisotropic signature along the Red Sea and across Saudi Arabia by analyzing shear-wave splitting recorded by stations from three different seismic networks. This is the largest, most widely distributed array of stations examined across Saudi Arabia to date. They demonstrated that the north-south orientation of the fast polarization direction is not just valid at isolated sites on the Arabian Shield, but extends throughout the whole of Arabia.

In this project we extend previous efforts to determine crustal and lithospheric mantle structure under the Arabian Shield and Red Sea by applying an improved method for inverting receiver functions and shear wave group velocity (SWGV) measurements. We apply this technique to a number of stations that sample the complexity of tectonic environments and provide new constraints on structure.

While there have been many studies of this topic using a wide variety of techniques, many questions about the structure of the Arabian Peninsula remain unanswered. A thorough understanding of the seismic structure and wave propagation characteristics of the region must be established before we can proceed to assess seismic hazard. We implemented several types of analysis to seismic data recorded by KACST seismic network. These analyses will include:

- teleseismic P- and S-wave travel time tomography;
- teleseismic receiver functions for crustal structure;
- teleseismic receiver functions for upper mantle discontinuity structure;
- teleseismic shear-wave splitting; and
- regional and far-regional surface waveform modeling.

Together these analyses result in a unified model of the structure and physical state of the lithosphere beneath the Arabian Shield and Red Sea. The dense station spacing and excellent quality of the KACST data allow for very detailed resolution of structure.

II. SEISMOTECTONICS & SEISMIC STRUCTURES

The Arabian Peninsula forms a single tectonic plate, the Arabian Plate. It is surrounded on all sides by active plate boundaries as evidenced by earthquake locations. Figure 2.1 shows a map of the Arabian Peninsula along with major tectonic features and earthquake locations. Active tectonics of the region is dominated by the collision of the Arabian Plate with the Eurasian Plate along the Zagros and Bitlis Thrust systems, rifting and seafloor spreading in the Red Sea and Gulf of Aden. Strike-slip faulting occurs along the Gulf of Aqabah and Dead Sea Transform fault systems. The great number of earthquakes in the Gulf of Aqabah pose a significant seismic hazard to Saudi Arabia. Large earthquakes in the Zagros Mountains of southern Iran may lead to long-period ground motion in eastern Saudi Arabia.

The two large regions associated with the presence or absence of sedimentary cover define the large-scale geologic structure of the Arabian Peninsula. The Arabian Platform (eastern Arabia) is covered by sediments that thicken toward the Arabian Gulf. The Arabian Shield is has no appreciable sedimentary cover with many outcrops. Figure 2.2 shows the sediment thickness, estimated from compiled drill hole, gravity and seismic reflection data *(Seber et al., 1997)*. The Arabian Shield consists of at least five Precambrian terranes separated by suture zones *(Schmidt et al., 1979)*. During the late Oligocene and early Miocene, the Arabian Shield was disrupted by the development of the Red Sea and Gulf of Aden rifts, and from the mid-Miocene to the present, the region experienced volcanism and uplift *(Bohannon et al., 1989)*. The uplift and volcanism are generally assumed to be the result of hot, buoyant material in the upper mantle that may have eroded the base of the lithosphere *(Camp and Roobol, 1992)*. However details about the nature of the upper mantle, such as its thermal and compositional state, are not known. Volcanic activity (the Harrats) is

observed on the Arabian Shield (Figure 2.1). This is likely to be related to the opening of the Red Sea and mantle asthenospheric upwelling beneath western Arabia (e.g. *Camp and Roobol*, 1992).

The northwestern regions of Saudi Arabia are distinct from the Arabian Shield, as this region is characterized by high seismicity in the Gulf of Aqabah and Dead Sea Rift. Active tectonics in this region is associated with the opening of the northern Red Sea and Gulf of Aqabah as well as a major continental strike-slip plate boundary.

The Dead Sea transform system connects active spreading centers of the Red Sea to the area where the Arabian Plate is converging with Eurasia in southern Turkey. The Gulf of Aqabah in the southern portion of the rift system has experienced left-lateral strike-slip faulting with a 110 km offset since early Tertiary to the present. The seismicity of the Dead Sea transform is characterized by both swarm and mainshock-aftershock types of earthquake activities. The instrumental and historical seismic records indicate a seismic slip rate of 0.15-0.35 cm/year during the last 1000-1500 years, while estimates of the average Pliocene-Pleistocene rate are 0.7-1.0 cm/year.

Historically, the most significant earthquakes to hit the Dead Sea region were the events of 1759 (Damascus), 1822 (Aleppo), and of 1837 ;1068 (Gulf of Aqabah area) caused deaths of more than 30,000 people. *Ben Menahem* (1979) indicated that about 26 major earthquakes ($6.1<ML<7.3$) occurred in southern Dead Sea region between 2100 B.C. and 1900 A.D. In 1980's and 1990's, the occurrence of earthquake swarms in 1983, 1985, 1991, 1993 and 1995 in the Gulf of Aqabah clearly indicates that this segment is one of the most seismically active zones in the Dead Sea transform system. Earthquake locations provide evidence for continuation of faulting regime from the Gulf northeastward inland beneath thick sediments, suggesting that the northern portion of the Gulf is subjected to more severe seismic hazard compared to the southern portion (*Al-Amri et al.*,1991).

To the south, the majority of earthquakes and tectonic activity in the Red Sea region are concentrated along a belt that extends from the central Red Sea region south to Afar and then east through the Gulf

of Aden. There is little seismic activity in the northern part of the Red Sea, and only three earthquakes have been recorded north of latitude 25° N. Instrumental seismicity of the northern Red Sea shows that 68 earthquakes (3.8<mb<6.0) are reported to have occurred in the period from 1964 to 1993. Historically, about 10 earthquakes have occurred during the period 1913-1994 with surface-wave *(Ms)* magnitudes between 5.2 and 6.1. Some of these events were associated with earthquake swarms, long sequences of shocks and aftershocks (the earthquakes of 1941, 1955, 1967 and 1993). The occurrence of the January 11,1941 earthquake in the northwest of Yemen (*Ms = 5.9*) with an aftershock on February 4, 1941 *(Ms* = 5.2), the earthquake of October 17, 1955 *(Ms* = 4.8), and the 1982 Yemen earthquake of magnitude 6.0 highlight the hazards that may result from nearby seismic sources and demonstrate the vulnerability of northern Yemen to moderate-magnitude and larger earthquakes. Instrumental seismicity of the southern Red Sea shows that 170 earthquakes (3.0<*mb*< 6.6) are reported to have occurred in the period 1965-1994. The historical and instrumental records of strong shaking in the southern Arabian Shield and Yemen (1832; 1845; 1941; 1982 and 1991) indicate that the return period of severe earthquakes which affect the area is about 60 years (*Al-Amri*,1995 b).

The Arabian Plate boundary extends east-northeast from the Afar region through the Gulf of Aden and into the Arabian Sea and Zagros fold belt. The boundary is clearly delineated by teleseismic epicenters, although there are fewer epicenters bounding the eastern third of the Arabian Plate south of Oman. Most seismicity occurs in the crustal part of the Arabian Plate beneath the Zagros folded belt (*Jackson and Fitch*,1981). The Zagros is a prolific source of large magnitude earthquakes with numerous magnitude 7+ events occurring in the last few decades. The overall lack of seismicity in the interior of the Arabian Peninsula suggests that little internal deformation of the Arabian Plate is presently occurring.

Seismic structure studies of the Arabian Peninsula have been varied, with dense coverage along the 1978 refraction survey and little or no coverage of the aseismic regions, such as the Empty Quarter. In 1978, the Directorate General of Mineral Resources of Saudi Arabia and the U.S. Geologic Survey conducted a seismic refraction survey aimed a determining the structure of the crust and upper mantle. This survey was conducted primarily in the Arabian Shield along a line from the Red Sea to Riyadh. Reports of crust structure found a relatively fast velocity crust with thickness of 38-43 km (*Mooney et al*,1985; *Mechie et al*,1986; *Gettings et al*,1986, *Badri*,1991). The crust in the western shield is slightly thinner than that in the eastern shield.

Mooney et al.(1985) Suggest that the geology and velocity structure of the Shield can be explained by a model in which the Shield developed in the Precambrian by suturing of island arcs. They interpret the boundary between the eastern shield and the Arabian Platform as a suture zone between crustal blocks of differing composition.

Surface waves observed at the long-period analog stations RYD (Riyadh), SHI (Shiraz, Iran), TAB (Tabriz, Iran), HLW (Helwan, Egypt), AAE (Addis-Ababa, Ethiopia) and JER (Jerusalem) were used to estimate crustal and upper mantle structure (*Seber and Mitchell*, 1992; *Mokhtar and Al-Saeed*,1994). These studies reported faster crustal velocities for the Arabian Shield and slower velocities for the Arabian Platform.

The Saudi Arabian Broadband Deployment (*Vernon and Berger et al.*, 1997; *Al-Amri et al.*, 1999) provided the first data set of broadband recordings of this region. This deployment consisted of 9 broadband three-component seismic stations along a similar transect an early seismic refraction study (*Mooney et al., 1985; Gettings et al.,1986; Mechie et al.*,1986). Data from the experiment resulted in several studies and models (*Sandvol et al.*, 1998; *Mellors et al.*, 1999; *Rodgers et al.*, 1999; *Benoit et al.*, 2002). These studies provided new constraints on crustal and upper mantle structure. The crustal model of the western Arabian Platform shows a little higher P-velocity for the

upper crust in the Shield than in the Platform and the crustal Platform seems to have a greater thickness than in the Shield by about 3 km. The Moho discontinuity beneath the western Arabian Platform indicates a velocity of 8.2 km/sec of the upper mantle and 42 km depth (*Al-Amri,*1998;1999). *Julià et al.*([2003) presented velocity models for the same stations, combining RF with surface wave dispersion data to invert for structure. *Al-Damegh et al.* (2005) calculated RF's for the Arabian Plate from permanent broadband stations in Saudi Arabia (*Al-Amri and Al-Amri,* 1999) and Jordan (*Rodgers et al.*, 2003a).

Figure 2.3 shows the iasp91 model along with lithospheric velocity models from our earlier work (*Rodgers et al.*, 1999; *Rodgers et al.*, 2001). As one can see *iasp91* has no sediment layer and the crustal thickness (35 km) is thin compared to the Arabian Platform model. There are also differences between the mantle velocities.

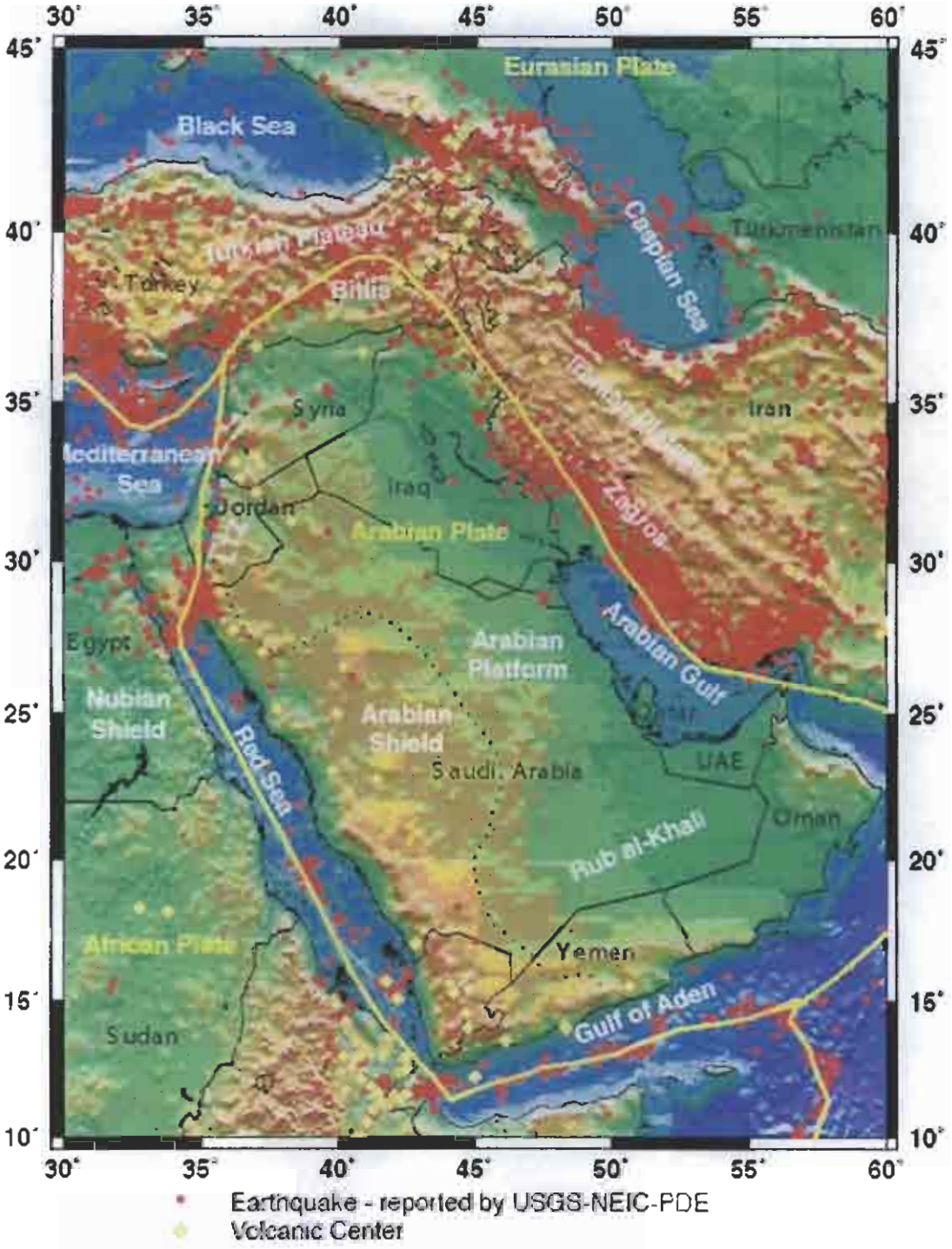

Figure 2.1 . Map of the Arabian Peninsula and surrounding regions. Major geographic and tectonic features are indicated. Plate boundaries are indicated by yellow lines. Earthquakes and volcanic centers shown as red circles and yellow diamond, respectively.

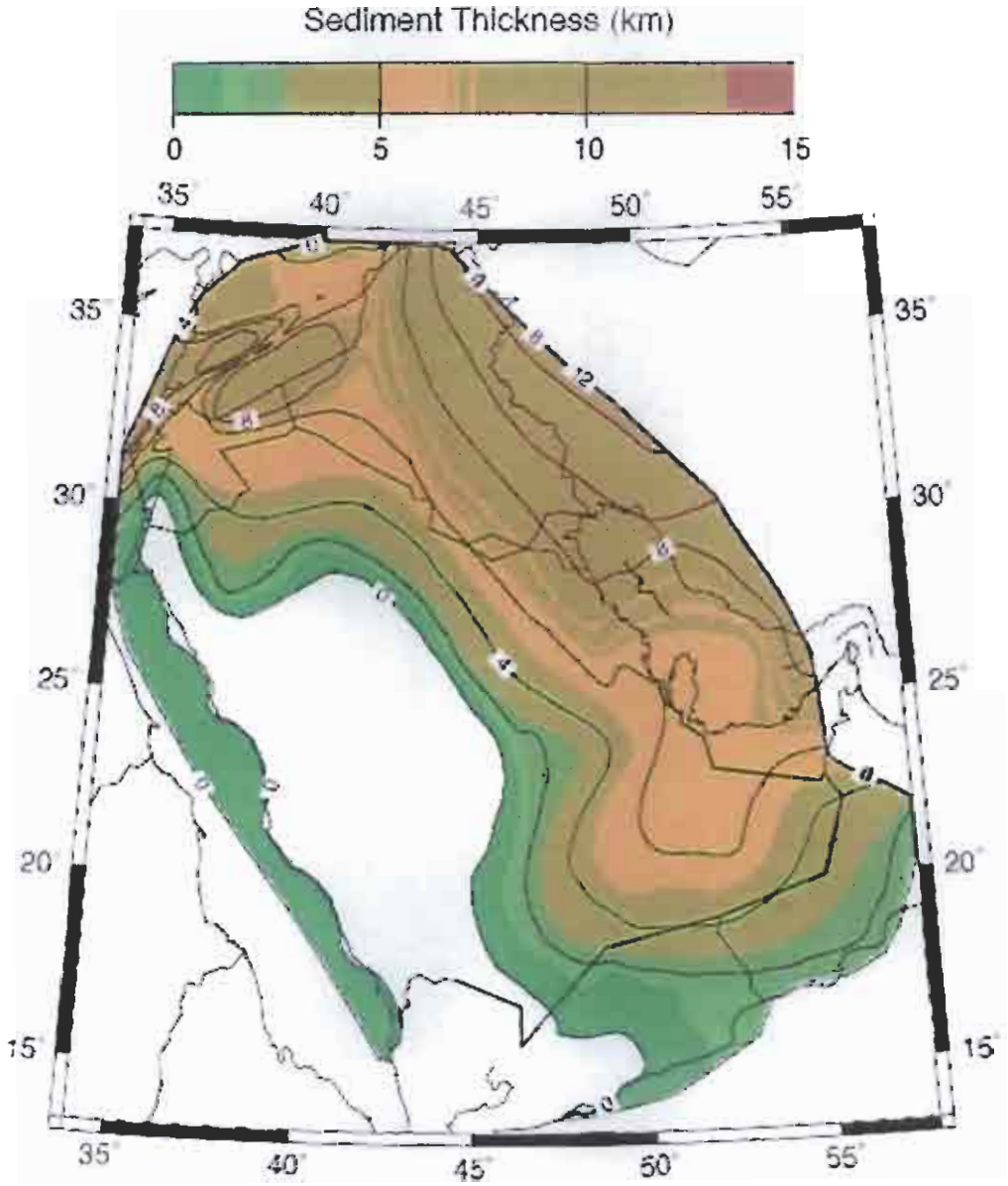

Figure 2.2. Map of sediment thickness of the Arabian Plate.

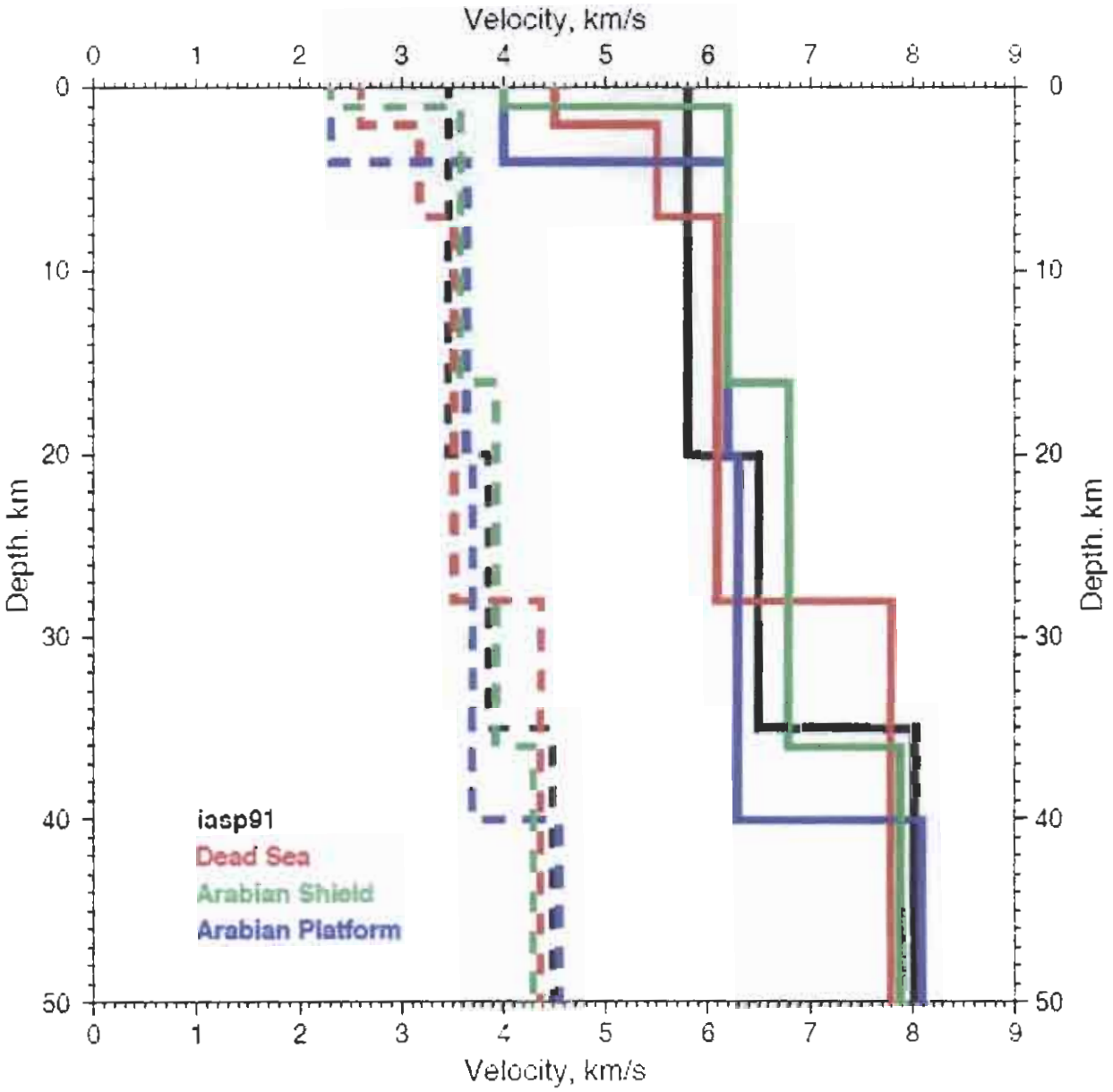

Figure 2.3. Seismic P- and S-wave velocity models, solid and dahsed respectively, for the Arabian Peninsula from various sources described in the text.

III. SEISMOGRAPHIC NETWORKS

There are two independent analog seismic telemetry networks in Saudi Arabia. King Saud University (KSU) network features 31 stations. King Abdulaziz City for Science and Technology (KACST) operates a network of three-component broadband and short-period stations (*Al-Amri and Al-Amri*, 1999). Both networks have stations throughout the Kingdom of Saudi Arabia, but the station density is greatest near the Gulf of Aqabah. These networks recorded the shots with good signal-to-noise above about 0.5 Hz.

Recently, KSU and KACST networks run the Boulder Real Time Technologies (BRTT) Antelope System as described below.

ANTELOPE is a system of software modules that implement acquisition, transport, buffering, processing, archiving and distribution of environmental monitoring information. Antelope is a distributed, open-architecture, UNIX-based acquisition, analysis and management system. It consists of two major sub-systems, namely Antelope Real Time System **(ARTS)** and Antelope Seismic Information System **(ASIS)**.

ARTS brings raw data from remote field sites in real time to KSU processing center where, automated real time processing of data is performed and information is automatically merged into long term information system archives. Within ARTS, data is buffered and transported through a mechanism known as an Object Ring Buffer **(ORB)**, which acts as the heart of ARTS. The ORB is managed by a single program, "*obrserver*". Field interface modules write all of the data from the field stations into the ORB. The concepts behind an ORB are straightforward:

1) A circular raw data store on disk

2) A server-client approach to manage the circular data store

3) All server-client inter-process communications take place through Internet sockets using TCP/IP.

Real time Richter magnitude estimates are made by a module called "*orbmag*". This program looks for ASIS origin rows data in the data processing ORB. For each origin read, *orbmag* determines appropriate time windows for each station and acquires the waveform data for all components from the same data processing ORB. Each waveform segment is converted to equivalent drum recorder displacement of a standard Wood-Anderson instrument and the maximum amplitude for the event is determined. These amplitudes are fed into the standard Richter magnitude formula for computing ml values for each station and all of the station ml values are median averaged to get a total network ml estimate. The *ml* estimate is used to modify the input origin row and this modified origin row is written back into the data processing ORB.

Location capability is provided by program "*orbgenloc*" which uses traditional inversion algorithm. The program "*orbenloc*" provides a generic location capability using traditional inversion algorithms. In addition, locations produced by "*orbassoc*" module can be fine tuned with "*orbgenloc*". "*orbgenloc*" reads the arrival, association and preliminary hypocenter information produced by "*orbassoc*" and computes a more refined earthquake location using a variety of traditional inversion algorithms. The refined locations are written to an output ORB as database row packets.

3.1 KSU Seismographic Network

The King Saud University (KSU) seismological network was established in 1985 and includes the digital WWSSN station in Riyadh. Currently, the network consists of 31 stations with denser sub-networks in the Gulf of Aqabah region (12 stations) and the southwestern part of Saudi Arabia (8 stations). The seismographic station in Riyadh is a 6 - channel station and consists of three S-13 short-period and three SL-200 long-period seismometers. The seismometer outputs are amplified, filtered and reeorded in both analog and digital form. The filters allow recording in four different

periods (SP wide band, SP narrow band, LP wide band and LP narrow band). The total system response for the Riyadh station is broadband (0.01 to 33 Hz). Signals from the 9 channels are also routed to a 12-bit A-to-D converter and recorded on 9-track magnetic tape. The other telemetered seismic stations are equipped with S-13 short-period seismometers connected to a field case housing an amplifier, a voltage controlled oscillator (VCO), an automatic daily calibrator and a telemetry interface.

3.2 KACST Seismographic Network

In May 1998 King Abdulaziz City for Science and Technology (KACST) began operating the seimic network. A description of the network is given in *Al-Amri and Al-Amri* (1999). It consists of 38 stations mostly distributed across the Arabian Shield (western Saudi Arabia, Figure 3.1). The instrumentation features 27 broadband and 11 short-period instruments. The station information is compiled in Table 3.1. All stations record three-component ground motions at a sample rate of 100 samples/second. The stations operate continuously and transmit data in real-time to the KACST Headquarters building in Riyadh. The KACST Data Center receives the raw waveform data and runs the Boulder Real Time Technologies (BRTT) Antelope System. This is a software package for managing real-time seismic network data and performing the basic network operations of detection, association and location of events as well as data archival. A short-term average-to-long-term average (STA/LTA) energy detector runs continuously and detects phase arrivals. The system attempts to locate the event if a number of arrivals are detected by the network within a specified time window. The system locates events relative to a single average global velocity model (*iasp91*, *Kennett and Engdahl*, 1991). This is a global continental average velocity model derived from worldwide observations of seismic travel times. While this model is appropriate for locating distant events, it is not necessarily a good model for locating events in and around the Arabian Peninsula.

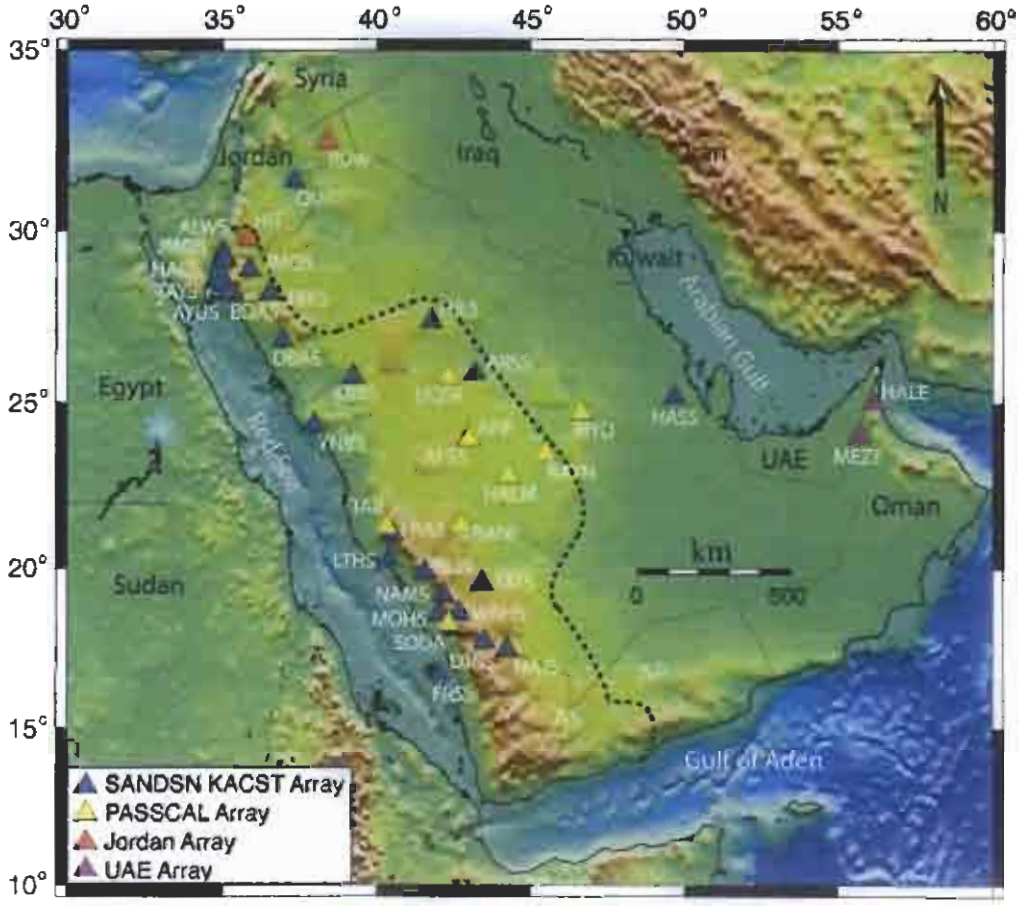

Figure 3.1. Teleseismic data from four different seismic arrays were used in this study (KACST, IRIS-PASSCAL, Jordan and UAE).

3.3 SGS National Seismographic Network

In 2005, The Saudi Geological Survey (SGS) began operating the national seismographic network in Jeddah, Saudi Arabia. It consists of 27 broadband stations distributed across the Arabian Shield and Platform (Figure 3.3) and the station information is compiled in Table 3.2.

SGS broadband seismic stations consist of Nanometrics Trillium broadband seismometers, 24-bit digitizers, GPS receivers, and VSAT transceivers. The current VSAT being used is a private or closed system that uses TDMA (time-domain multiple access) for satellite channel sharing on ARABSAT-2B and UDP/IP communication protocol for data transmission and commands to remote stations. Data from remote sites are transmitted to satellite then to the SGS master station (HUB) in Jeddah. The satellite channel usage is managed via commands from the SGS seismic center. The Ku band for the SSPB (solid-state-power-block or transmitter final stage and up frequency converter) and LNB (low-noise-block or receiver) is susceptible to rain fade and thus a provision for lost packets is required. In addition to data recovery and remote sensor calibration, the VSAT system allows configuration of remote sites via a lower data rate TDMA channel. The present Ku band VSAT system has proven to be quite robust and operates well even in severe dust storms.

All seismic data (45 channels) from 15 remote seismic stations are received by the master VSAT station (HUB) at the seismic center in Jeddah. At present several servers (SUN workstations and PC workstations) are dedicated to network management software that put all data in ring buffers for access by client programs such as event detection and picking programs. Automatic picks

Figure 3.2 Geographic map showing the locations of SGS seismic stations.

Table 3.1 Stations of KACST Digital Seismic Network.

Station Code	Station Location	Latitude	Longitude	Elevation (meters)	Sensor Type
AFFS	Afif	23.9267	43.0005	109	BB
ALWS	As Safayhah	29.3103	35.0650	0	SP
ARSS	Ar Rass	25.8810	43.2365	72	BB
AYUS	Aynunah	28.1889	35.2689	0	SP
BDAS	Al Bada	28.4317	35.1014	36	BB
BIDS	Al Bida	26.8670	36.9595	0	BB
BLJS	Baljurashi	19.8812	41.5992	206	BB
DBAS	Duba	27.2114	35.9773	18	SP
DJNS	Dahran-Al-Janub	17.7073	43.5434	220	BB
FRAS	Faraa	21.0622	40.5200	0	BB
FRJS	J.-Farasan	22.5905	39.3638	0	SP
FRSS	Farasan Island	16.7392	42.1143	0	BB
HAQS	Haql	29.0548	34.9297	42	BB
HASS	Al Hasa	25.1899	49.6944	20	BB
HILS	Al Hail	27.3835	41.7917	108	BB
HKNS	J.-Hakran	22.6420	41.7158	0	SP
HWYS	Hawiyah	21.4349	40.4177	0	SP
JAZS	Jizan	17.0678	42.9177	0	SP
JMOS	J. Al-Moallq	29.1686	35.1094	0	BB
JMQS	J. Al-Moqyreh	28.8861	35.8778	0	BB
KAMS	Al Khamasin	20.3092	44.5798	75	SP
KBRS	Harrat Khaybar	25.7893	39.2623	78	BB
LBNS	J. Laban	21.0465	39.9013	0	BB
LTHS	Al Lith	20.2750	40.4107	18	BB
MOHS	Muhayl	18.5761	42.0190	52	BB
MYKS	Mirrayikh	21.5545	39.3323	0	SP
MZLS	Mezel	24.0275	45.2071	88	SP
NAJS	Najran	17.5034	44.2847	131	BB
NAMS	Namsa	19.1714	42.2084	252	BB
QURS	Al Hadithat	31.3860	37.3240	49.1	BB
RNYS	Wadi Ranyah	21.4267	42.7662	0	SP
RYDS	Riyadh	24.1900	46.6400	0	BB
TATS	Tathlith	19.5412	43.4775	110	BB
TAYS	Tayyib Ism	28.5511	34.8717	0	BB
TBKS	Tabuk	28.2248	36.5485	82	BB
UMJS	Umm Lajj	25.2340	37.3119	13	SP
WBHS	Wadi-Ibnhashbal	18.6057	42.7144	187	SP
YNBS	Yanbu	24.3397	37.9922	8	BB

Table 3.2 Stations of SGS National Seismic Network.

STATION	LONGITUDE	LATITUDE
SGS01	40.51830	21.05840
SGS02	39.69070	21.44850
SGS03	40.35900	21.83220
SGS09	39.68382	21.00450
SGS10	47.24482	22.03856
SGS12	50.84604	24.04615
SGS13	49.46148	22.92739
SGS15	50.64384	24.79768
SGS16	38.74320	24.35750
SGS19	49.37570	25.86875
SGS22	36.32290	26.78340
SGS23	44.34106	27.50471
SGS24	47.94161	28.18663
SGS25	34.79676	28.29980
SGS26	35.49159	28.73540
SGS27	35.06222	29.30028

(STA/LTA trigger algorithm) are written to a database for later reference and post processing of data. In addition to seismic data, the center has access to state-of-health (SOH) data (battery voltages, temperatures, GPS and clock performance, re-transmission requests, data thru-put) to assist in tracking station performance and to assist in station maintenance. SOH information is very useful in detecting antenna alignment problems and is easily accessible via a JAVA GUI interface.. The primary network management software is provided by Nanometrics, Inc., Canada. SGS also uses USGS EARTHWORM software for real-time earthquake picks and locations and Oracle database software with extensions provided by Nanometrics. The current primary post processing software

for phase and amplitude picks, plots, and magnitude calculations is Atlas. Atlas is a JAVA based earthquake picking program that works on any computer system with a JAVA run time environment. Atlas reads SEED files, event-wave files in the Oracle database, and extracts event-wave data from the NAQS ring buffer. HYPOINVERSE (Klein, 2002) is the primary earthquake location program used by SGS. Earthquake epicenter plots can be easily viewed in Atlas and a Wood-Anderson simulation is provided in Atlas for computing of local magnitudes.

3.4 GSN Seismic Station

RAYN is one of the newest stations in the IRIS/IDA global seismographic network. The seismic station at Ar Rayn (RAYN), Saudi Arabia was established in 1996 under a memorandum of understanding between KACST, the IRIS Consortium, and the University of California, San Diego (UCSD), with key support from the KSU Department of Geology.

RAYN station consists of a STS-2 three-component broadband seismometer (passband between 0.008 Hz and 50 Hz), a Kinemetrics FBA-23 strong motion accelerometer, and a Teledyne broadband KS-54000 (passband between 0.0003 Hz and 8 Hz). The KS-54000 is emplaced in a borehole at a depth of 100 meters to insure the quietest possible recording environment. The purpose of installing the STS-2 is to provide much better coverage of high frequencies than would be possible with the KS-54000 alone. The FBA-23 is in place to record ground motion from earthquakes either too large or too close to be recorded on-scale by the KS-54000 and STS-2. All sensors are recorded on an IRIS-3 high-resolution data acquisition system.

The IRIS/IDA station RAYN has noise characteristics which place it among the quietest seismic stations in the world. Minimum detectable magnitudes are estimated for RAYN station using the observed noise levels over 1 Hz. The m_b detection threshold for the distance range of 5-10 degrees is about m_b = 2.7-3.0 assuming the signal-to-noise ratio of 3 dB or better.

IV. METHODOLOGY

We improved our understanding of the crustal structures and upper mantle of the Red Sea and the Arabian Shield using broadband waveform data from KACST Digital Seismic Network. The proposed research includes standard seismological investigations as well as newly developed techniques as follows :

4.1 Data Collection and Validation

The investigators wrote software to extract waveform data from the KACST data archive. This software facilitated the extraction and exchange of seismic waveform and parameter data.

In order to validate the station timing and instrument response we performed comparisons of timing and amplitudes of P-waves for large teleseismic events at the KACST stations with the Global Seismic Station RAYN. This station has well calibrated timing and instrument response. The relative arrival times of teleseismic P-waves at the KACST can be accurately measured by cross-correlating with the observed waveforms at RAYN and correcting for distance effects. Absolute amplitudes of teleseismic P-waves at the KACST and RAYN stations were measured by removing the instrument response, gain and band-pass filtering.

This study also considered many events and computed average travel time and amplitude residuals relative to a globally averaged one dimensional earth model, such as iasp9l. Although there were deviations between the timing and amplitudes of KACST P-waves from the predictions of the iasp9I model (because of lateral heterogeneity) the tests were useful to identify which stations might have timing and / or instrument calibration problems.

4.2 Teleseismic Travel Time Tomography

A number of tomographic methods are available for using P and S wave travel time delays to image upper mantle velocity variations (e.g., *Thurber,*1983; *VanDecar,*1991; *Evans and Achauer*, 1993). We used these methods to image relative velocity variations in the upper mantle beneath the Arabian Shield. An example of the results we obtained is provided by a recent study by *Benoit et al.* (2002) of upper mantle P wave velocity structure under the Arabian Shield. In this study, P wave travel time residuals were determined from the SABD dataset using the multi-channel cross correlation (**MCCC**) method of *VanDecar and Crossen* (1990) and then modeled using the inversion method of *VanDecar* (1991). The MCCC method of *VanDecar and Crossen* (1990), which makes use of the waveform coherency that is found across a regional network, involves three steps. First, the data is band-passed filtered between 0.5 and 5 Hz. A cross correlation is then computed for all possible pairs of stations to find the relative arrival times, and finally a least squares optimization scheme is applied to the arrival times to minimize inconsistencies in the data. The uncertainties in the relative P wave travel times obtained from the SABD dataset are about 0.1 to 0.15 seconds. After computing the travel time residuals, they were inverted for P wave slowness and earthquake relocations. The inversion searches for the smoothest model with the least amount of structure that will match the data. The inversion is linear and minimizes both spatial gradients and model roughness using a conjugate gradient scheme as shown in the flow chart. Root mean square (rms) and variance reduction (VR) for each model are calculated as a measure of misfit according to the following expressions:

$$rms = \sqrt{\frac{N_{\max}}{N}} \sqrt{\frac{\sum_{i=1}^{N} w_i (obs_i - theor_i)^2}{N}};$$

$$VR = \{1 - \sqrt{\frac{\sum_i (obs_i - theor_i)^2}{\sum_i obs_i^2}}\}100\%$$

where N is the number of selected periods for Love or Rayleigh wave dispersion at a given station (typically, we consider 11 discrete periods spanning from 20 to 70 seconds for Love waves, and 20 discrete periods spanning from 7 to 100 seconds for Rayleigh waves), and N_{max} is the number of periods for Rayleigh wave dispersion. $\sqrt{\frac{N_{max}}{N}}$ is then a normalization factor, which equalizes the relative significance of rms results for Love and Rayleigh wave dispersion, given the fact that less data points are available for Love waves. w_i is defined as 1/e (where e is the error of each point in surface wave dispersion curves) and is a relative weight of each velocity measurement in the dispersion. If there is a large misfit at only period of the group velocity dispersion, the above expression for rms would significantly impact the result. However, the above expression for variance reduction would not significantly penalize the result. Therefore, variance reduction is more appropriate measure of misfit than rms for waveforms (receiver functions) with much larger number of points than in discrete dispersion measurements, where it is important to fit the character of the waveform. rms and VR expressions are used combined as criteria for selection and plotting small percentages of the best models.

Overall, even though the resulting models consisting of 3-layer crust and a half space are in many cases too simplistic, we note that some excellent matches of the data by the synthetics were found, particularly in cases when only receiver function or only surface wave data (either Love or Rayleigh wave dispersion) are considered.

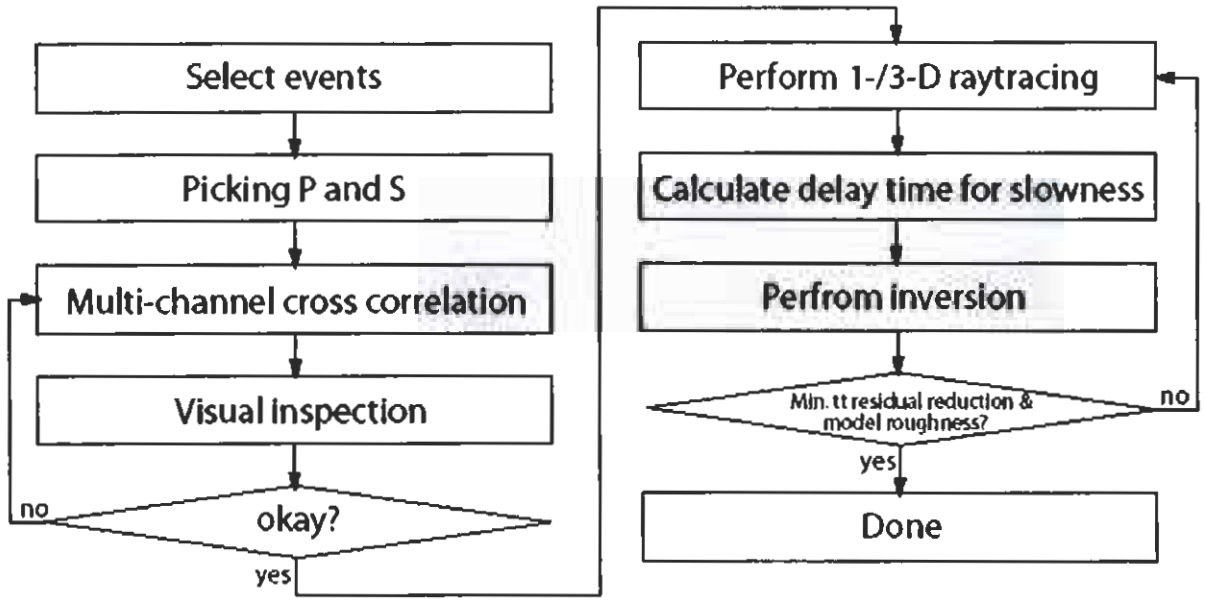

Flow chart of data reduction and travel-time inversion procedures.

4.3 Receiver Functions

The use of P wave receiver functions to infer the existence of major crustal and upper mantle discontinuities has become a standard technique in seismology. These methods are described elsewhere (e.g., *Langston,*1979; *Owens et al* 1984; *Ammon,*1991) and consist of deconvolving the vertical P wave component from the radial (and possibly tangential) component to expose P-to-S converted waves in the P wave coda. The timing and amplitude of these conversions are then modeled or incorporated in inversion algorithms to infer S wave velocity models and the depth to the discontinuities. We performed P wave receiver function studies for some stations of the network. To image crustal structure, we combined the receiver functions with surface wave dispersion measurements out to 30 sec using the joint receiver function/surface wave inversion method of *Julia et al.*(2000). This method, then, provides a simple way to control trade-offs between fitting the receiver functions and the dispersion curves (normalized by the data uncertainty and number of

points), and also the trade-off between fitting the data and model smoothness. Both smoothness and weighting parameters are estimated empirically, after running a suite of inversions.

The combination of receiver functions with surface wave dispersion measurements allowed us to place tight constraints on average crustal S velocities and Moho depths.

4.4 Teleseismic Shear Wave Splitting

The most abundant and highly anisotropic upper mantle mineral, olivine, develops preferred lattice orientations when deformed in the dislocation creep regime (*Karato,*1998). For large strains, the olivine axes become parallel to the direction of shear. Therefore, measurements of seismic anisotropy can be used to investigate mantle deformation. While seismic anisotropy has been studied in several diverse tectonic settings, its interpretation in many cases is still enigmatic. No tectonic environment has been more difficult to understand than rift zones. Since *Hess* (1964) pioneering study of anisotropy in ocean basins, it has been expected that extension should align fast directions of olivine parallel to the rifting direction through shear in the lithosphere or asthenosphere. However, recent studies of seismic anisotropy from SKS splitting in the Basin and Range (*Savage et al.,*1990), the Rio Grande Rift (*Sandvol et al.,*1992), the Baikal Rift (*Gao et al.,*1997) and an area adjacent to the Red Sea Rift Zone (*Wolfe et al.,*1999 ; *Hansen et al.,* 2006) have not found extension parallel fast directions. This suggests that flow in the asthenosphere is not completely driven by surface tectonics.

The anisotropic signature beneath continental rift zones can provide important constraints on the mechanism of extension. For example, a passive model of continental rifting, where the entire lithosphere is extended below the rift, would be expected to produce a lattice preferred orientation (LPO) of olivine aligned parallel to the direction of extension. Active rifting, involving thinning of the lithosphere through small-scale convection, might result in more complex flow and therefore

more complicated LPO alignments, depending on the details of the small scale convection. In addition to LPO developed during mantle flow, alternative models for seismic anisotropy beneath rift zones include fossil LPO frozen into the lithosphere during a previous tectonic event and the alignment of magmatic cracks. These magma filled cracks are expected to align themselves perpendicular to the least compressive stress direction, resulting in rift parallel fast polarization directions. This mechanism is analogous to extensive dilatancy anisotropy, where parallel alignment of vertical, fluid-filled microcracks in the crust produces anisotropy. It has been suggested as the dominant cause of anisotropy beneath the Rio Grande and East African Rifts (*Gao et al.*, 1997).

Results of previous research found a fast polarization direction parallel to the Red Sea Rift's spreading, by modeling far-regional surface waves (*Schwartz et al.*,2000). That study estimated crustal and upper mantle velocity structures for the Red Sea Rift Zone were derived by modeling regional and far-regional body and surface waveforms. The best-fit model had a 17 km thick crust with anomalously low upper mantle velocities (Vp=7.7 km/s) underlain by a significant low velocity zone. Velocity models that fit the radial and vertical waveforms are unable to accurately predict the Love wave on the transverse component. Including 3-4% faster SH than SV velocities in the upper mantle replicates the Love wave and points to a fast anisotropic polarization axis parallel to the rift's spreading direction. These results are in direct contradiction to the SKS splitting results of *Wolfe et al.* (1999) and require further investigation of the anisotropic structure beneath the Red Sea Rift zone to understand its origin and relationship to the geodynamic processes involved in continental rifting.

Here we used the KACST data set to address this very important problem. Specifically, we measured teleseismic shear wave splitting in S and SKS phases recorded by 26 broadband stations of the KACST network that border the Red Sea in Saudi Arabia. S and SKS splitting parameters were analyzed for the possibility of lateral variations in anisotropic structure and dipping symmetry

axes. Dipping symmetry axes were not considered in any of the previous studies of rift zone anisotropy, but may be able to reconcile the apparent difference in fast polarization directions obtained from body and surface waves for the Red Sea Rift Zone. Regional and far-regional surface waves from moderate sized events in the Red Sea region recorded by all available stations in the area were modeled to increase the surface wave observations and confirm or refute our previously obtained extension parallel fast propagation direction. The S, SKS and surface wave anisotropy results were combined in an attempt to construct a consistent model for mantle flow beneath this rift zone.

The study of *Wolfe et al.* (1999) as well as most shear wave splitting studies concentrate on the SKS phase and average individual splitting measurements (fast polarization directions and delay times) made from events at various back-azimuths to obtain station averages. SKS is the favored phase because it passes through the liquid outer core and any effects of source-side splitting are obliterated due to its complete conversion to compressional motion in the outer core. This property of outer core traversing waves renders them very powerful to study receiver side anisotropy. The tendency to average individual splitting parameters is primarily due to the relatively small number of observations at each station (since SKS phases alone are favored) and large measurement errors. Averaging splitting parameters implicitly assumes that the anisotropy is adequately described by a single anisotropic region of hexagonal symmetry with the olivine axes oriented horizontally, thus implying horizontal flow. This may not always be a valid assumption so rather than averaging individual splitting parameters obtained from different events to produce station averages, we analyzed the dependence of splitting parameters on arrival directions. This allowed us to determine: 1) if waves from different directions sample different anisotropic regions; and 2) if the anisotropic medium has a symmetry that is more general than hexagonal with a horizontal symmetry axis.

Although S phase splitting is more difficult to interpret than SKS, since its splitting could have occurred anywhere along its propagation path, the inclusion of S phases greatly increases the range of available incidence angles and back azimuths and allows interpretation of individual splitting measurements. We incorporate S wave splitting in this study and remain aware of the possibility of source-side anisotropy for the S phases. We however, preferably analyzed S phases from deep focus events to minimize this effect.

We used the horizontal velocity traces to obtain the splitting parameters. For SKS phases we rotated and shifted the two components to find those parameters (polarization direction, phi and delay time,) that minimize the energy on the transverse component and render the particle motion most linear, that is, we minimized the smallest eigenvalue of the covariance matrix. For S we used this covariance method. Measurement errors were estimated by the commonly used F test method.

4.5 Regional and far-regional surface wave modeling

While knowledge of the velocity structure of northeastern Africa is important for understanding its tectonic development, progress has historically been hindered by both a lack of large African earthquakes and the sparseness of seismic stations at regional distance from seismic sources. Although large African earthquakes are still quite rare, station coverage in the area of the Red Sea Rift is now sufficient for regional waveform modeling of relatively pure paths traversing the Red Sea. We tested and refined our previously derived model of the crust and upper mantle structure beneath the Red Sea Rift zone through waveform modeling at regional and far-regional distances. Events with high signal to noise with known focal mechanisms were culled to insure that the data possess distinct compressional, shear, and surface wave arrivals. Processing and modeling of the data were proceed following procedures used by *Rodgers and Schwartz* (1998) and *Rodgers et al.* (1999) and includes:

1) deconvolution of the station response to ground displacement;
2) initial band-pass filtering between 5-100 seconds;
3) rotation of horizontal components to the great-circle coordinates; and
4) application of a grid-search algorithm to determine crustal and mantle parameters that best-fit both the surface and body waves in the period ranges between 20-100 s.

Modeling surface and body waves together provides better constraints upon the crustal and upper mantle structure than modeling selected portions of the seismograms because it includes information about the surface wave group and phase velocities plus the body wave arrival times and their relative amplitude to the surface waves.

Using a range of velocity and layer thickness parameters, a suite of models is created and synthetic reflectivity seismograms (*Randall*, 1994) generated for each. The best parameters are chosen by calculating a normalized least-squares misfit between the data and synthetic components. Initial iterations focus on constraining the crustal velocities and thickness through fitting the absolute timing, amplitude, and dispersion of the Love and Rayleigh surface wave packets. Later iterations involve varying lid and upper mantle thickness and gradients, allowing shear velocity to increase independently of the P/SV velocity structure if necessary to fit the transverse and radial component surface waves and the P and S body wave arrivals and amplitudes.

V. RESULTS & INTERPRETATION

5.1 Teleseismic Travel Time Tomography

We determined detailed models of compressional and shear velocities of the crust and upper mantle down to about 400 km using teleseismic receiver functions and P- and S-wave travel time tomography. The state of strain in the upper mantle was determined from teleseismic shear wave splitting. Deep receiver functions were sampled the upper mantle transition zone discontinuities at 410 and 660 km. The resulting models provided new constraints on tectonic models of the rupturing of continental lithosphere and the source of volcanism in the Arabian Shield.

Rayleigh wave dispersion curves have been measured using the array methods of *Menke and Levin* (2002) as shown in Figure 5.1. The figure shows path coverage for three period bands centered at 22 s, 60 s and 150 s. The fourth panel shows the Rayleigh wave dispersion curve for the inter-station path between KACST station (ARSS) and BDAS in Ethiopia. The coverage is quite good for this data set (*Park et al.*,2005).

In this study, the tomographic inversion method uses a multi-channel cross-correlation (*Van Decar and Crosson*, 1990) to find the optimal set of relative delays between teleseismic P-wave arrivals at the entire KACST network. Tomography requires many crossing ray paths in order to isolate the locations of velocity anomalies below the network. The method uses an iterative non-linear ray tracing algorithm to allow for ray bending 3-D structure.

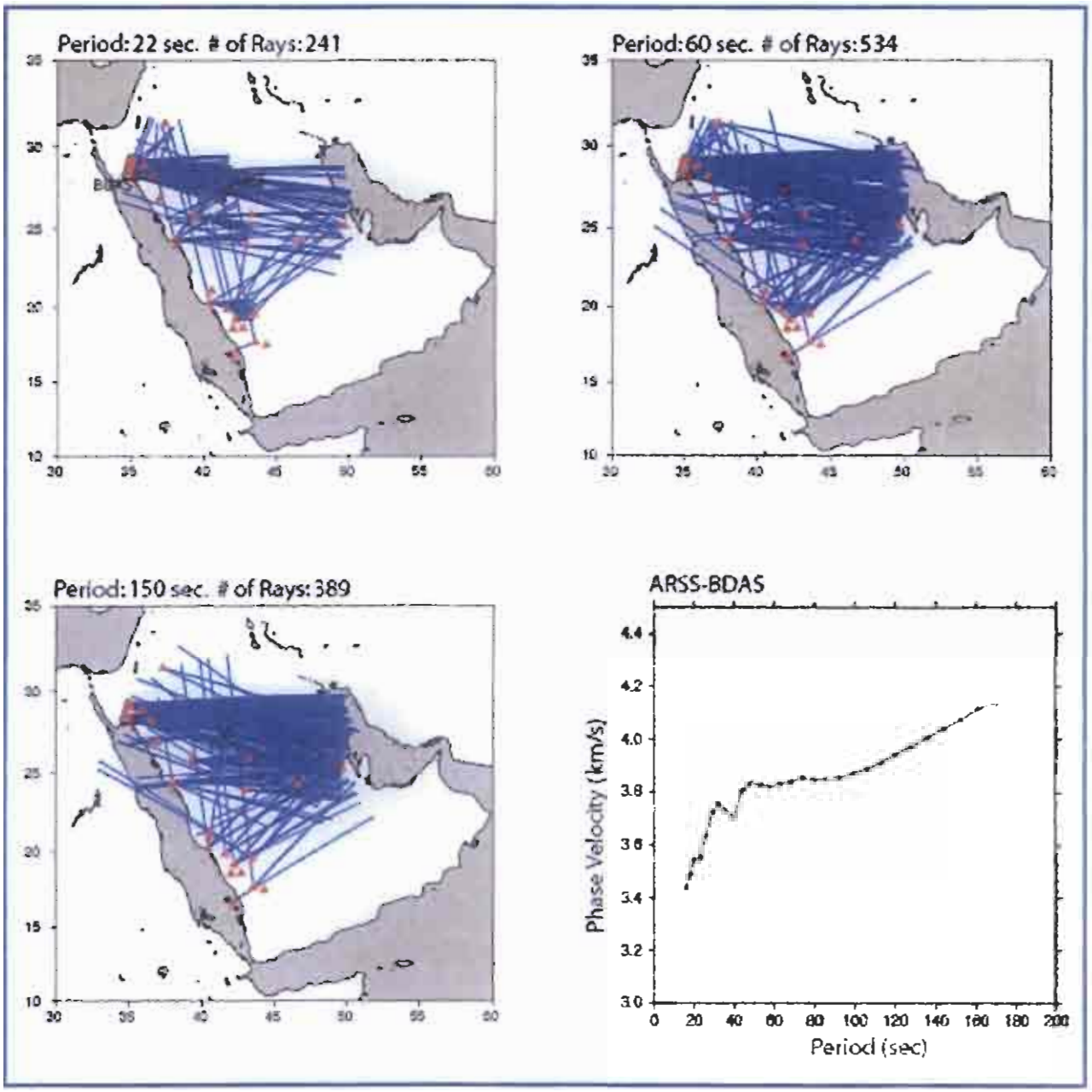

Figure 5.1. Rayleigh wave dispersion curves for three period bands centered at 22 s, 60 s and 150 s. The fourth panel shows the Rayleigh wave dispersion curve for the inter-station path between KACST station ARSS and BDAS in Ethiopia.

For P-wave model, we used 401 earthquakes resulting in 3416 ray paths with P- and PKP-wave arrivals. The majority of the events are located in the western Pacific Rim between back azimuths of 15 and 150 degrees, but the events are distributed over a wide range of back azimuths (Figure 5.2a). The waveforms were filtered with a zero-phase two-pole Butterworth filter between 0.5 to 2 Hz, and relative P-wave travel time residuals were computed (*Park et al.*,2005).

For the S-wave model, we used 201 earthquakes resulting in 1602 ray paths with S-and SKS-wave arrivals. Although the total number of rays for S-wave model is a half of the rays for the P-wave model, the event distribution shows better coverage of back azimuth (Figure 5.2b). The signal processing procedures for S-wave are exactly same as P- wave data, but traces are filtered with lower frequency band (0.04 to 0.1 Hz), relative arrival time residuals are computed by the multi-channel cross-correlation (MCCC) method with fifteen-second time window (*Park et al.*,2005).

The resulting tomographic images of upper mantle structure at depths of 100-400 km are shown in Figure 5.3. P-wave velocities vary by ±2% beneath Arabia. Slower than average velocities are generally beneath the Arabian Shield and faster than average velocities beneath the Arabian Platform. However, a striking feature is the low velocities extending through the upper mantle beneath the eastern edge of the Arabian Shield (beneath Riyadh). This feature can be seen in the cross-sections shown in Figure 5.4.

For comparison, we show the upper mantle P-wave velocity model of *Benoit et al.* (2003) in depth slice and cross-section view in Figures 5.5 and 5.6, respectively. The study used data from the 9 station IRIS-PASSCAL Saudi Broadband Deployment (*Vernon et al.*, 1998). In fact the sampling is complementary with the PASSCAL data covering north-south and northeast-southwest trending zones across the Arabian Shield beneath the stations. As can be seen in Figures 5.5 and 5.6, the resolution and lateral extent of the area imaged using the Saudi Arabian Broadband Deployment (SABD) data set is quite limited.

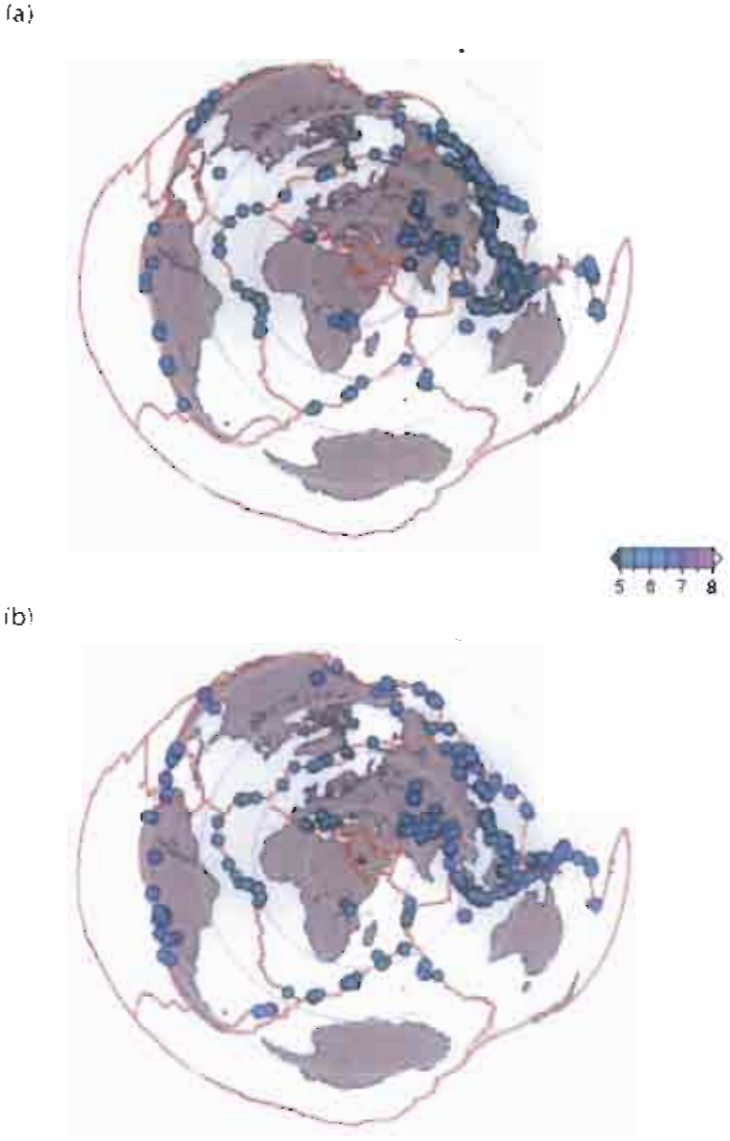

Figure 5.2. The distribution of earthquakes for (a) P wave (3416 rays from 401 events) and (b) S wave (1602 rays from 201 events) plotted by the equal distance projection. The color s scale indicates magnitude of each event, the red solid lines show plate boundaries, and each circle represents 30 degree distance interval from the center of KACST seismic array.

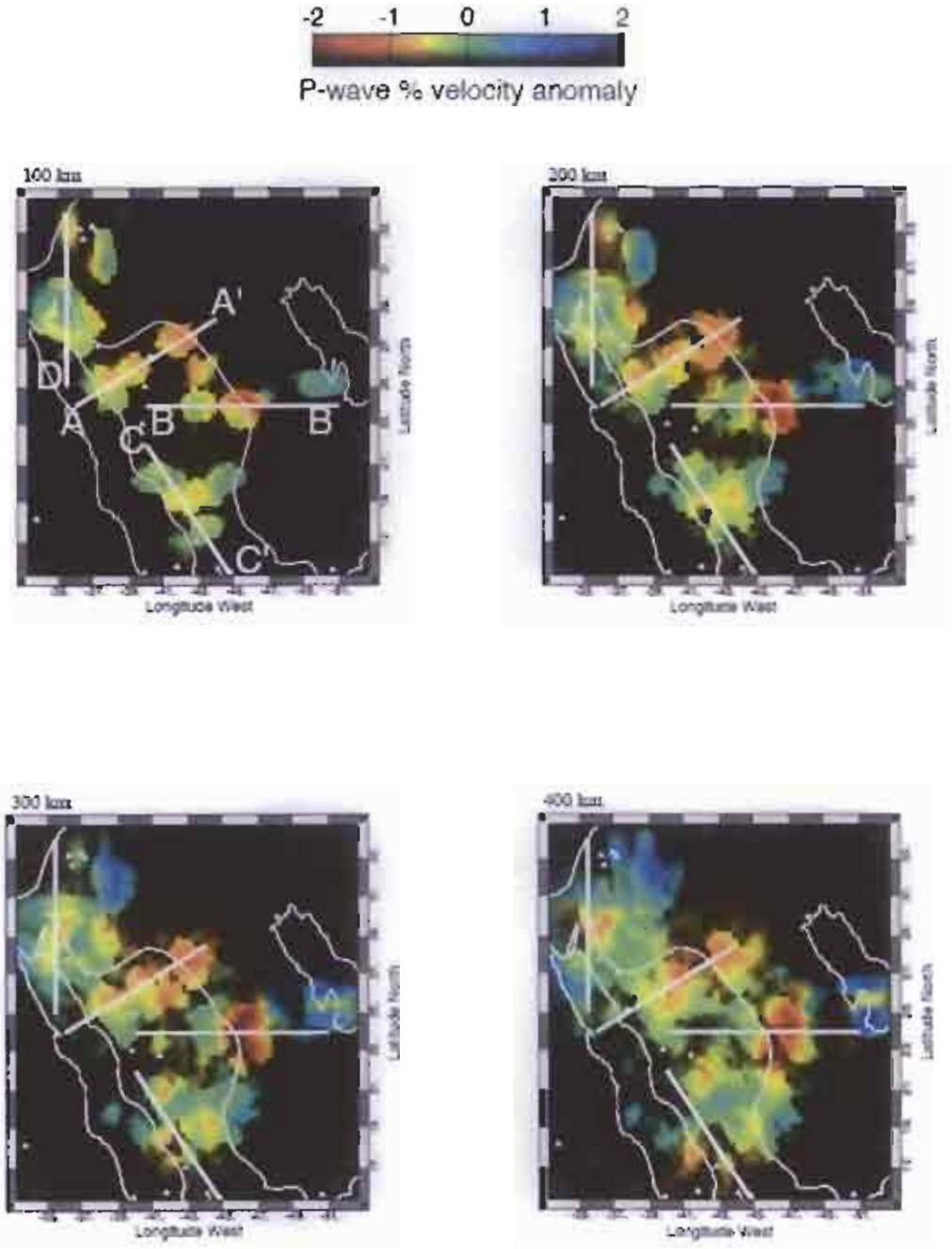

Figure 5.3. P-wave velocities in the upper mantle at depths of (a) 100, (b) 200, (c) 300 and (d) 400 km depths. Velocities are plotted with the color scale as the relative perturbation to the average one-dimensional background model. The locations of cross-sections through the model are indicated by the white lines.

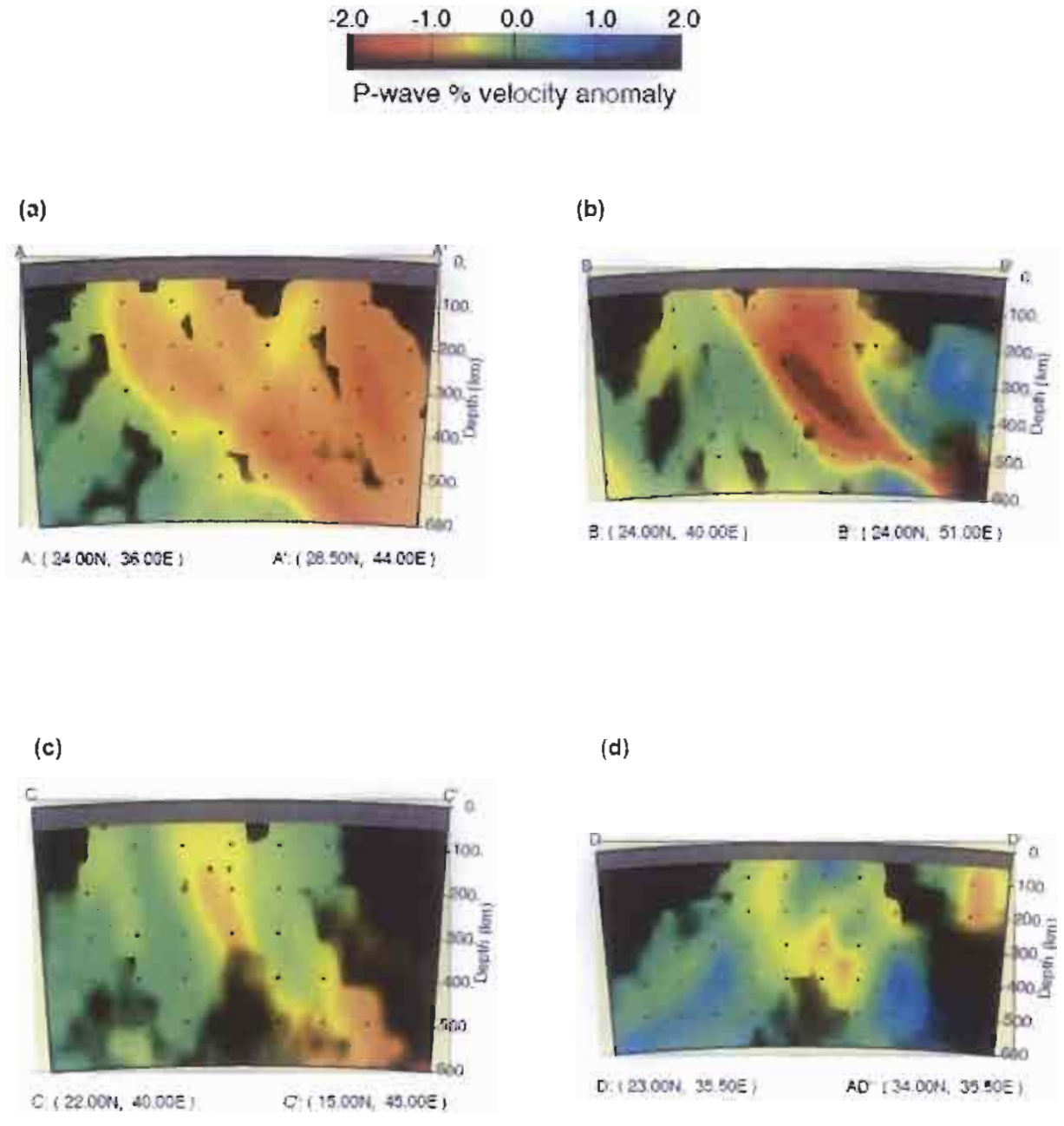

Figure 5.4. Cross-sections through the upper mantle tomography model: (a) A-A' across the northern Arabian Shield; (b) B-B' across the shield-platform boundary; (c) C-C' along the southern Red Sea coast (Asir Province); and (d) D-D' along the Gulf of Aqabah and the Dead Sea Rift.

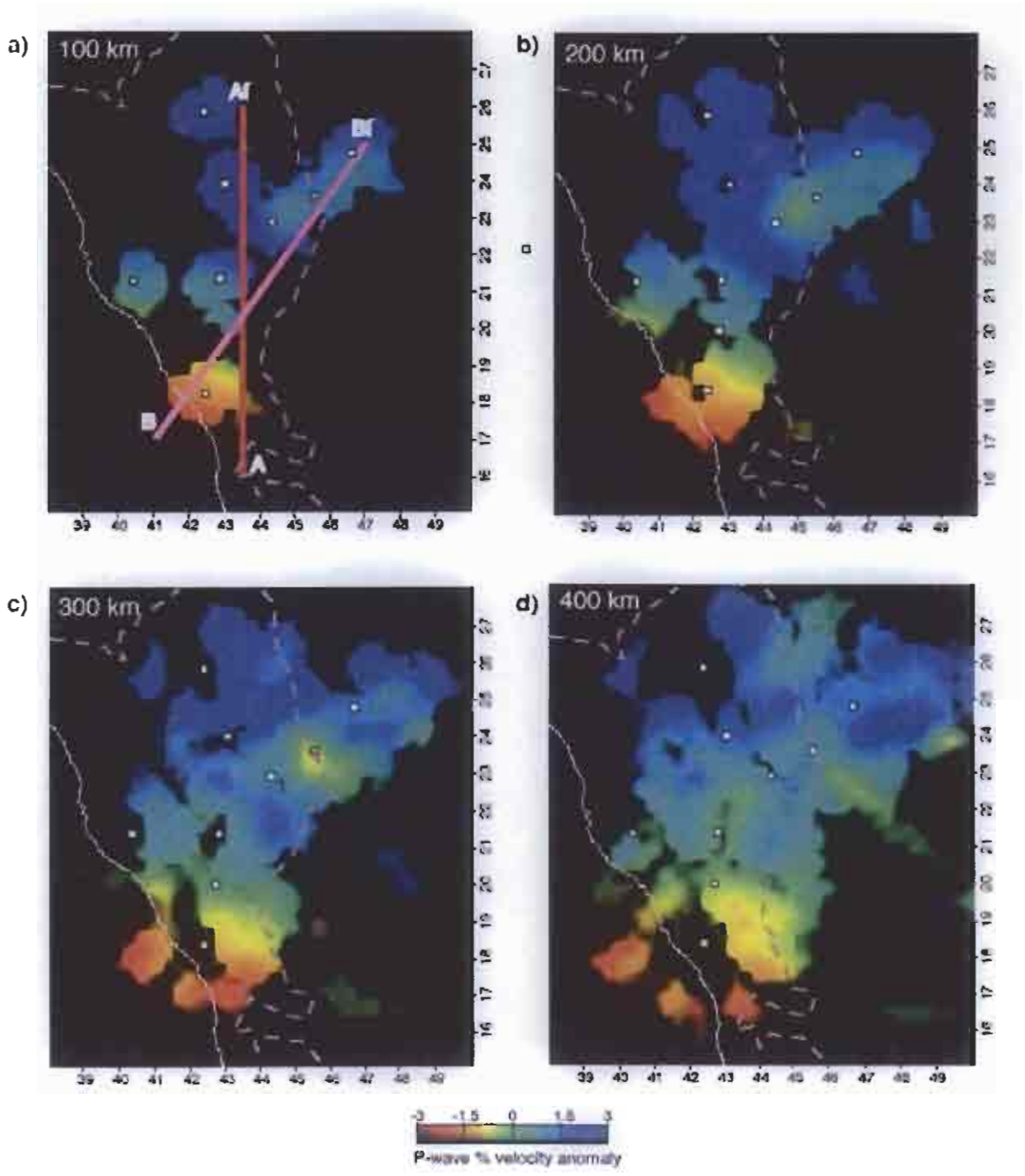

Figure 5.5. Tomographic model of *Benoit et al.* (2003). P-wave velocities in the upper mantle at depths of (a) 100, (b) 200, (c) 300 and (d) 400 km depths. Velocities are plotted with the color scale as the relative perturbation to the average one-dimensional background model. The locations of cross-sections through the model are indicated by the red lines.

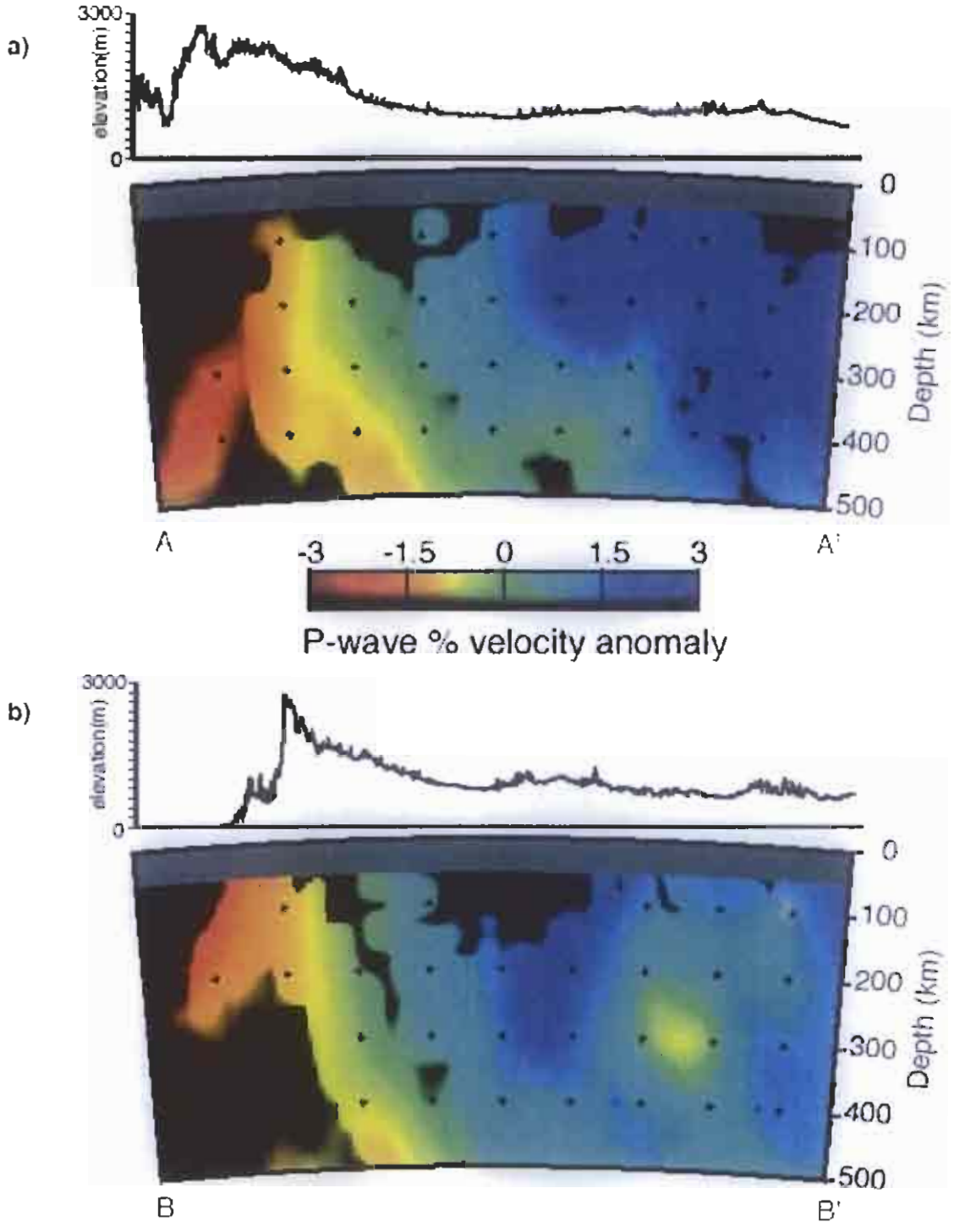

Figure 5.6. Cross-sections through the upper mantle tomography model: (a) A-A' north-south section across the Arabian Shield and (b) B-B' southwest-northeast section from the Red Sea across the Arabian Shield to the Arabian Platform.

5.2 Resolution tests

To test the resolution of our P- and S-wave model, we produced a synthetic checkerboard model consisting of 100 km diameter spheres with ± 5% slowness anomaly placed at 100, 400, and 700 km depths (Figures 5.7 and 5.8). Ray paths through a 1-D reference mode as defined by the IASP91(*Kennett and Engdahl,* 1991) are used, and noise is added to the synthetic, travel-times as a Gaussian residual time error by a standard deviation of 0.02 and 0.04s for the P and S wave data, respectively. Figures 7 and 8 show the recovered structure from the checkerboard test for P - and S- wave velocity perturbations, respectively. The input spheres are retrieved below 200 km depth (Figure 5.7e-h for P-wave tomography, and Figure 5.8e-h for S-wave tomography), and the amplitudes of the slowness anomalies is recovered by ~20% of input anomaly. Since the spacing of seismic stations is sparse, and the ray paths of teleseismic body-waves are incident vertically near the surface, the velocity perturbations set at 100 km depth were recovered with very small anomaly values in our model. However, the cross-section images of P- and S-wave models show that the pattern of the retrieved models are reliable between 200 km and 400 km depth (Figure 5.7g and h, and Figure 5.8g and h).

Generally speaking, we would suggest that low velocity beneath the Gulf of Aqabah and southern Arabian Shield and Red Sea at depths below 200 km are related to mantle upwelling and seafloor spreading. Low velocities beneath the northern Arabian Shield below 200 km may be related to volcanism. The low velocity feature near the eastern edge of the Arabian Shield and western edge of the Arabian Platform could be related to mantle flow effects near the interface of lithosphere of different thickness.

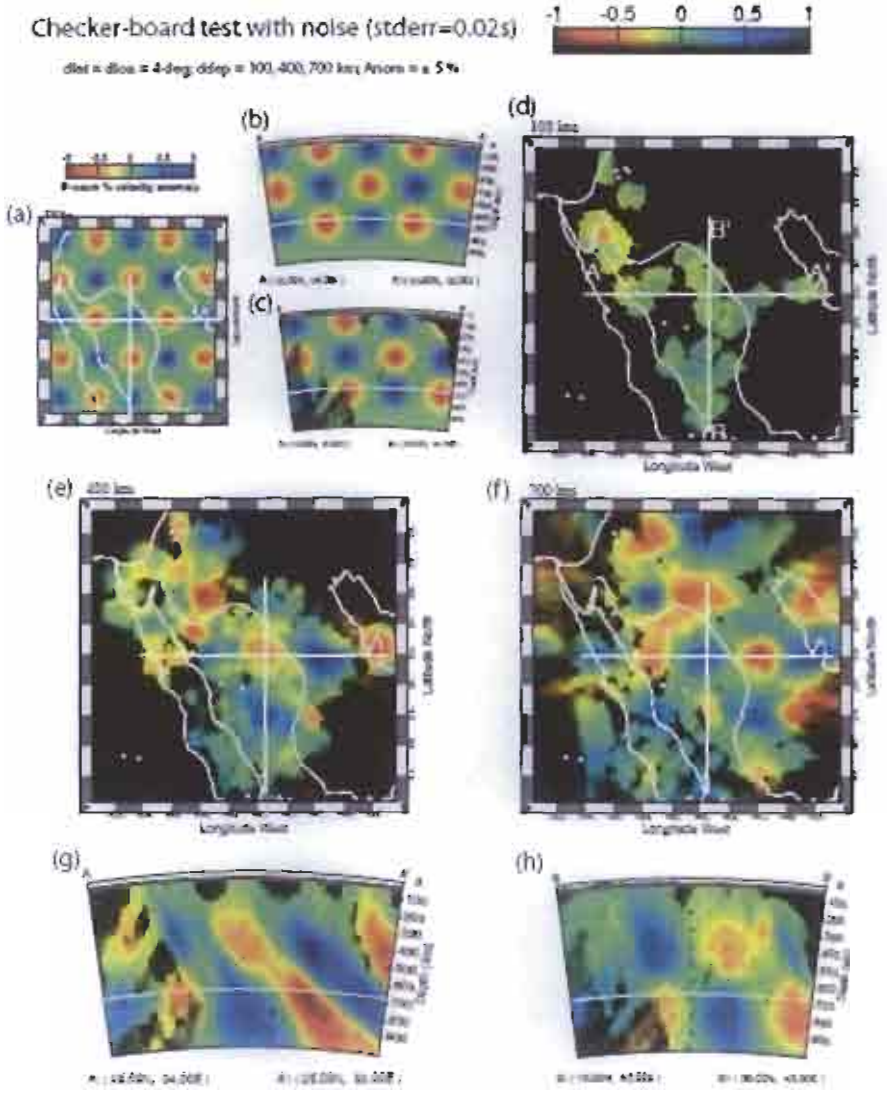

Figure 5.7. Synthetic checker board resolution test for inverted P-wave model. (a) shows the 100 km depth profile of input model, and (b) and (c) show the cross sections located on (a). 100 km diameter spheres defined by Gaussian functions across their diameter of ± 5% peak velocity anomaly are distributed in layers of depth 100, 400 and 700 km. (d), (e) and (f) are the 100, 400 and 700 k km depth profiles inverted from input model, and (g) and (h) are the cross cross-sections.

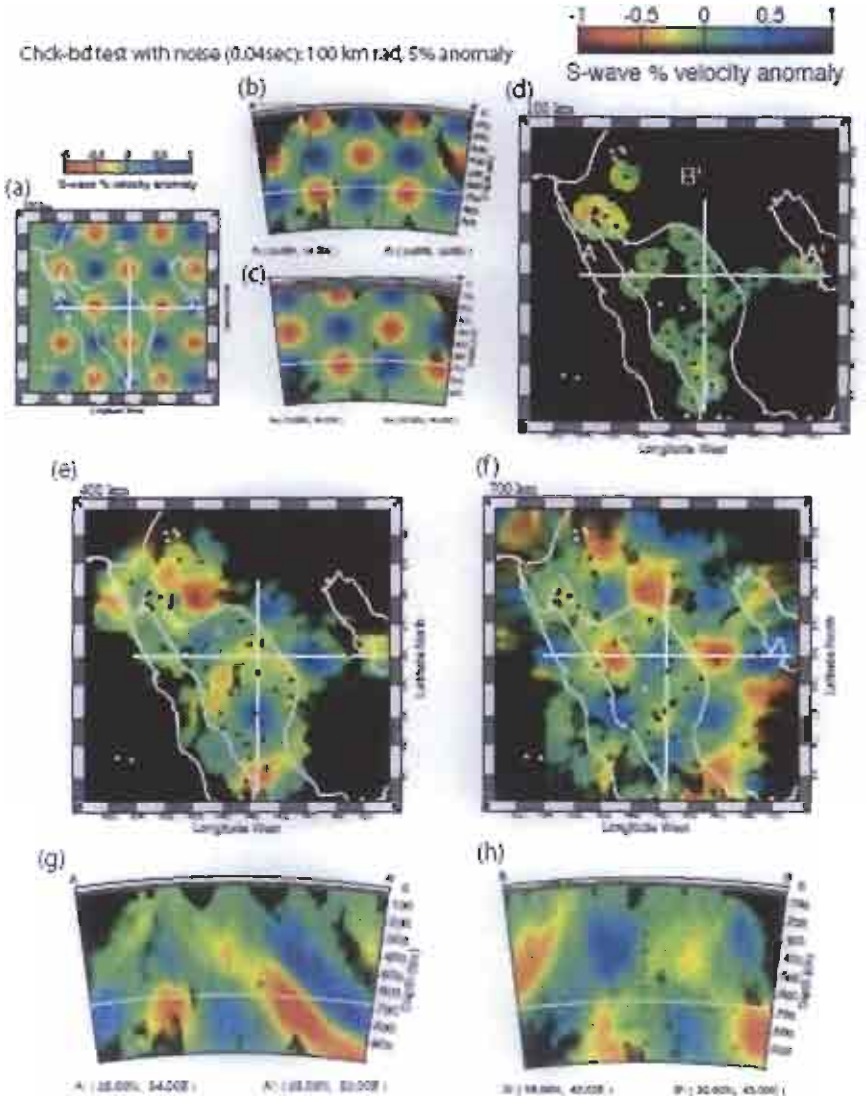

Figure 5.8. Synthetic checker board resolution test for inverted S-wave model. (a) shows the 100 km depth profile of input model, and (b) and (c) show the cross sections lo located on (a). 100 km diameter spheres defined by Gaussian functions across their diameter of ± 5% peak velocity anomaly are distributed in layers of depth 100, 400 and 700 km. (d), (e) and (f) are the 100, 400 and 700 km depth profiles inverted from input model, and (g), and (h) are the cross cross-sections.

5.3 Crustal Structures from Teleseismic Receiver Functions

The detailed structure of the Moho has been one of the most important targets in the earth sciences since its discovery by *Mohorovicic* (1910). Seismic refraction and reflection techniques have provided relatively high resolution images regarding the physical and structural properties of the Earth's lower crust and upper mantle. The detailed architecture of the crust-mantle transition is the most significant asset in unraveling the lithospheric processes that are involved in extension and in collision zones and provide key knowledge in processes like crustal growth and accretion.

Since the beginning of broadband digital seismometry in the late 1970's, teleseismic receiver functions have been used to estimate regional crustal structure (e.g. *Langston*, 1979; *Owens*, 1987; *Owens et al.* 1987; 1988; *Ammon et al.,* 1990; *Ammon,* 1991). This widely applied method deconvolves the vertical component P-wave from the radial component to isolate the shear-wave response of the crust and upper mantle beneath the recording station. RF's are very sensitive to changes in seismic velocities (i.e. discontinuities), however are only weakly sensitive to absolute velocities. Methods to model crustal structure with RFs have relied on formal inversion (e.g. *Ligorría and Ammon*, 1999; *Ammon et al.,* 1990) or grid search (e.g. *Sandvol et al.,* 1998).

There were several studies recently however, in which RF's were jointly inverted with surface wave dispersion for crustal structure (*Özalaybey et al.,* 1997, *Du and Folger*, 1999; *Julià et al,* 2000). These methods have the advantage of improved sensitivity to absolute velocities compared to RFs alone.

Teleseismic RF's were calculated for stations in the Arabian Peninsula in a number of studies. For example, *Sandvol et al.* (1998) estimated lilthospheric structure of the Arabian Shield by modeling of receiver function stacks from teleseismic P waves recorded at the Saudi Arabian Portable Broadband Deployment data (*Vernon and Berger*, 1997). *Julià et al.* (2003) presented velocity

models for the same stations, combining RF with surface wave dispersion data to invert for structure. *Al-Damegh et al.* (2005) calculated RF's for the Arabian Plate from permanent broadband stations in Saudi Arabia (*Al-Amri and Al-Amri*, 1999) and Jordan (*Rodgers et al.*, 2003a).

In this study, a numerous teleseismic earthquakes recorded at 7 broadband seismic stations in Saudi Arabia (AFFS, HAQS, HASS, HILS, KBRS, TATS, and TBKS) was analyzed to estimate the Moho depth at each station from the receiver function.

We estimate teleseismic RFs from high-quality waveform data. A raw data for RF analysis consist of 3-component broadband velocity seismograms (fig.5.9) for earthquakes with magnitudes M_w > 5.8 and epicentral distances between 30° and 90°. Most of the seismicity occurring at epicentral distances suitable to use for the receiver function method are confined in the western part of the Pacific Rim, from the Kuril Islands in the north to the Indonesia in the south.

In order to produce radial receiver functions at each station, we used the time-domain iterative deconvolution procedure described in *Ligorría and Ammon* (1999). Prior to applying the deconvolution procedure, we cut traces at 60 seconds before and 120 seconds after the main P arrival. Resulting receiver functions from a number of earthquakes could be stacked and averaged for a range of back-azimuths. However averaging can result in reducing the amplitudes of some important features, especially at later times of the receiver function time series where signal from the crust is weak. Therefore, a special care is taken in selecting only mutually coherent waveforms, resulting from at least 10 or more earthquakes. We also checked how RFs vary at each station with azimuth of the incoming waves and found that this variation is not very significant. If the number of waveforms is quite large, we have a comfort of using only data from a relatively narrow sub-range of available back-azimuths at similar epicentral distances.

In the time domain, the observed P-wave arriving at a seismic station from a teleseismic event is the composite of the seismic source function, the impulse response of the recording instrument, and the

impulse of the local (near receiver) earth structure. In order to combine the information contained in many events, each with different seismic source function, an estimate of the receiver function requires an effective means of isolating the source effect from the observed seismograms. The source equalization procedure proposed and discussed by *Langston* (1979) is an effective procedure to isolate the local earth structure effects. For this study, we have calculated the receiver functions using the time domain methods (*Ligorria and Ammon,1999*). The foundation of time-domain iterative techniques is a least-square minimization of the difference between the Gaussian filtered observed horizontal seismogram and a predicted signal generated by the convolution of an iteratively updated spike train with the vertical component seismogram (*Ligorria and Ammon*, 1999).

The resolution of receiver function technique has increased with the utilization of digital broadband data. This increased resolution of fine structure extends to an increased sensitivity of receiver function to shallow structure interface with high-velocity contrast (i.e. the sedimentary cover-basement rock contact).

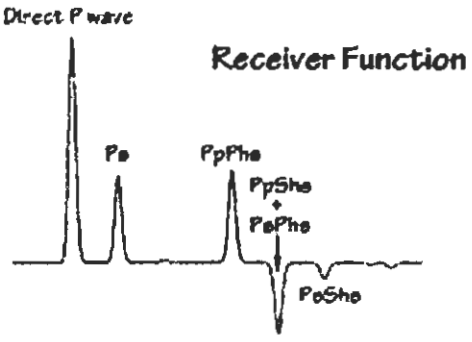

The first arrival, denoted by p in as shown below, arises because of the partition of the incident P wave into vertical and radial components at the surface. The subsequent arrivals correspond to the partition of S wave incident. A Ps corresponds to an S-wave created by conversion of the teleseismic

P wave into S at the Moho. Lateral arrivals correspond to structural reverberations. Different structure such as shallow structure, ray parameters, and velocity can affect the receiver function.

5.3.1 Interpreted Crustal Structures

Receiver function is scnsitive to the shear- wave velocity structure and has been used successfully to resolve boundaries at different depths and provide site specific information about the dip angle and direction of interface geometry. However, its inversion for shear-velocity structure is non-unique (velocity-depth trade-off) since there is very little absolute velocity information contained in thc receiver function. In order to define the Moho depth for each station, we used the depth at which the shear-wave velocity about 4.3 km/sec for the shield station and 4.55 for the platform stations (*Al-Amri et al.*,2004). This was necessary since, as wc will see, not all inverted models have sharp discontinuity in velocity at depths at which we would expect the Moho.

The seismic stations used in this study can be organized based on the tectonic setting and location. Stations AFFS, HILS, KBRS, TATS, and TBKS are located on the Arabian shield. Although station HAQS located on the Arabian shield it can be grouped to the Gulf of Aqabah region. The remaining station HASS is located on the Arabian platform.

The receiver functions for each event are calculated using the iterative time-domain deconvolution method. Each receiver function was deconvolved using 100 iterations with a limiting error of 0.001 for Gaussian factors of 0.5, 1.0 and 2.5. To reduce the influence low-frequency noise on receiver function, all the receiver functions were high-pass filtered with a two-pass Butterworth 0.02 Hz corner frequency filter (Fig. 5.10).

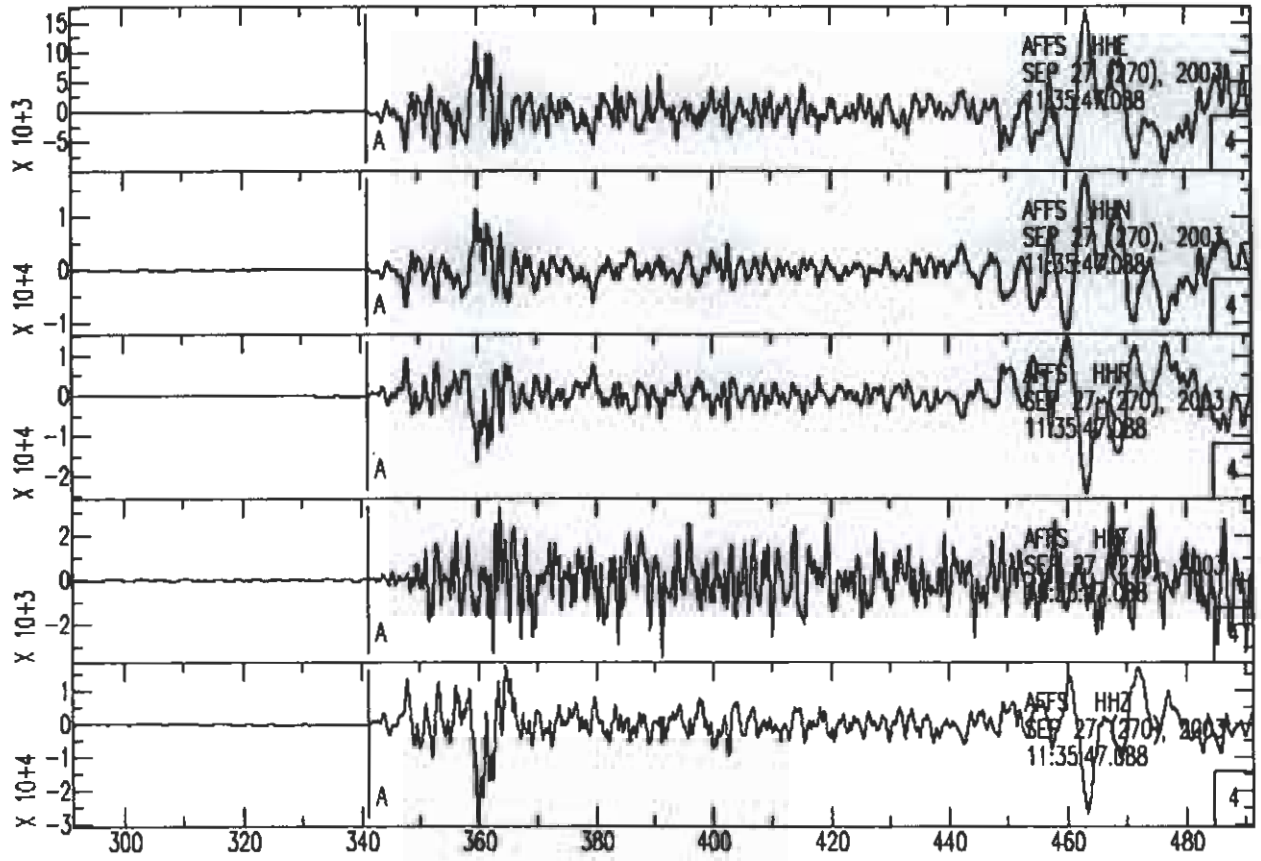

Figure 5.9 shows typical 3 component seismograms east-west, north-south, and vertical (E, N, and Z) accompanied with the rotated traces (R and T) for a good earthquake that met all the criteria to compute receiver function. The digital 3 component seismograms are rotated to radial (R), tangential (T), and vertical (Z) components.

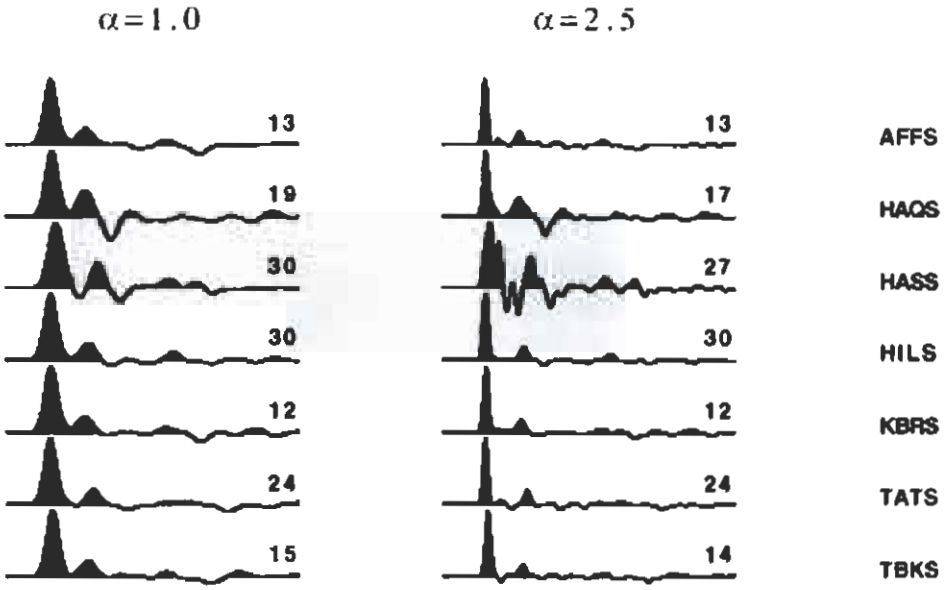

Figure 5.10. Stacked receiver function as a function of ray parameters. The figure shows the station name combined with the number of total receiver function used to invert the final earth model.

AFFS

Station AFFS is located on the Arabian Shield, and we do not observe sediments. The crustal thickness is about 36 km, with a fairly pronounced Moho. We stack 38 receiver functions for this station. We used the receiver function with Gaussian factors (0.5 1.0 2.5).

The inversion uses a one layer over half space as a starting model. The final shear velocity model for this station shows a high velocity layer for depths from 0 to 6 km with shear velocity of 3.0 km/sec. The first 6 km can be considered as the one upper crust layer. The middle crust has a velocity of 3.8 km/sec and extends 30 km depth. The lower crust (6 km thick) with average shear velocity of 4.2 km/sec extends until the Moho discontinuity at 36 km depth. The velocity is gradually increases until the Moho discontinuity (Fig. 5.18).

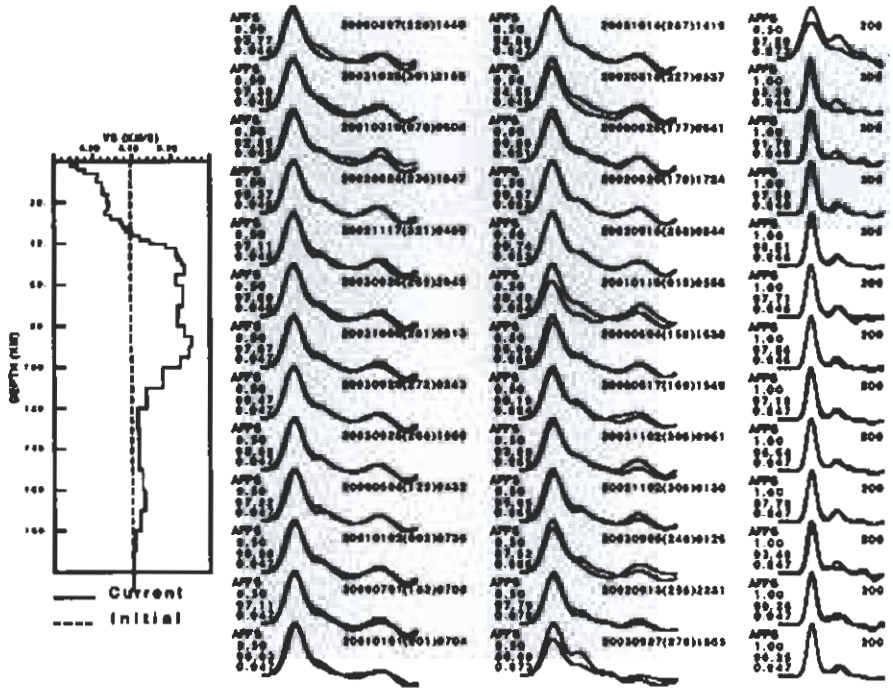

Figure 5.11. Left side plot is the final earth model inverted from the receiver functions. The right-side plot shows all the receiver function compute to do the inversion. The plot shows the station's name (AFFS), the Gaussian factors (α = 0.5, 1.0, and 2.5), the final fit between the observed and the predicted receiver function, ray parameters, and the earthquakes used.

KBRS

Station KBRS is an example of a station which has a simple crustal but a complex lithospheric structure. A gradational Moho between 35 and 38 km is found in our best model. For this station we stack 36 receiver function. The upper 4 km has a low shear velocity of about 3.3 km/sec. The next 6 km (4 to 10 km depth) form the second layer of the upper crust with a shear velocity of about 3.6 km/sec. the middle crust extends from 10 to 20 km with a shear velocity of 3.8 km/sec. The shear velocity is then increase gradually to 4.0 km/sec forming the lower crust with a thickness of about

10 km (20 to 30 km depth). For this station a sharp Moho discontinuity is identified at depth 36 km with a shear velocity of 4.45 km/sec. (Fig. 5.12).

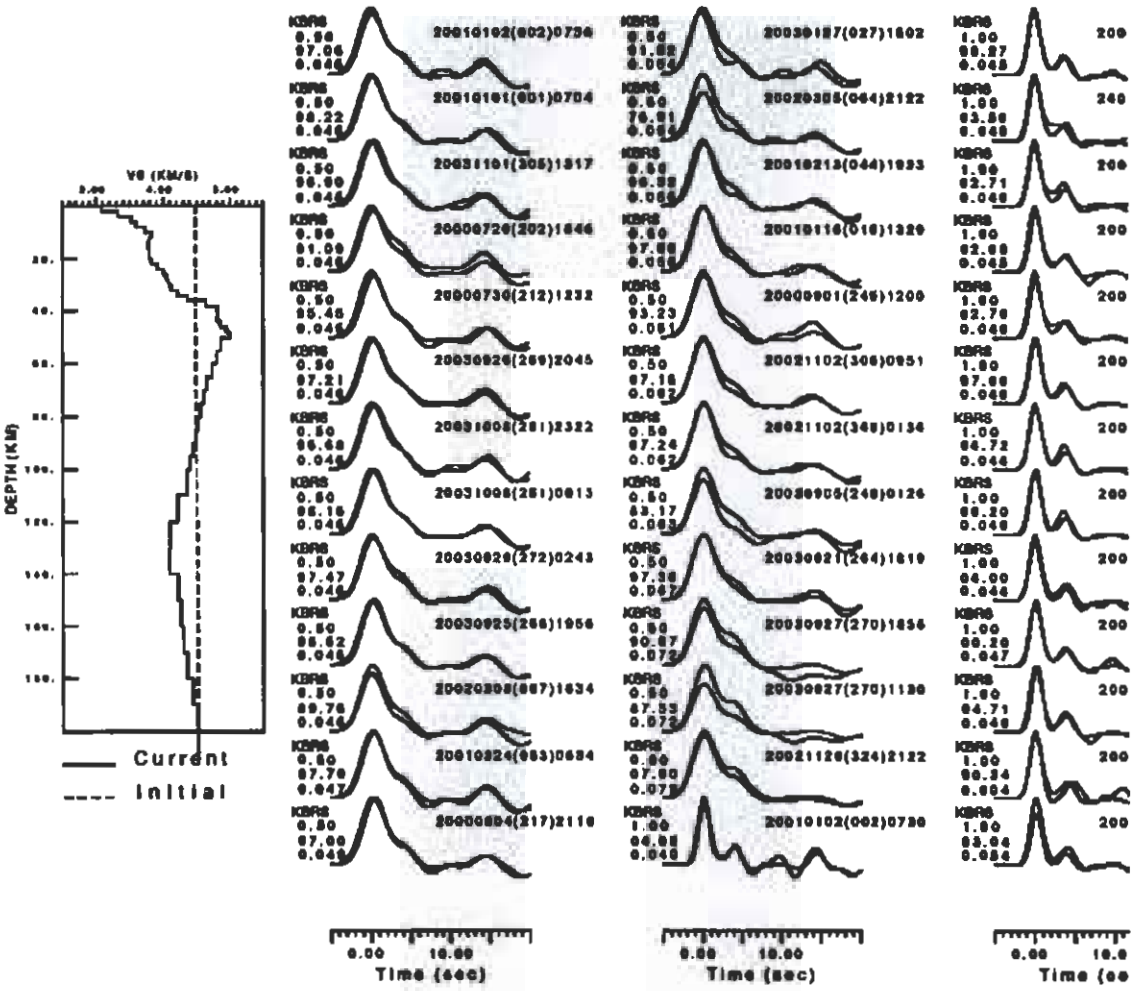

Figure 5.12. Left side is the final earth model inverted from the receiver functions. The right-side plot shows all the receiver function compute to do the inversion. The plot shows the station's name, (KBRS) the Gaussian factors (α = 0.5, 1.0, and 2.5), the final fit between the observed and the predicted receiver function, ray parameters, and the earthquakes used.

TBKS

We stack 44 receiver function for this station. Although we can locate the Moho discontinuity at 32 km depth, we can not trust the inverted model for this station. The inversion for this station has been affected by the shallow sedimentary layer (Fig. 5.13).

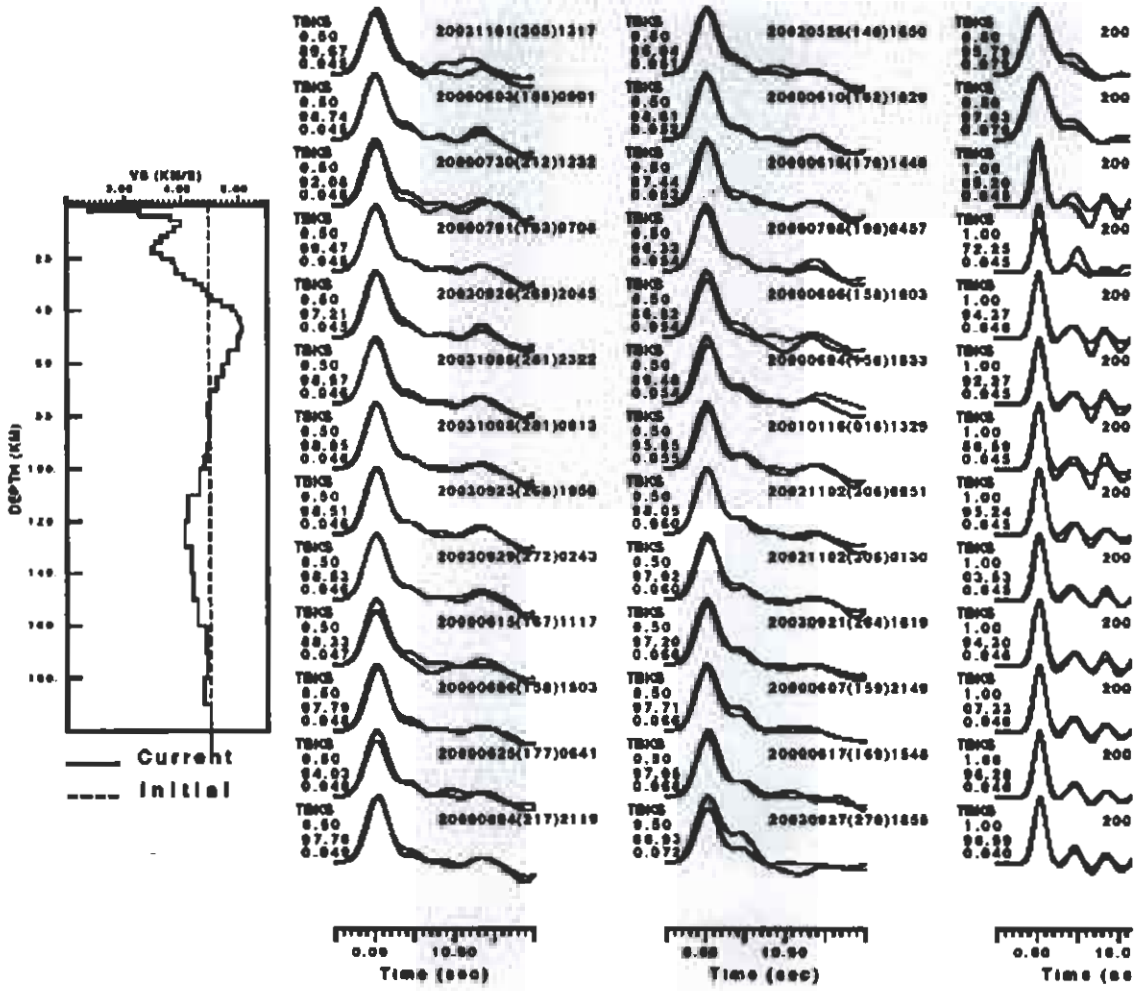

Figure 5.13. Left side is the final earth model inverted from the receiver functions. The right-side plot shows all the receiver function compute to do the inversion. The plot shows the station's name, (TBKS) the Gaussian factors (α = 0.5, 1.0, and 2.5), the final fit between the observed and the predicted receiver function, ray parameters, and the earthquakes used.

HILS

Station HILS is the best example of RF data that do not require a complex lithospheric structure to be explained jointly. The data from this station were also analyzed as the best data used in the study of *Al-Damegh et al.* (2005). We obtain a very similar crustal thickness as in that study. For this station we have been able to stack 30 receiver function. The final shaer velocity earth model show three distinct layers. The first layer extends to 6 km deep with shear velocity of 3.7 km/sec. The second layer extends between 6 to 24 km with shear velocity of 3.9 km/sec. the lower crust has a total thickness of 12 km (24 to 36 km) and shear velocity of 4.1 km/sec. For this station we identified a sharp crust-mantle transition at 38 km depth with a shear velocity of about 4.5 km/sec. (Fig. 5.14).

The velocity contrast at the Moho is fairly large and it appears that the lithospheric lid and low velocity zone are not strongly pronounced features in the lithospheric mantle under HILS. The Moho depth is at about 36-38 kilometers, which is comparable with the previous study of receiver functions of *Al-Damegh et al.* (2005).

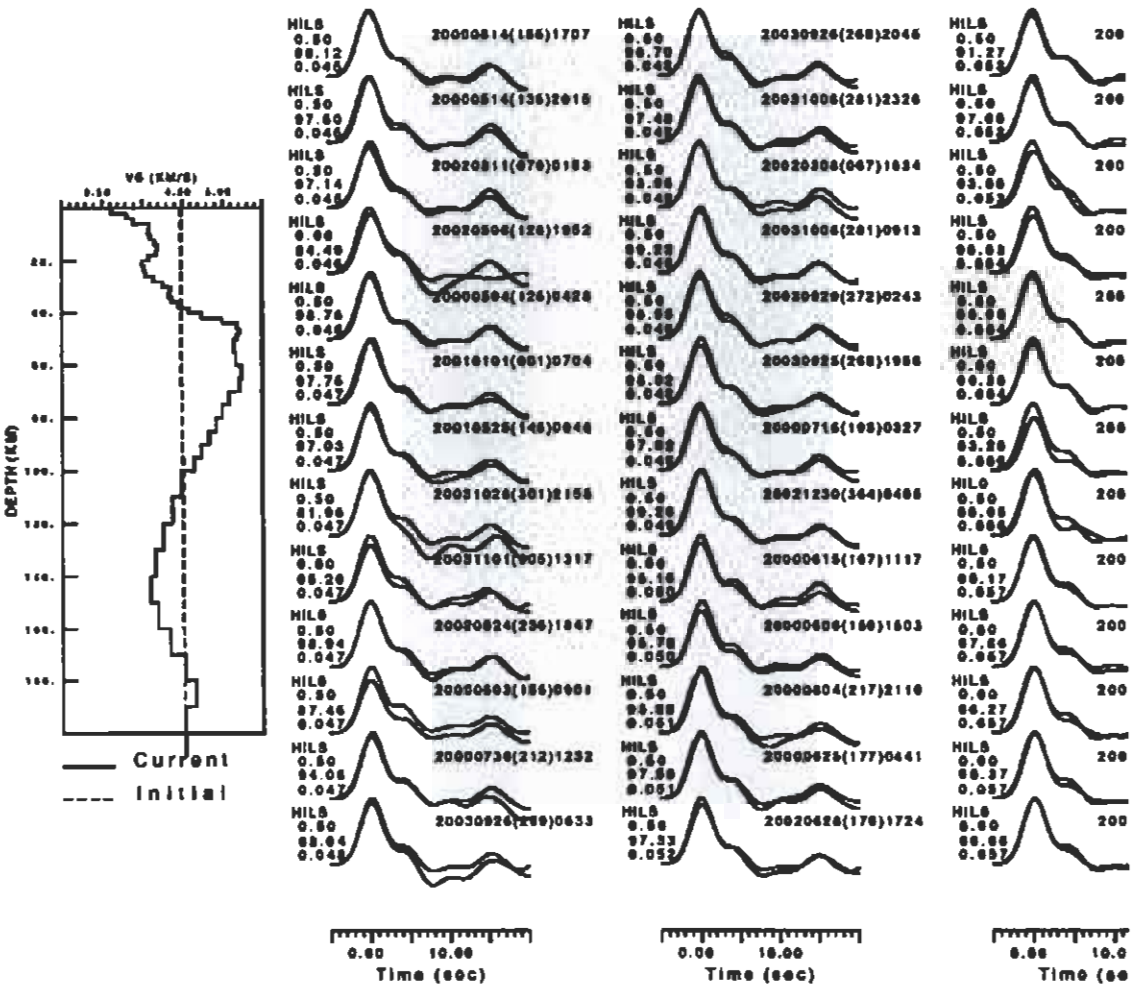

Figure 5.14. Left side is the final earth model inverted from the receiver functions. The right-side plot shows all the receiver function compute to do the inversion. The plot shows the station's name, (HILS) the Gaussian factors (α = 0.5, 1.0, and 2.5), the final fit between the observed and the predicted receiver function, ray parameters, and the earthquakes used.

HAQS

Station HAQS is adjacent to the Gulf of Aqabah and Dead Sea Rift. We stack more than 50 receiver function for this station. Based on the final shear velocity model, this station shows a low velocity layer of 3 km/sec with crustal thickness of about 4 km. the upper layer extends from 4 to 18 km depth with an average shear velocity of 3.5 km/sec. the velocity is gradually increases from the

depth 18 km to the crust-mantle transition. The Moho discontinuity can be identified based on the delay time from the receiver function at 35 km depth. The crust-mantle transition at this station is a clear example of the gradual discontinuity (Fig. 5.15).

Generally, our velocity model for HAQS features a few thin low-velocity layers near the surface, the crustal velocities are consistent with a slightly lower than average continental values and a Moho depth of about 35 km, consistent with the model obtained by *Rodgers et al.* (2003). The mantle is characterized by an anisotropic lid ($v_{SH} > v_{SV}$) approximately 55 km thick underlain by a LVZ.

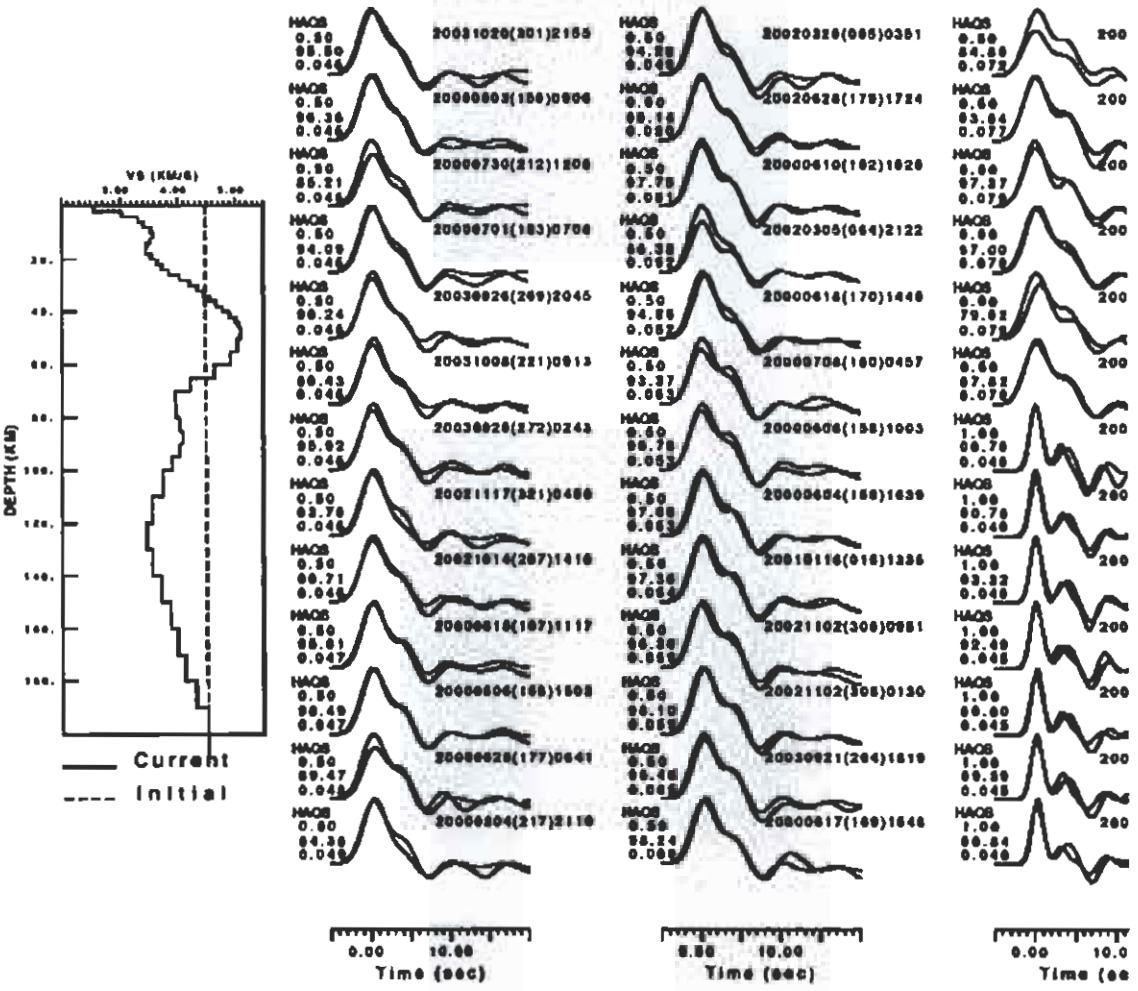

Figure 5.15. Left side is the final earth model inverted from the receiver functions. The right-side plot shows all the receiver function compute to do the inversion. The plot shows the station's name, (HAQS) the Gaussian factors (α = 0.5, 1.0, and 2.5), the final fit between the observed and the predicted receiver function, ray parameters, and the earthquakes used.

TATS

From the stacked receiver function for this station, we identified two layers. The first layer extends to about 14 km deep with an average shear velocity 3.9 km/sec. The second layer extends from 14 to 36 km depth with an average shear velocity of 4.1 km/sec. The crust-mantle transition at this station is sharp (Moho depth is 40 km) with shear velocity of 4.3 km/sec. (Fig. 5.16).

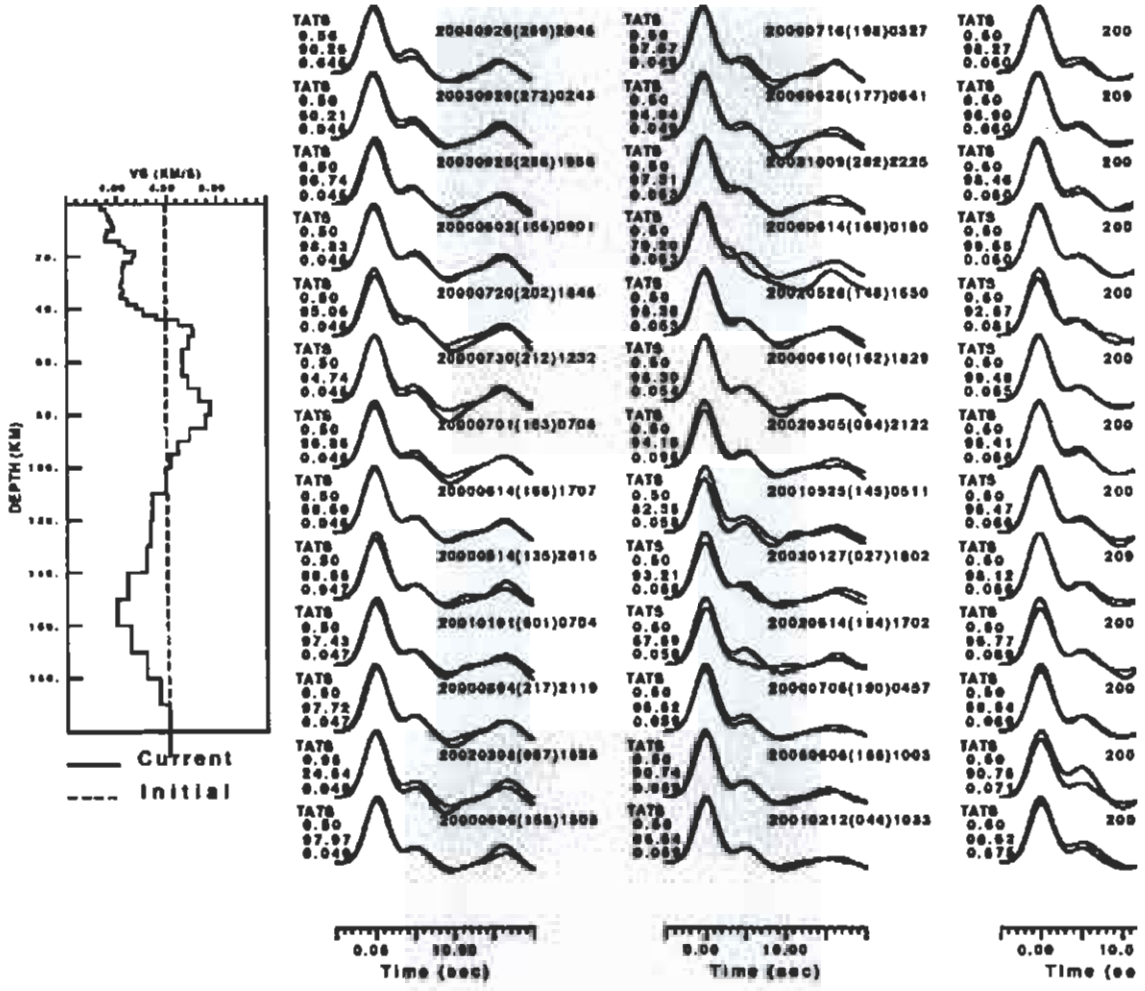

Figure 5.16. Left side is the final earth model inverted from the receiver functions. The right-side plot shows all the receiver function compute to do the inversion. The plot shows the station's name, (TATS) the Gaussian factors (α = 0.5, 1.0, and 2.5), the final fit between the observed and the predicted receiver function, ray parameters, and the earthquakes used.

HASS

Station HASS is characterized by 4-km thick sediments, which is half that determined by *Al-Damegh et al.* (2005). For this station we stack more than 30 receiver function.

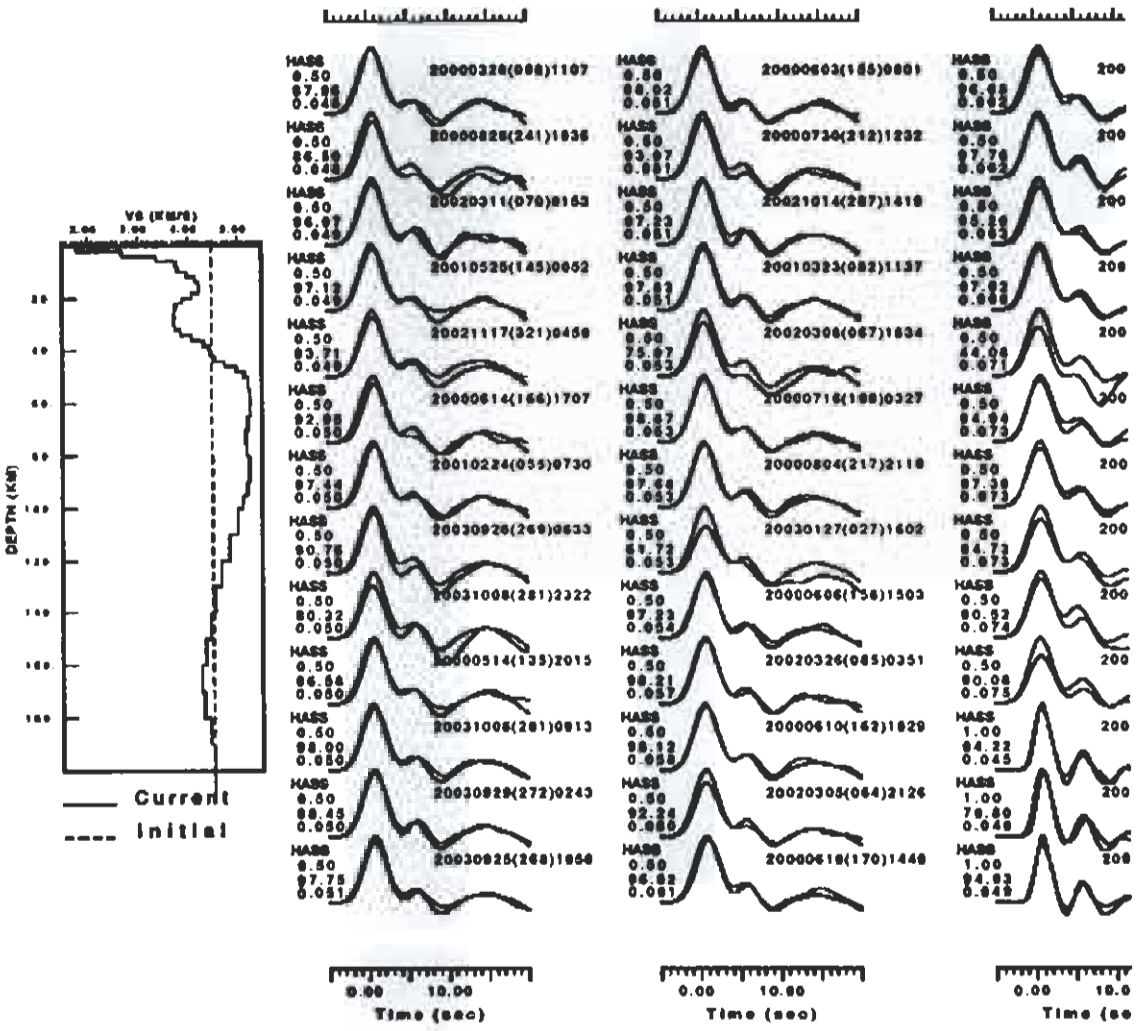

Figure 5.17. Left side is the final earth model inverted from the receiver functions. The right-side plot shows all the receiver function compute to do the inversion. The plot shows the station's name, (HASS) the Gaussian factors (α = 0.5, 1.0, and 2.5), the final fit between the observed and the predicted receiver function, ray parameters, and the earthquakes used.

Since this station is located over a thick sedimentary layer, we can see the effect on the receiver function. The first few kilometers of the upper crust has a very low shear velocity 2 km/sec. The upper crust has a shear velocity of 3.8 and extends between 4 and 30 km depth. The second layer has a crustal thickness of 6 km with an average shear velocity of 4.2 km/sec. The Moho discontinuity can be identify at depth 42 km with an average shear velocity equal to 4.5 km/sec.

The Moho appears to be gradational, but the crustal thickness does not exceed 40 km, which is consistent with v_p/v_s analysis and inconsistent with a grid search analysis for receiver functions fits only, presented in *Al-Damegh et al.* (2005). The mantle velocities are consistent with stable continental values.

Generally speaking, the resulting velocity models beneath the Arabian Peninsula (Fig. 5.18) provide new constraints on crustal and upper mantle structure. This study shows an average crustal thickness of the Arabian shield of 36 km for the stations used in this study. A three layers can be indicated from the final velocity model which is consistent with models reported by *Al-Amri et al.* (2004).

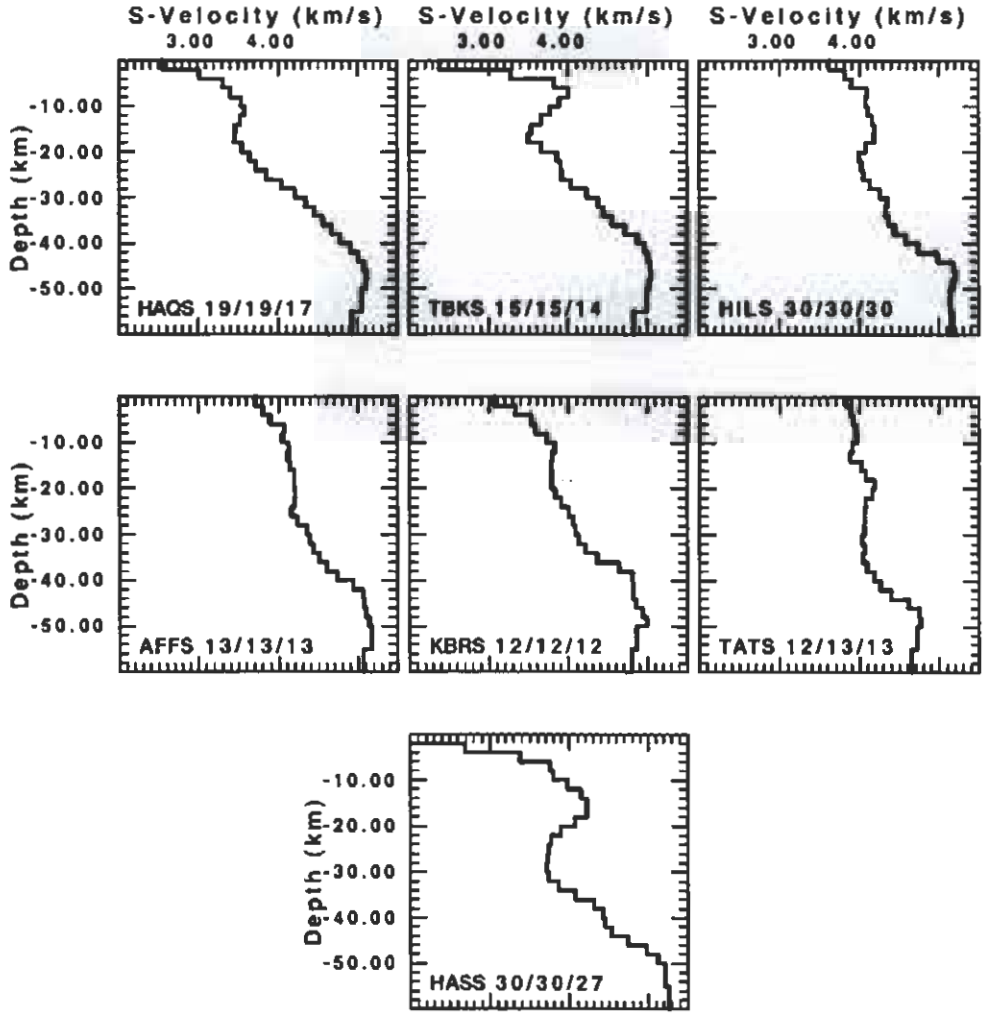

Figure 5.18. The final shear velocity model inverted from receiver function. The model compares stations used on this study. This figure shows the station name with the total receiver function used for the inversion.

5.4 Modeling of surface wave dispersion and teleseismic receiver functions

In this study we applied a new method to simultaneously fit receiver function and surface wave group velocity data (*Tkalcic et al.*,2005). The method involves a combination of grid search, iterative inversions and forward modeling to simultaneously explain the surface wave dispersion (from 7 to 100 seconds for Rayleigh and 20 to 70 seconds for Love waves) and teleseismic RF observations at the broadband stations in the Arabian Peninsula. For the grid search we used a database of pre-calculated theoretical receiver functions and dispersion curves, which allowed us to significantly reduce the computing time and investigate wide range of structural models. We initially fit receiver functions and shorter periods of the observed dispersion curves with the structure within the crust and immediately beneath the crust. We then used an additional grid search to characterize the lithospheric lid and low velocity zone in the upper mantle, fixing the crustal structure and fitting longer period dispersion curves. The method proved to be robust and could be applied in the cases where a little a priori knowledge exists about the crustal structure. Additionally, as a result of the "step by step" approach to recover the structure starting from the "top" and ending with the "bottom" of the model, the multi-step method revealed how mantle velocity variations and transverse isotropy is needed to simultaneously fit all available data.

We apply this technique to a number of stations that sample the complexity of tectonic environments and provide new constraints on structure. Figures 5.19, 5.20, 5.21 and 5.22 illustrate the final fit to the data and our best models for stations ARSS, BLJS, NAMS, YNBS, AFFS, HASS, HILS, HITJC1, KBRS and MEZE. In the following we discuss the features of these models.

Station **ARSS** (Figure 5.19) is located in the eastern edge of the Arabian shield. Our final model has a 40 km thick crust and a relatively pronounced Moho, with a thin lithospheric lid extending 10 km below Moho. No transverse isotropy is needed to explain simultaneously the RFs and surface wave

dispersion data. It appears that the lithospheric lid thickens significantly and that the slight transverse isotropy does not exist at ARSS.

The velocity structure for station **BLJS** (Figure 5.20) is characterized by shallow low velocities, normal crustal velocities and a Moho depth of 38 km. The mantle is characterized by a thin lid and decreasing velocities and up to 5% anisotropy ($v_{SV} > v_{SH}$). These results are consistent with the nearby station, NAMS.

We observe a strong contrast in the velocity at Moho for station **NAMS (Figure 5.21)**. The crustal thickness of 41 km is in agreement with estimate of *Al-Damegh et al.* (2005). Mid-crustal structure is characterized by a transition from slow to fast shear wave speeds (exceeding 4 km/s) and a sudden drop of velocities at about 23 km depth by 0.6 km/s. The lithospheric lid of about 20 km thickness, overlaying a broad low-velocity zone that extends to about 140 km depth, is a well-pronounced feature in the upper mantle.

Station **YBNS** (Figure 5.22) lies in the northern part of the Red Sea coast. YNBS is a station with considerably thinner crust (28 km) compared with other stations modeled in this report, but is consistent with the results of *Al-Damegh et al.* (2005). The mantle velocity is low (4.2 km /s on average), and no lithospheric lid could be observed in the final model (although a strong v_{SH} lid is required). The sign of anisotropy is thus opposite from the sign modeled for stations BLJS and NAMS in the southern part of the Red Sea.

Station **AFFS** (Figure 5.23) is located on the shield, and we do not observe sediments. The crustal thickness is about 35 km, with a fairly pronounced Moho. A layer of transverse isotropy in the zone just below Moho is required to improve fits for Love wave dispersion at intermediate periods. We present a model in which a narrow zone of transverse isotropy (about 20 km) is characterized by a strong value ($v_{SH}>v_{SV}$ about 6%) below Moho and gradually decreasing with depth. The model contains a thin lithospheric lid and low shear wave velocity in the mantle below it (Vs=4.2km/s).

Station **HASS** (Figure 5.24) is characterized by 4-km thick sediments, which is half that determined by *Al-Damegh et al.* (2005). While estimates of sedimentary cover in the eastern Arabian Platform exceed 4 km, explain the difference by our additional constraints from surfaee wave group velocities. This would be consistent with higher velocity sedimentary cover in the deeper parts of the section. The Moho appears to be gradational, but the crustal thickness does not exceed 40 km, which is consistent with v_p/v_s analysis and inconsistent with a grid search analysis for receiver functions fits only, presented in *Al-Damegh et al.* (2005). Again, we believe that surface wave dispersion data provide critical additional constraints when estimating lithospheric structure. Our model for station HASS contains a thick high-velocity lithospheric lid (down to about 120 km) and a low velocity zone beneath it. A strong transverse isotropy (with $v_{SH}>v_{SV}$ up to 8%) extending from Moho to about 120 km depth is required in order to explain jointly receiver functions and Rayleigh and Love wave group velocities. The mantle velocities are consistent with stable continental values.

Station **HILS** (Figure 5.25) is the best example of RF and SWGV data that do not require a complex lithospheric structure to be explained jointly. The data from this station were also analyzed as the best data used in the study of *Al-Damegh et al.* (2005). We obtain a very similar crustal thickness as in that study, and a relatively good fit for a grid search inversion with only 3 layers in the crust and one layer below the crust. There are some improvements in the overall fits by introducing a larger number of much thinner layers in the crust, however these improvements are not so significant as for other stations. The velocity contrast at the Moho is fairly large and it appears that the lithospheric lid and low velocity zone are not strongly pronounced features in the lithospheric mantle under HILS. The Moho depth is at about 36-38 kilometers, which is comparable with the previous study of receiver functions of *Al-Damegh et al.*(2005).

Station **HITJC1** (Figure 5.26) is adjacent to the Gulf of Aqabah and Dead Sea Rift. Our velocity model for this station features a few thin low-velocity layers near the surface, The crustal velocities

are consistent with a slightly lower than average continental values and a Moho depth of about 35 km, consistent with the model obtained by *Rodgers et al.* (2005). The mantle is characterized by an anisotropic lid ($v_{SH} > v_{SV}$) approximately 55 km thick underlain by a LVZ.

Station **KBRS** (Figure 5.27) is an example of a station which has a simple crustal but a complex lithospheric structure. The observed group velocity data cannot be fit jointly with an isotropic model. A gradational Moho between 35 and 38 km is found in our best model. The data for this station had to be modeled by introducing a thin lithospheric lid and a low velocity zone in the upper mantle in order to match low group velocities at intermediate periods (40 to 70 s). A strong transverse isotropy (with $v_{SH}>v_{SV}$ slightly above 10%) is required in the upper mantle below Moho down to about 70 km in order to fit longer periods of Love wave group velocity dispersion. Some anisotropy ($v_{SH}>v_{SV} \sim 3\%$) in the lowermost crust is also required in order to explain high velocities at shorter periods of Love wave group velocity dispersion. We do not have a very good depth resolution of transverse isotropy distribution, and the radial profiles of transverse isotropy (with gradual increase, flat value and decrease) are somewhat arbitrary. Sensitivity kernels of surface waves have quite broad depth variation and we limit our modeling efforts only to introducing simple anisotropy function of depth.

Station **MEZE** (Figure 5.28) is characterized by a small number of useful receiver function data. This is partially due to the fact that it operated for only about 10 months with various instrumentation problems. Our averaged receiver function is thus based only on 5 receiver functions that were sufficiently consistent to be stacked and averaged. We present only a simple grid search result here. We obtain slightly lower crustal thickness than in HASS (about 38±2 km), with overall crustal velocities lower than in HILS and very comparable to HASS models. We cannot expect to entirely infer sediment thickness from only step 1, however the shape of surface wave dispersion

curves is very similar to HASS. It does not appear that any transverse isotropy in the mantle is needed to explain jointly Love and Rayleigh wave group velocities.

We would suggest that low velocity beneath the Gulf of Aqabah and southern Arabian Shield and Red Sea at depths below 200 km are related to mantle upwelling and seafloor spreading. Low velocities beneath the northern Arabian Shield below 200 km may be related to volcanism. The low velocity feature near the eastern edge of the Arabian Shield and western edge of the Arabian Platform could be related to mantle flow effects near the interface of lithosphere of different thickness.

The resulting velocity models beneath the Arabian Peninsula provide new constraints on crustal and upper mantle structure. This study shows an average crustal thickness of the Arabian shield of 36 km for the stations used in this study. A three layers can be indicated from the final velocity model which is consistent with models reported by *Al-Amri et al.* (2004).

Generally speaking, the results for crustal structure are consistent with previous studies where applicable. New results for the lithosphere suggest that the mantle lithosphere is thin and the LVZ is significant near the Red Sea, where rifting is active. The mantle lid thickens away from the Red Sea in the Arabian interior. Furthermore our results indicate the presence of polarization anisotropy in the lithospheric upper mantle, in the vicinity, as well as farther away from the Red Sea. Our modeling suggests $v_{SV} > v_{SH}$ in the southern part of the Red Sea, consistent with vertical flow, and $v_{SH} > v_{SV}$ in the northern part of the Red Sea and the continental interior, as is commonly reported in the continents.

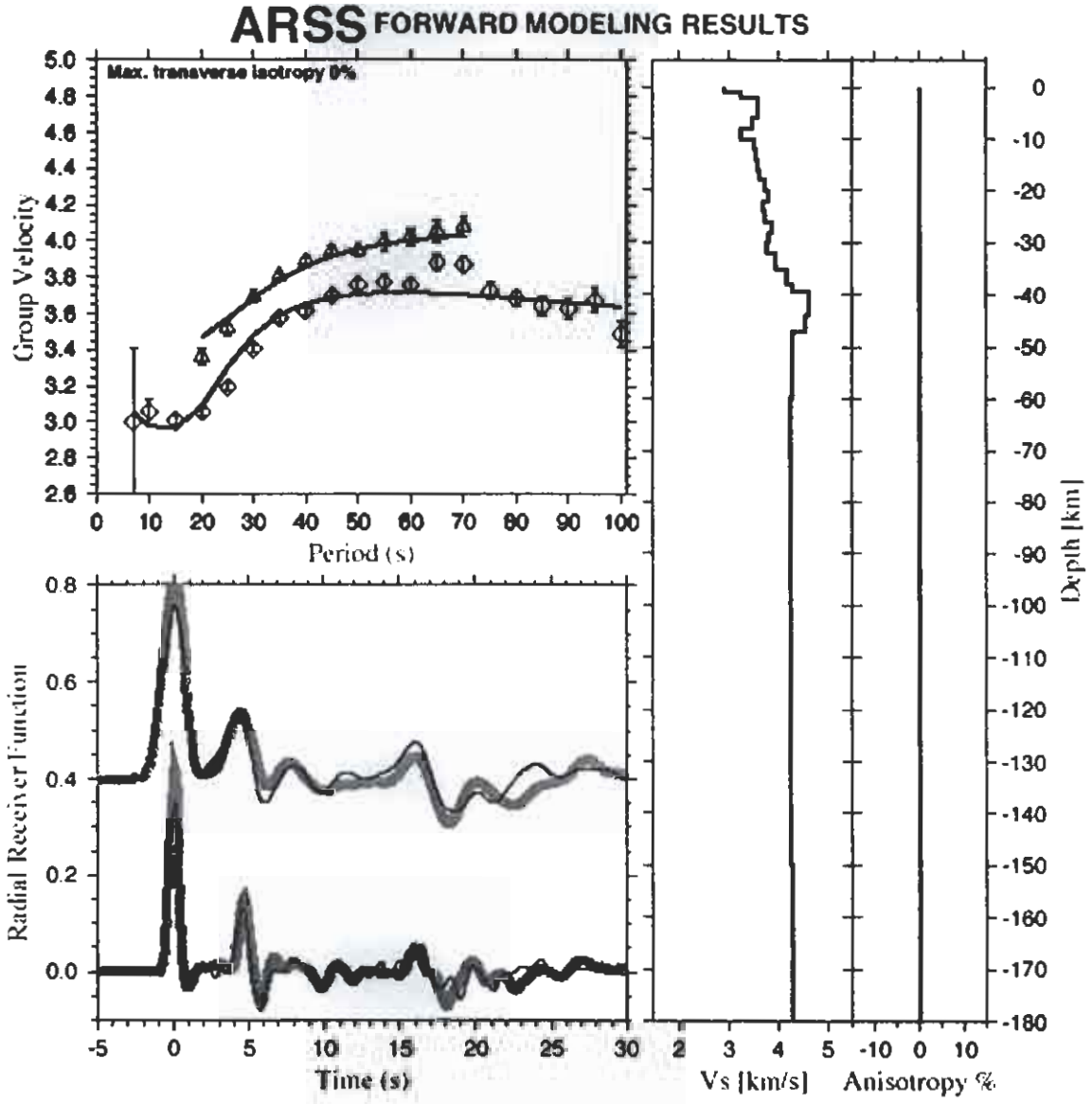

Figure 5.19. Forward modeling of velocity and anisotropy structure in the upper mantle from Love and Rayleigh wave group dispersion for ARSS station. The model shows the final fit to the data and no transverse isotropy is needed to simultaneously fit all available data.

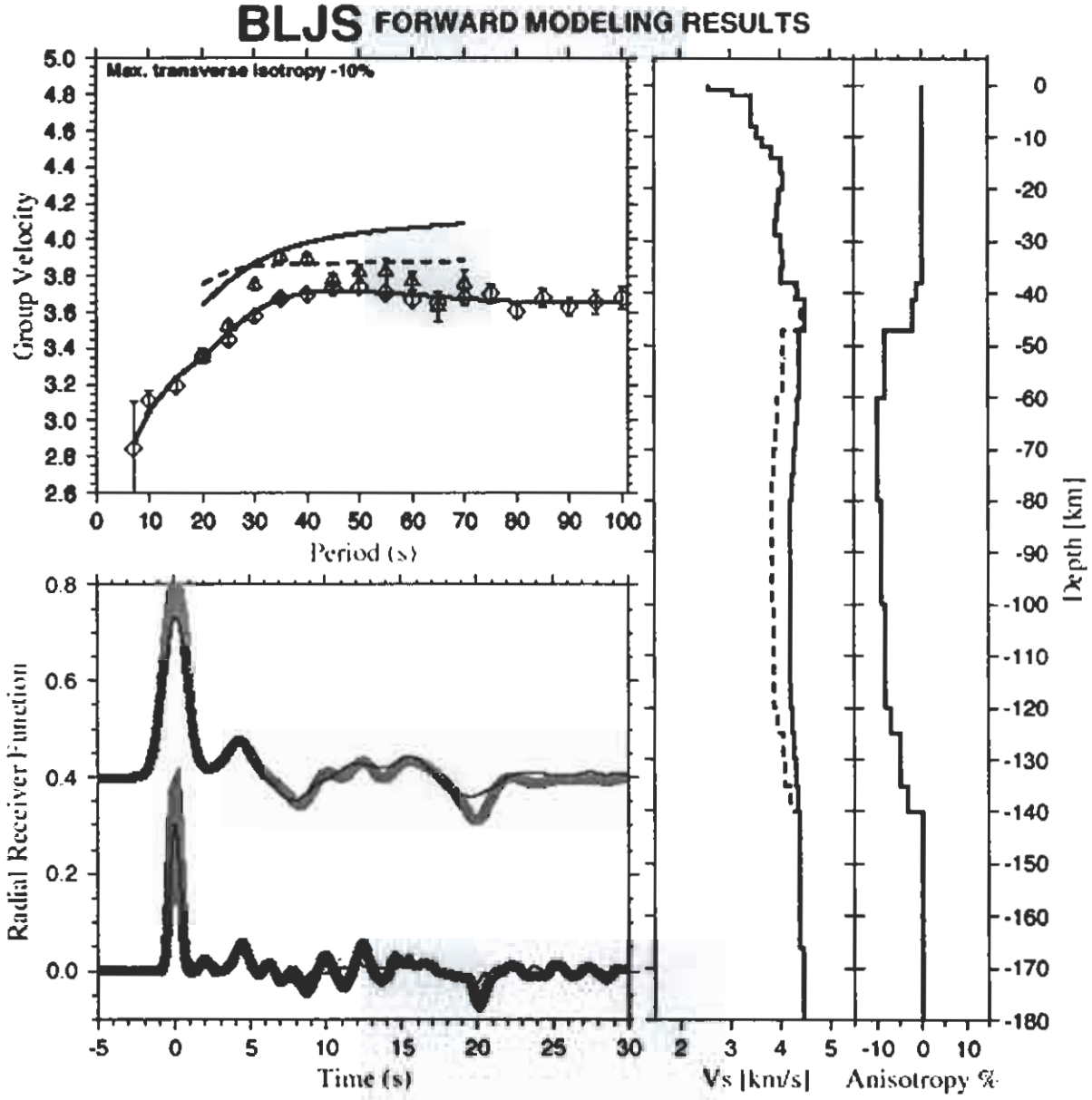

Figure 5.20. Forward modeling of velocity and anisotropy structure in the upper mantle from Love and Rayleigh wave group dispersion for BLJS station. The model shows the final fit to the data and up to 5% anisotropy (Vsv> Vsh).

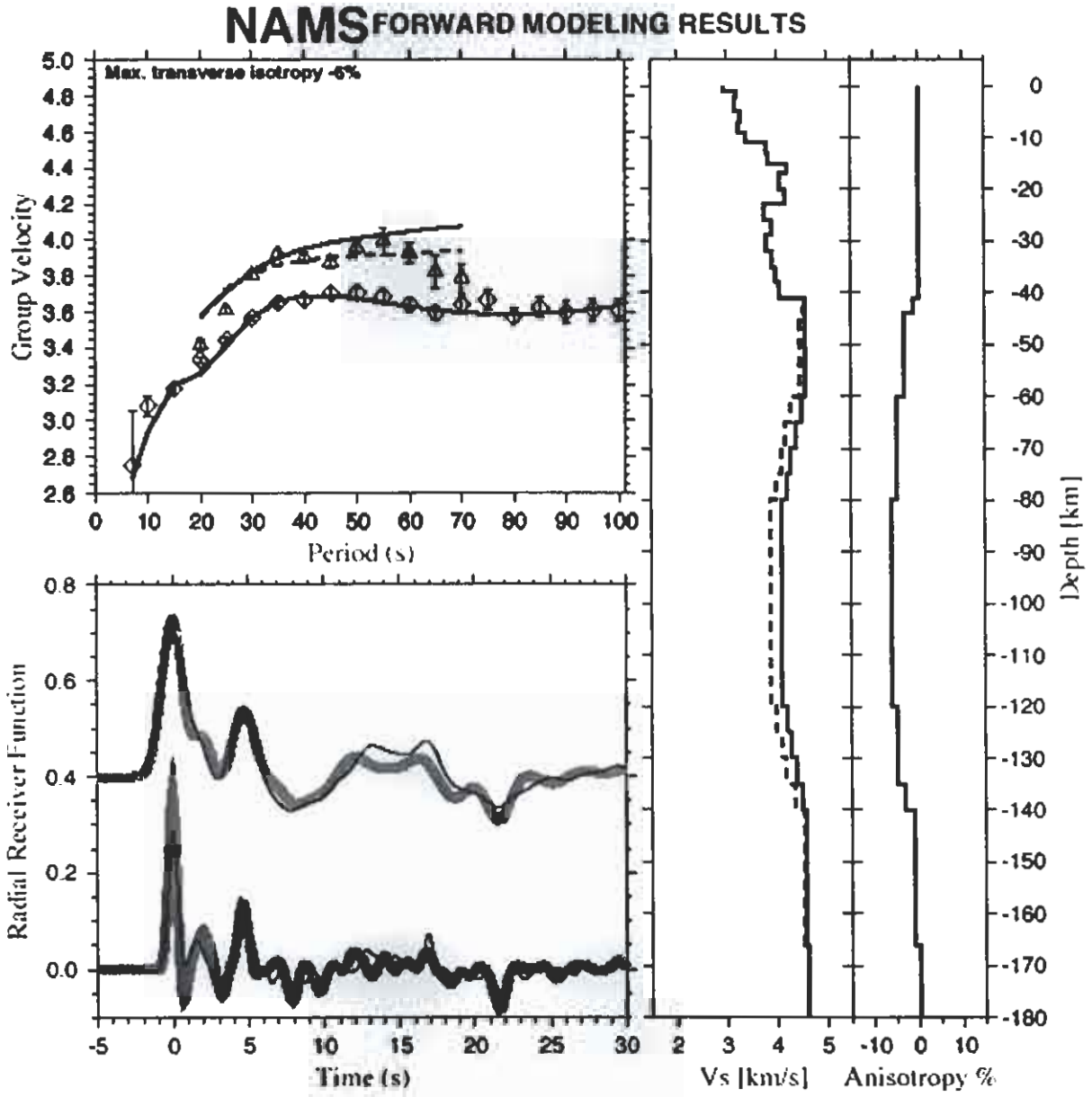

Figure 5.21. Forward modeling of velocity and anisotropy structure in the upper mantle from Love and Rayleigh wave group dispersion for NAMS station. The model shows the final fit to the data. A broad transverse isotropy coinciding with the low velocity zone in the mantle is required with Vsv exceeding Vsh by 6%.

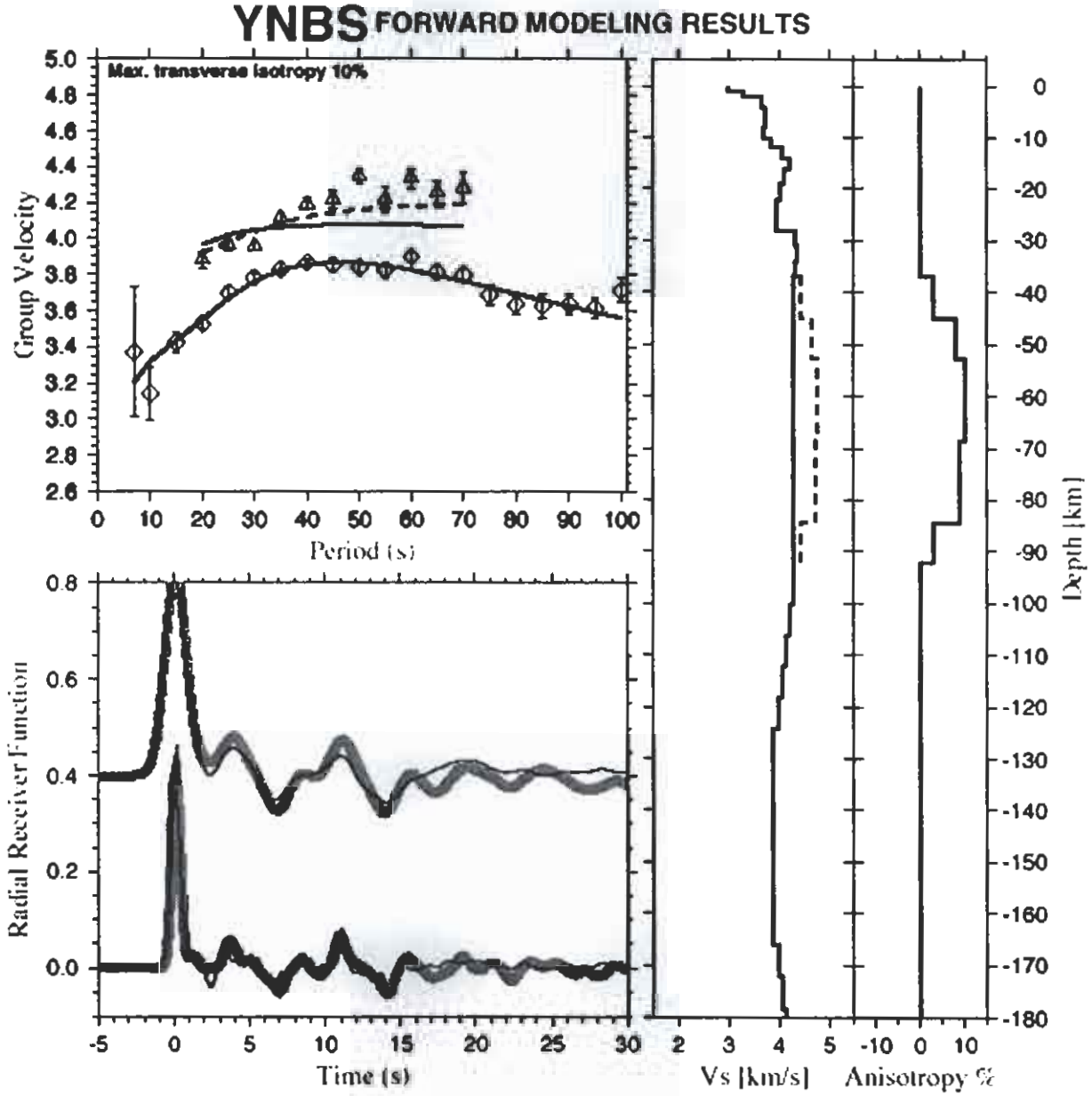

Figure 5.22. Forward modeling of velocity and anisotropy structure in the upper mantle from Love and Rayleigh wave group dispersion for YNBS station. The model shows the final fit to the data. A strong transverse isotropy is found (8% of Vsh > Vsv).

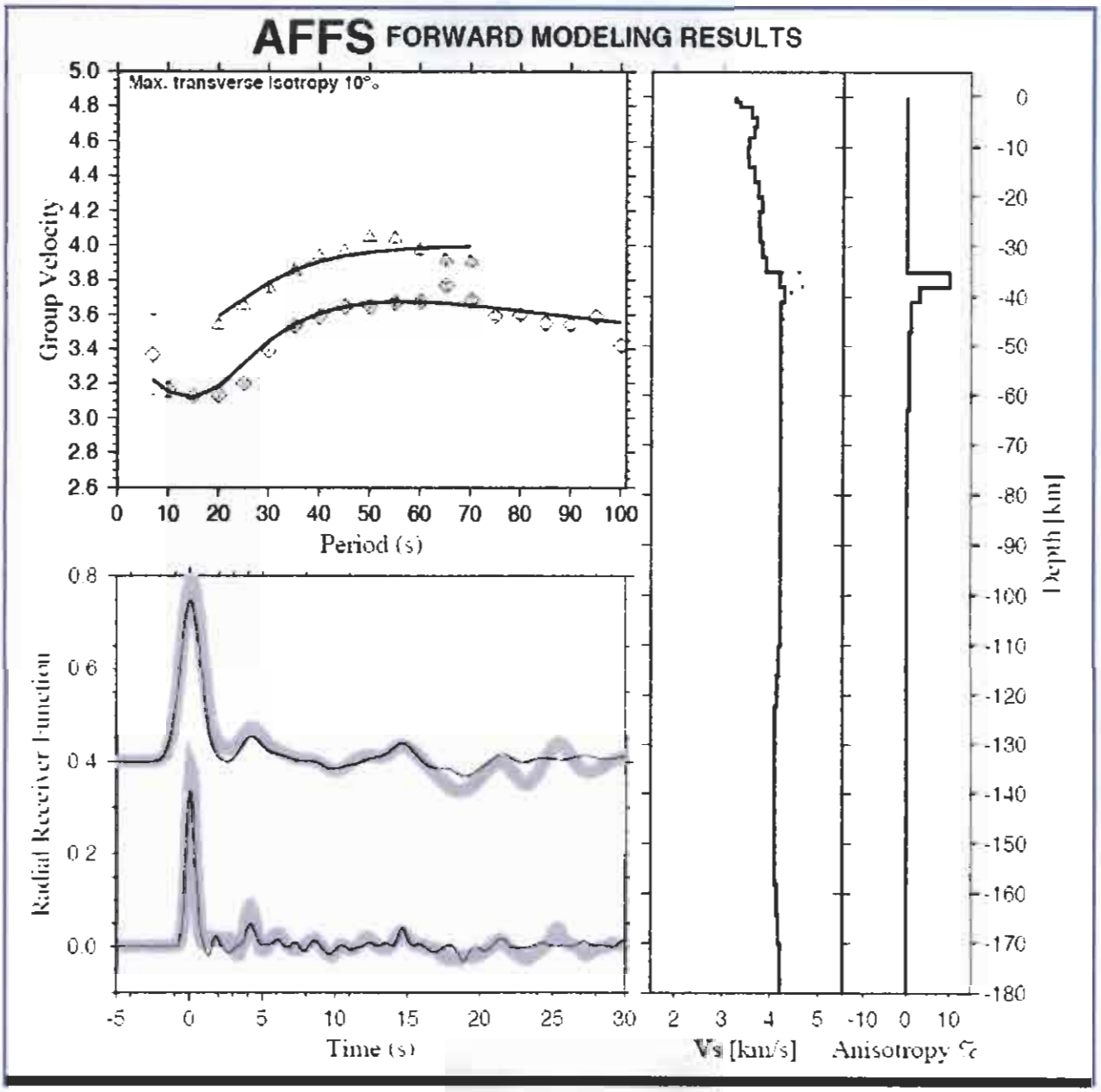

Figure 5.23. Forward modeling of velocity and anisotropy structure in the upper mantle from Love and Rayleigh wave group dispersion for AFFS station. The model shows the final fit to the data.

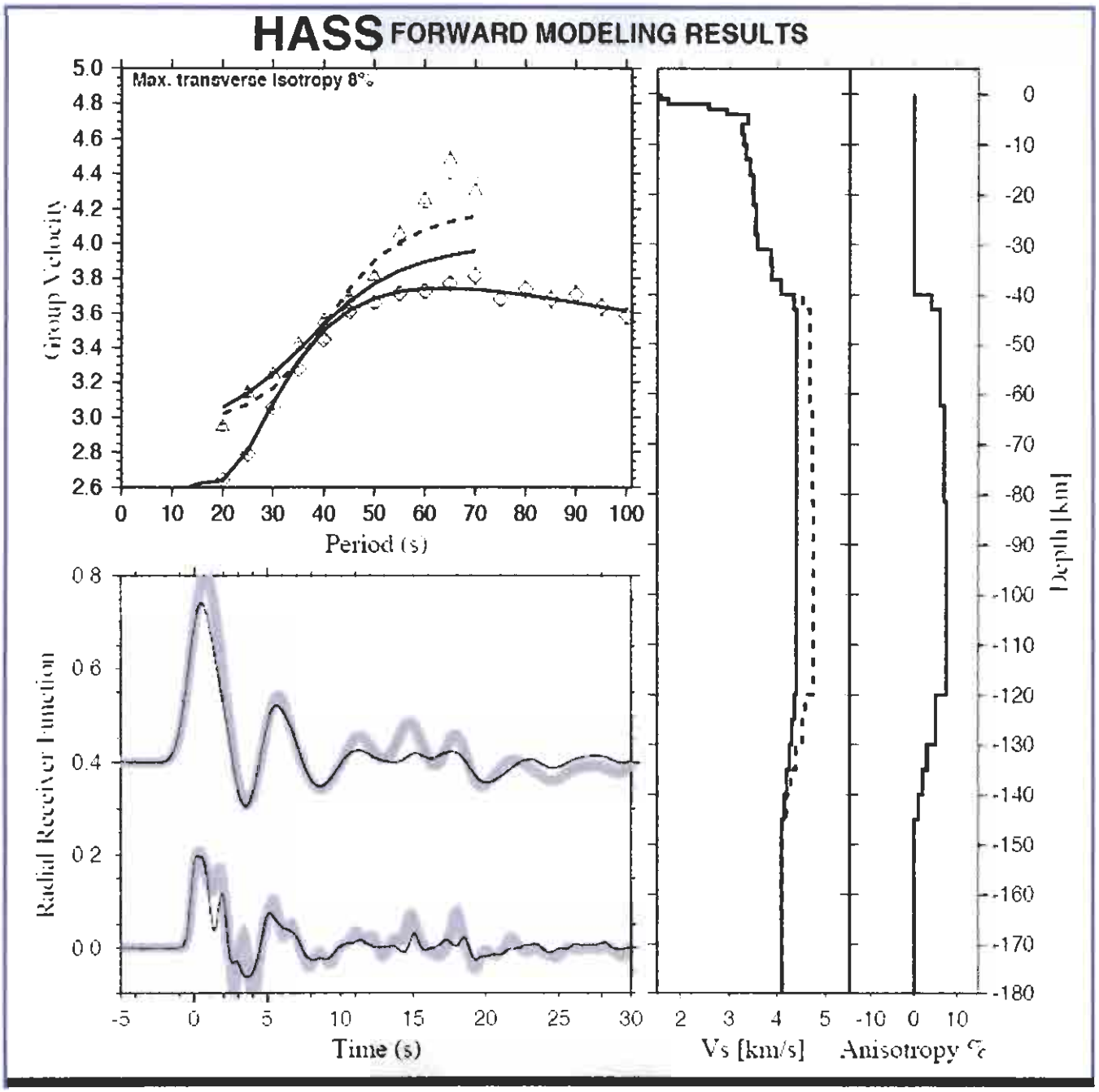

Figure 5.24. Forward modeling of velocity and anisotropy structure in the upper mantle from Love and Rayleigh wave group dispersion for HASS station. The model shows the final fit to the data.

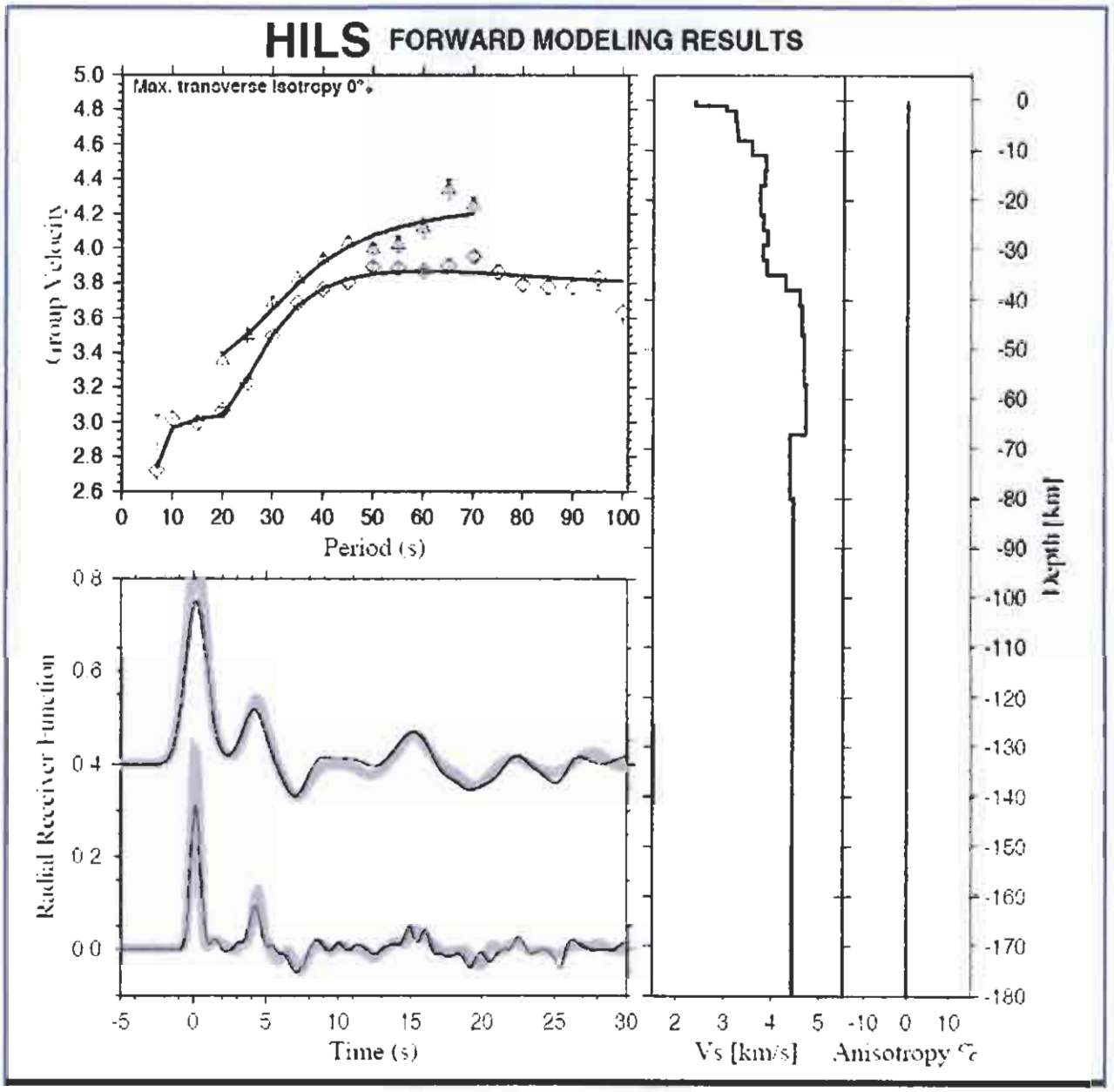

Figure 5.25. Forward modeling of velocity and anisotropy structure in the upper mantle from Love and Rayleigh wave group dispersion for HILS station. The model shows the final fit to the data

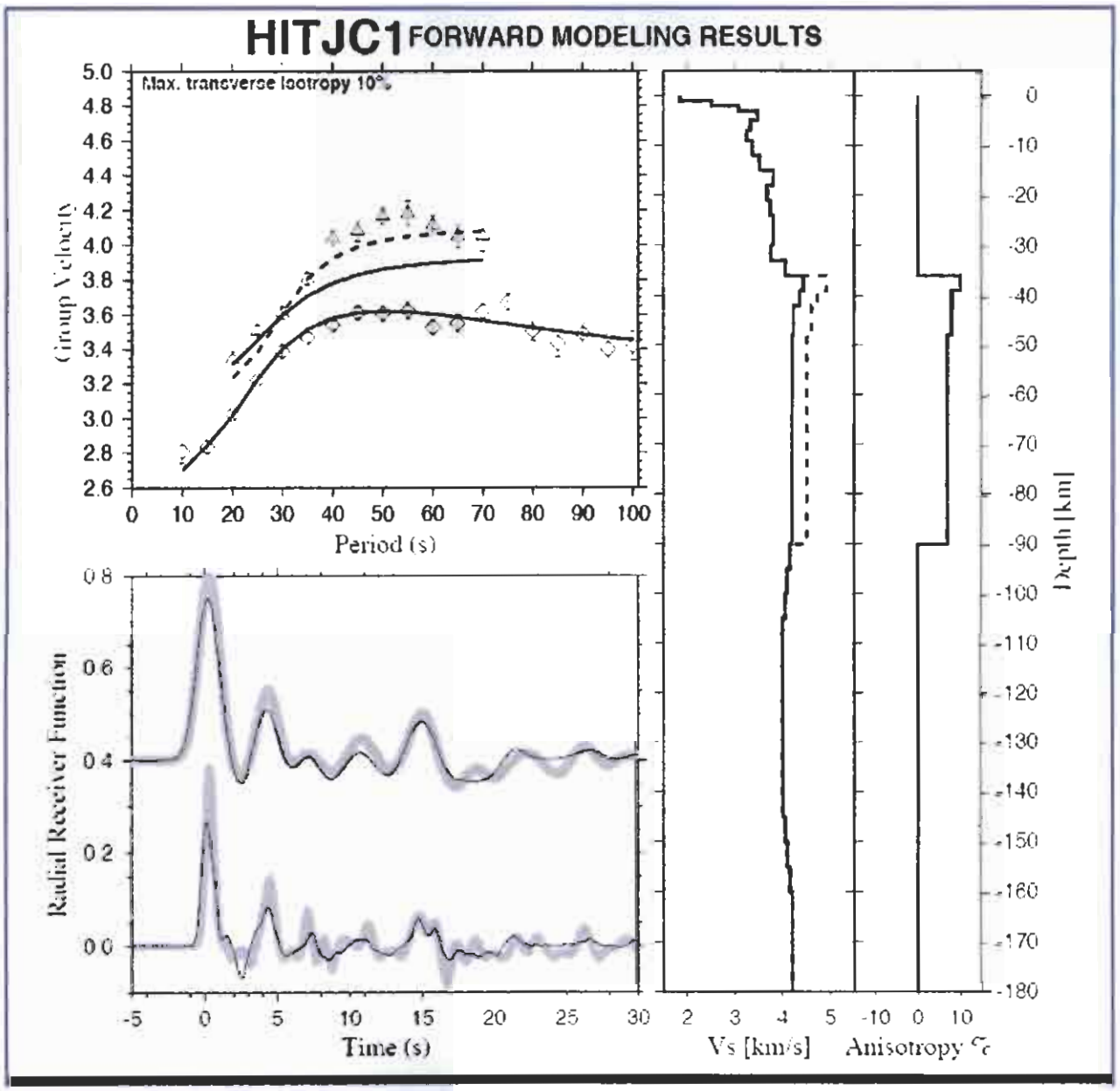

Figure 5.26. Forward modeling of velocity and anisotropy structure in the upper mantle from Love and Rayleigh wave group dispersion for HITJC1 station. The model shows the final fit to the data.

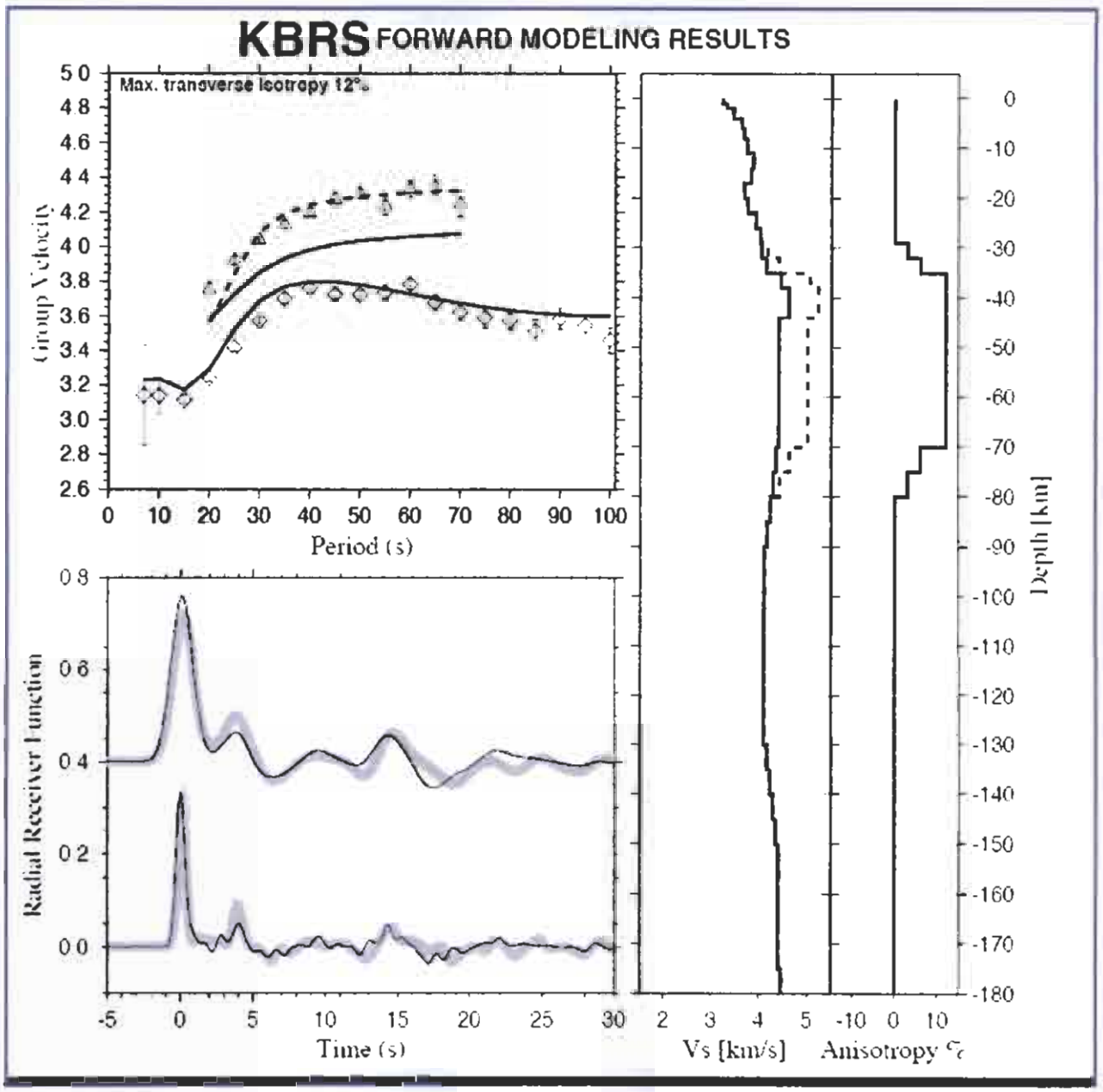

Figure 5.27. Forward modeling of velocity and anisotropy structure in the upper mantle from Love and Rayleigh wave group dispersion for KBRS station. The model shows the final fit to the data

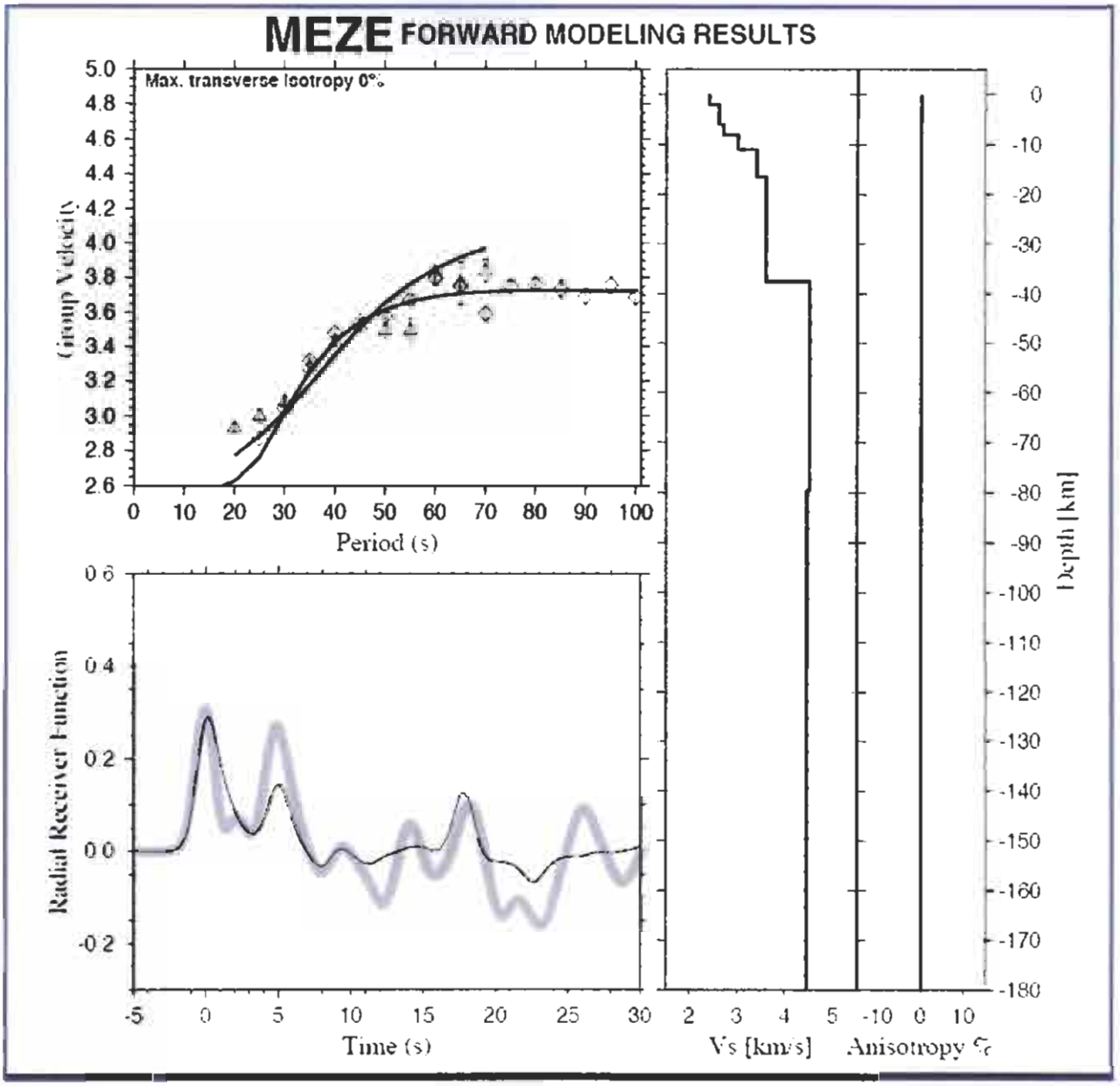

Figure 5.28. Forward modeling of velocity and anisotropy structure in the upper mantle from Love and Rayleigh wave group dispersion for MEZE station. The model shows the final fit to the data.

5.5 Mantle Anisotropy from Shear-Wave Splitting

Seismic anisotropy in the earth causes wave motions in different directions to travel at different speeds. For shear-waves this can lead to bi-refringence, where different polarizations travel at different speeds. Furthermore, anisotropy can cause motions with one polarization to couple into other polarizations. The SKS phase is widely used to study anisotropy because it emerges from the outer core as purely a radially polarized wave. Splitting of the SKS phase occurs when the radially polarized shear wave encounters a zone of anisotropy. One then observes SKS energy on the transverse component of motion, unexpected in an isotropic earth model. The two waves arrive at the station with a relative time shift proportional to the amount of anisotropy and the thickness of the anisotropic layer. The SKS data are processed to estimate the direction of the fast-axis of the anisotropic layer and the delay time. Figure 5.29 shows two example events with similar fast axis (-20 degrees, clockwise from north) and delay time.

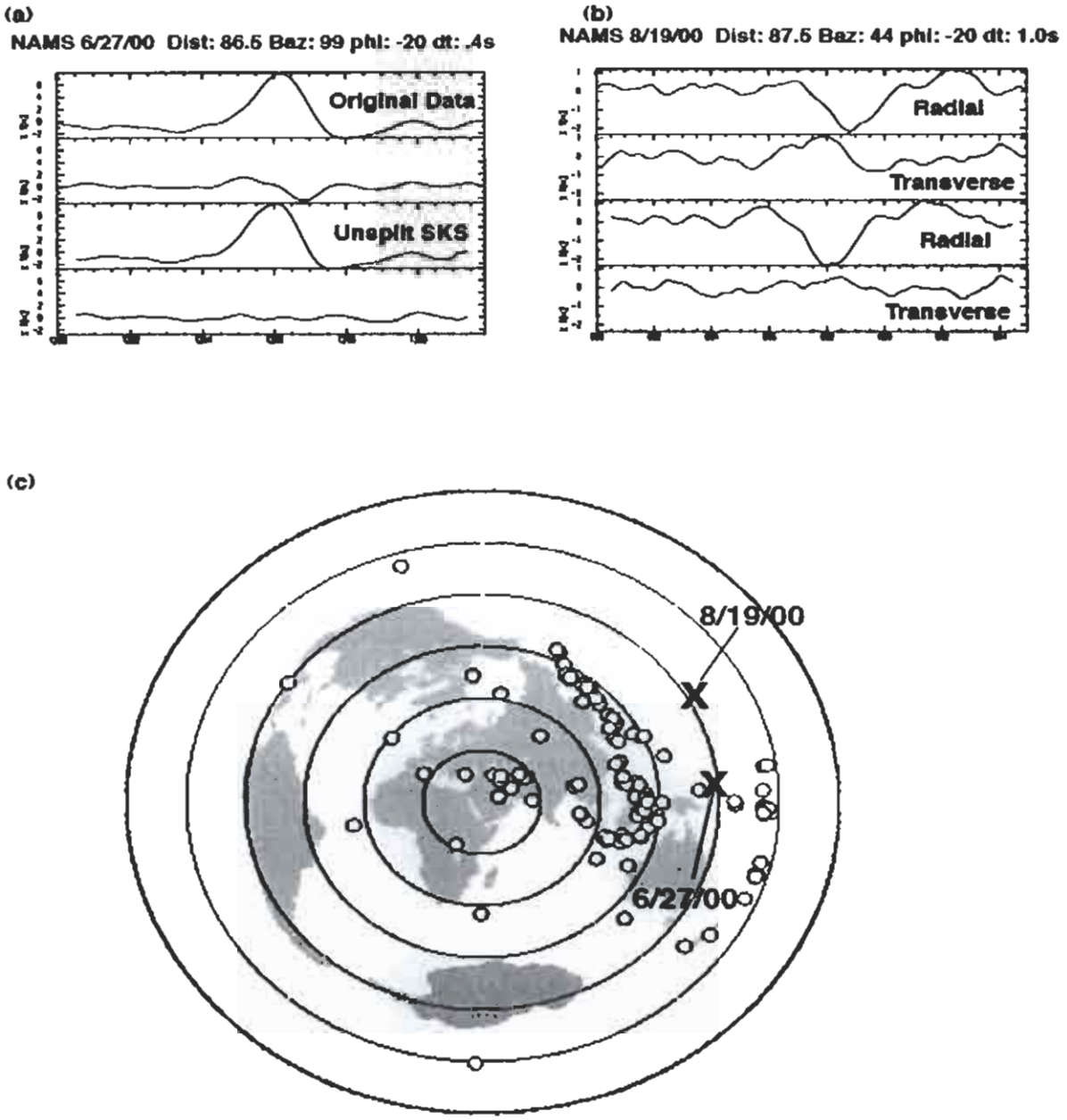

Figure 5.29 Shear-wave splitting examples from SKS data observed at station NAMS. Two events are shown (a) and (b). The event locations are shown in (c).

Hansen et al.(2006) have processed a set of waveforms from several stations in the KACST network. They show clear SKS splitting due to seismic anisotropy.). In total, they used 135 events including 247 records of SKS phases, 12 records of SKKS phases, and 52 records of S phases.

The splitting parameters from different events at each station were averaged to find an overall resultant and these are shown in Figure 5.30. In general, the stations display a north-south oriented φ with an average δt of 1.4 s, similar to the findings of previous studies throughout the area *(Wolfe et al.,* 1999*; Levin and Park*, 2000; *Schmid et al.,* 2004*; Levin et al.*, 2006.

Hemispherical plots for two KACST stations: Gulf of Aqabah station TAYS and Arabian Shield station NAMS are shown in Figure 5.31. Each line displays the splitting parameters for one event, where the line is oriented in the fast polarization direction (φ) and is scaled to the delay time ((δt). The angles on the perimeter show the back-azimuth at which the arrivals are coming from. One can see that while observations at station TAYS are rotated further east, neither station shows any variation in the splitting parameters with back-azimuth.

The splitting observations at the Gulf of Aqabah stations can be best explained by a one-layer model whose φ is oriented parallel to the Dead Sea Transform. Most of the splitting parameter observations across Saudi Arabia are very consistent. The observed north-south φ is not oriented perpendicular to the Red Sea Rift and therefore does not support a passive rifting model. Also, the orientation of φ is at least 30° different from the reported absolute plate motion direction. It is possible that the anisotropic signature obtained could be the result of fossilized anisotropy in the lithosphere, where φ is aligned parallel to the northerly strike of accreted terranes and sutures dating back to the Proterozoic assembly of the Arabian platform (*Stoeser and Camp*, 1985; *Stern*, 1994).

Results of *Hansen et al.* (2006) indicate a fairly consistent fast polarization direction of N20-25°W with delay times ranging between 0.75-1.2 s. This direction is similar but about 20° more westerly

than the north-south fast polarization direction reported by *Wolfe et al.* (1999) from a temporary network of broadband sensors deployed over a much more spatially limited region of the Arabian Shield. *Hansen et al.*, (2006) results extend and confirm their interpretation of a fairly homogeneous anisotropic fabric throughout the shield. However, *Wolfe et al.* (1999) could not discriminate between different interpretations of their dominantly north-south fast polarization directions. Mechanisms that they considered included fossil anisotropy associated with formation of the Proterozoic Arabian lithosphere and modern mineral alignment caused by asthenospheric flow associated with the present northward motion of the Arabian Shield or with an Ethiopian mantle plume.

Generally, this study feel that the observed splitting parameters are the result of a complex interaction of mantle flow in the asthenosphere. Shear caused by the absolute plate motion, which is directed approximately 40° east of north at about 22 mm/yr (Figure 5.32), may affect the alignment of mantle minerals. However, it has also been suggested that flow radiating from the mantle plume beneath Afar is channelized towards the Red Sea Rift (*Ebinger and Sleep*, 1998), which is oriented approximately 30° west of north. Assuming that the strain caused by the plume flow is comparable to that of the plate motion, we can combine these two flow orientations, similar to the vector approach of *Silver and Holt* (2002). This gives an overall resultant that is oriented with a north-south alignment (Figure 5.32).

Our preferred interpretation of the slightly more westerly, and Red Sea Rift parallel, fast directions we obtained, is the alignment of magma filled cracks that form perpendicular to the least compressive stress direction resulting in rift parallel fast polarization directions. This mechanism has been suggested as the dominant cause of anisotropy beneath other rift zones.

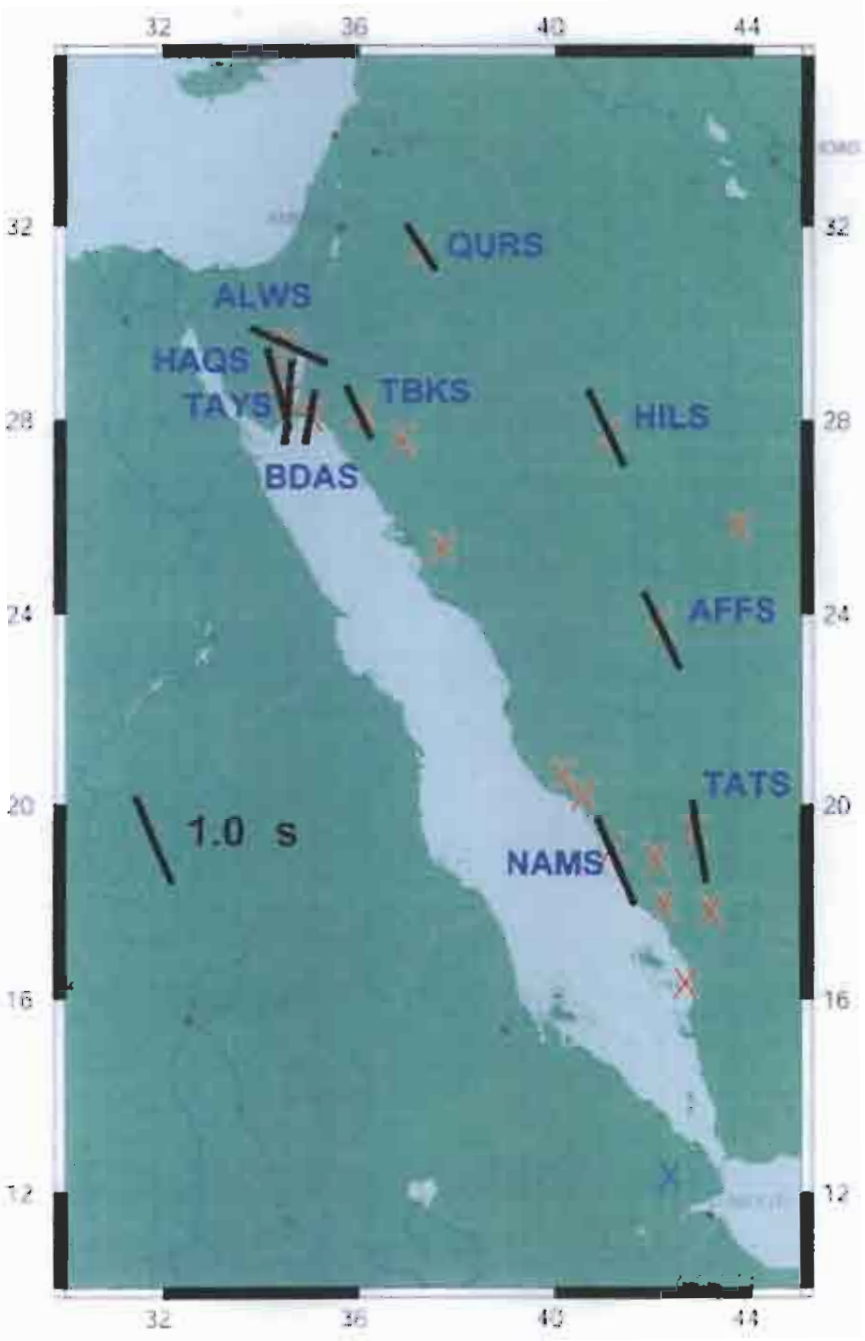

Figure 5.30. SKS splitting parameters for several KACST stations. Red crosses indicate station locations with too few SKS splitting parameters to determine a meaningful average. The direction of the black bar indicates the average direction of fast polarization and its length is scaled by the delay time between the fast and slow waves. Most stations east of the Red Sea Rift show consistent northwesterly fast directions with some complications arising in the vicinity of the Dead Sea.

Mantle flow parallel to extension along the rift, such as in the passive rifting model, would also display a similar orientation to the plate motion. However, since the north-south orientation is also observed far from the rift axis, we favor the absolute plate motion as the contributing vector.

Seismic tomography models have shown that the upper mantle beneath the western portion of the Arabian Shield is anomalously slow, with velocities increasing towards the continental interior (*Debayle et al.*, 2001*; Benoit et al.*, 2003). These observations are attributed to thermal differences beneath Saudi Arabia and indicate much hotter mantle beneath the Red Sea than beneath the interior of the shield, which is consistent with plume flow directed beneath the rift. Surface wave and receiver function analysis shows that there is a change from vertical flow in southwest Saudi Arabia to horizontal flow further north, also consistent with the presence of channelized flow from the mantle plume (*Tkalčić et al.*, 2005*). Daradich et al.* (2003) demonstrated that the higher elevations along the Red Sea Rift and the overall tilt of the Arabian plate result from viscous stresses associated with large-scale mantle flow from the Afar plume. In addition, *Schilling et al.* (1992) found isotopic evidence for mantle mixing between depleted asthenosphere and plume flow in Saudi Arabia, supporting the idea that an interaction of flow is occurring at depth. This combination of both plate and density driven flow can explain the observed anisotropic signature and is consistent with an active rifting model.

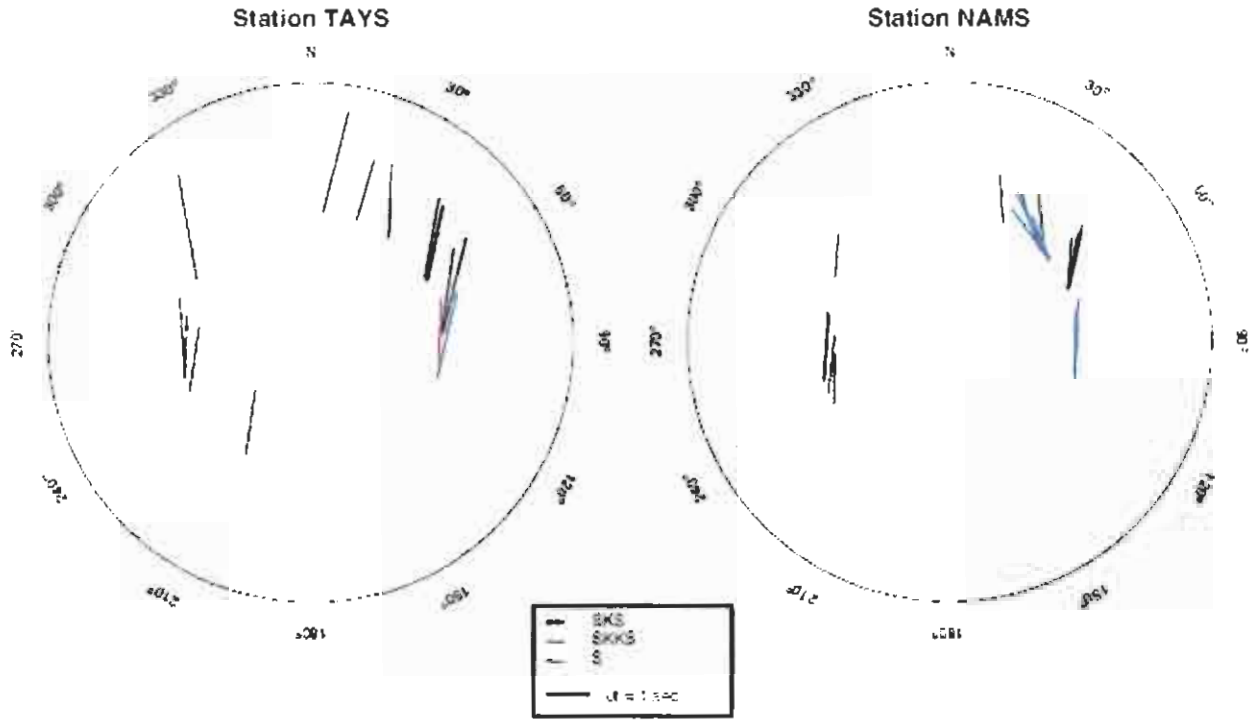

Figure 5.31 . Hemispherical plots for two KACST stations: Gulf of Aqabah station TAYS and Arabian Shield station NAMS. Each line displays the splitting parameters for one event, where the line is oriented in the fast polarization direction (φ) and is scaled to the delay time (δt). Black lines correspond to SKS phases, red lines correspond to SKKS phases, and blue lines correspond to S phases.

Table 5.1. Average splitting parameters. This table lists the latitude and longitude of each station as well as the average splitting parameter values and their corresponding standard deviations. These values were plotted in Figure 5.30 *(Hansen et al. (2006).*

Station Name	Latitude	Longitude	Avg. Fast Angle	Fast Angle St. Dev	Avg. Delay Time	Delay Time St. Dev.
AFFS	23.927	43.001	-6.80	14.02	1.466	0.44
AFIF	23.931	43.040	-13.00	10.28	1.378	0.30
ALWS	29.310	35.065	2.89	9.01	1.522	0.40
ARSS	25.881	43.237	8.33	13.88	1.124	0.33
AYUS	28.189	35.269	2.75	15.16	1.518	0.46
BDAS	28.432	35.101	1.91	10.02	1.702	0.34
BLJS	19.881	41.599	-3.20	22.25	1.010	0.31
DJNS	17.707	43.543	-9.43	8.77	1.514	0.71
HALM	22.845	44.320	-1.38	14.54	0.966	0.33
HAQS	29.055	34.930	10.57	11.57	1.608	0.38
HASS	25.190	49.694	-8.00	15.64	1.266	0.46
HILS	27.384	41.792	-17.00	11.76	1.162	0.31
HIT	32.475	38.402	6.50	10.84	1.512	0.49
JMOS	29.169	35.109	3.07	7.12	1.606	0.37
KBRS	25.789	39.262	-3.43	14.96	1.358	0.38
LTHS	20.275	40.411	-8.86	15.32	1.228	0.33
NAMS	19.171	42.208	-3.12	14.34	1.346	0.23
QURS	31.386	37.324	-6.00	13.65	1.314	0.52
RANI	21.312	42.780	6.73	13.51	1.664	0.40
RAYN	23.522	45.500	6.26	12.98	1.164	0.36
RIYD	24.722	46.640	4.00	32.76	1.414	0.67
RUW	29.743	35.841	0.67	9.23	1.300	0.05
SODA	18.292	42.380	-7.14	10.43	1.510	0.29
TAIF	21.281	40.350	8.67	9.35	1.208	0.20
TATS	19.541	43.478	-2.67	10.20	1.538	0.44
TAYS	28.551	34.872	7.47	7.19	1.856	0.31
TBKS	28.225	36.549	-13.25	15.15	1.212	0.45
UQSK	25.789	42.360	-2.00	10.58	1.456	0.34
YNBS	24.340	37.992	-4.29	12.88	1.464	0.13

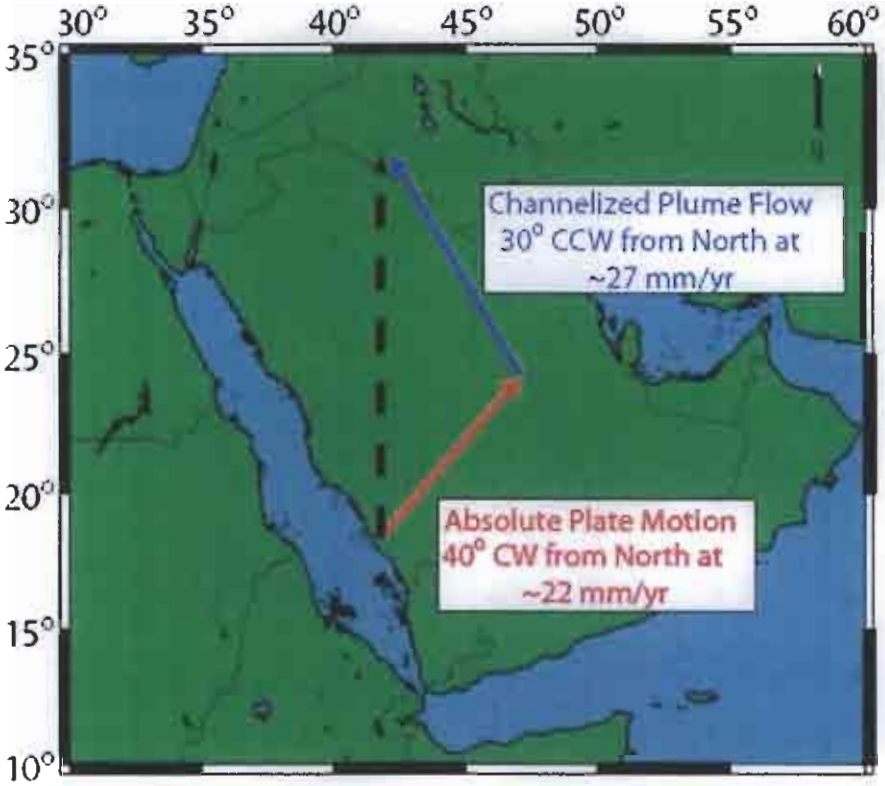

Figure 5.32. Vector examination of plate motion (red arrow) coupled with channelized upwelling flow (blue arrow) beneath Saudi Arabia. If we estimate that absolute plate motion is oriented N40E at a rate of 22 mm/yr and that channelized hotspot flow is oriented approximately N30W, then the rate of hotspot flow needed to obtain a north-south resultant (black dashed arrow) is ~27 mm/yr.

VI. DISCUSSION & CONCLUSIONS

Teleseismic data recorded on broadband instruments from four different seismic arrays were used in this study. The largest array, KACST seismic network, includes 27 broadband stations distributed along the eastern edge of the Red Sea and across the Arabian Peninsula. KACST data from events occurring since 2000 were used. To supplement the KACST coverage, we also analyzed data recorded by the eight IRIS-PASSCAL Saudi Arabian Broadband Array stations, which operated from November 1995 to March 1997, data from two stations deployed in Jordan, which operated between 1998 and 2001, and data recorded by two stations in the UAE from 2003 and 2004

S-waves with high signal-to-noise ratios were selected from earthquakes with magnitudes larger than 5.7 in a distance range of 60° to 85°. Waveforms were first rotated from the N-E-Z to the R-T-Z coordinate system using the event's back-azimuth and were visually inspected to pick the S-wave onset. The three-component records were then cut to focus on the section of the waveform that is 100 s prior to the S-wave onset and 20 s after. To more clearly detect Sp conversions, the cut R-T-Z data must be further rotated around the incidence angle into the SH-SV-P coordinate system and deconvolved. This second rotation is critical because if an incorrect incidence angle is used, noise can be significantly enhanced and major converted phases may become undetectable. A subroutine was developed, based on the approach of Sodoudi (2005), which rotates the cut R-T-Z seismograms through a series of incidence angles, from 0° to 90° in 3° increments, to create a set of quasi-SV and quasi-P data. Each quasi-SV component is then deconvolved from the corresponding quasi-P component using Ligorria and Ammon's iterative time domain method, which creates a SRF. To make the SRFs directly comparable to PRFs, both the time axes and the amplitudes of the

SRFs must be reversed. Using this approach, 31 different SRFs, corresponding to the 31 different incidence angles examined, are created for each event at a given station.

To limit our examination to the true P, SV components and their corresponding receiver function, we found the incidence angle that minimizes the direct S-wave energy on the P-component. On the time-reversed receiver functions, the direct S arrival is at 0 s. Therefore, we are only interested in the receiver function whose mean amplitude is closest to zero at zero time. A second subroutine was developed to examine all the generated receiver functions for a given event and determine which record best meets this criteria. The P, SV components and the corresponding receiver function with the appropriate incidence angle are retained, and the remaining records are discarded.

Once receiver functions were generated for all events at an examined station, a move-out correction was applied to the receiver functions to correct for variations in distance between events. Again, to make the SRFs directly comparable to PRFs, we used a reference slowness of 6.4 s/deg. Each individual receiver function is then visually inspected and compared to previously determined PRFs at the same station to identify the Moho phase. Only SRFs that display a clear Moho conversion at the appropriate time are used for further analysis. These records were then stacked to obtain a better signal-to-noise ratio for the weaker LAB phase (Lithosphere / Asthenosphere Boundary).

It should be noted that a similar approach to that outlined above was also used to examine SKS arrivals. In this case, we examined earthquakes with magnitudes larger than 5.6 in a distance range from 85° to 120°. However, it was discovered that the SKS arrivals do not generate clear Sp conversions given their steeper angles of incidence. Therefore, further examination of SKS receiver functions was not pursued.

Synthetic receiver functions were generated using the reflectivity method to match the amplitude and timing of both the Moho and LAB conversions on the stacked SRFs. Using the programs "icmod" and "respknt", the responses of an incoming S-wave to different three-layer velocity models were generated. These synthetic responses were then processed using the same approach outlined previously to obtain the synthetic SRFs. The amplitude and timing of the phases on the real and synthetic receiver functions were matched by adjusting the crustal, upper mantle, and lower mantle velocities as well as the depth of the Moho and the LAB. While these values varied from station to station, the average crustal and upper mantle S-wave velocities needed to fit the Moho amplitude were about 3.6 and 4.5 km/s, respectively. These are similar to the S-wave velocities used to fit the Moho amplitude on the SANDSN PRFs. To fit the LAB amplitude, an average lower mantle velocity of about 4.2 km/s is required. In all cases, a default Poisson's ratio of 0.25 was used .

It should be noted that the average shear velocities and default Poisson's ratio used to generate the synthetics differ from those found by waveform modeling. Rodgers et al.(1999) reported average crustal S-wave velocities of 3.7 and 3.5 km/s and average upper mantle S velocities of 4.3 and 4.55 km/s for the Arabian Shield and Platform, respectively. In addition, the reported Poisson's ratio in the Arabian Shield mantle was 0.29 while in the Platform it was 0.27. Testing reveled that the waveform modeling velocities did not fit the SRF phase amplitudes as well, but the timing of the phases only changed by a few tenths of a second. Therefore, the difference in shear velocities only leads to a few kilometers difference in depth. However, the timing of the phase conversions is more dependent on the Poisson's ratio. Larger Poisson's ratios, such as those suggested by the waveform modeling, result in earlier arrivals and hence shallower depths. Several tests were performed to examine how much the Moho and LAB depths changed when using the

Shield and Platform Poisson's ratio values. Based on the amount of variation observed, the reported Moho and LAB depths are accurate to within 5 and 10 km, respectively.

Seafloor spreading in the Red Sea is non-uniform, ranging from nearly 0 cm/yr in the north to about 2 cm/yr in the south. Given the configuration of stations, we focused our examination along profile AA', which extends from the southern Red Sea Rift axis inland to station HASS. This allowed us to examine the most extensively rifted portion of the lithosphere as well as the structure beneath both the Arabian Shield and Platform. However, for comparison, we also examined the more northern profile BB', which extends from the northern rift axis across the Arabian Shield to station ARSS. Similar to profile AA', the Moho and LAB along BB' are shallowest near the Red Sea and become deeper towards the Arabian interior . Near the coast, the Moho is at a depth of about 22-25 km. Crustal thickening continues until an average Moho depth of about 35-40 km is reach beneath the interior Arabian Shield. The LAB near the coast is at a depth of about 55 km; however it also deepens beneath the Shield to attain a maximum depth of 100-110 km. These boundary depths are comparable to those at similar distances along profile AA' (Hansen et al., 2007).

The lithospheric structure along profile BB' was also tested by comparing its predicted gravity signature to data collected by the GRACE satellites. The same density values for the Arabian Shield used in the examination of profile AA' were employed. In addition, since profile BB' has fewer stations and therefore fewer constraints, we set the lithospheric thickness beneath the rift axis to be similar to that on profile AA' and examined if the calculated gravity signature is consistent with the recorded data. Small-scale recorded gravity observations can be matched very well by slightly adjusting the Moho and LAB boundaries (within the estimated error). Broad-scale gravity observations are also well fit by a shallow asthenosphere beneath the Red Sea. These results demonstrate that while seafloor spreading is not as developed in the northern Red Sea, the lithosphere has still been thinned and eroded by rifting processes (Hansen et al., 2007).

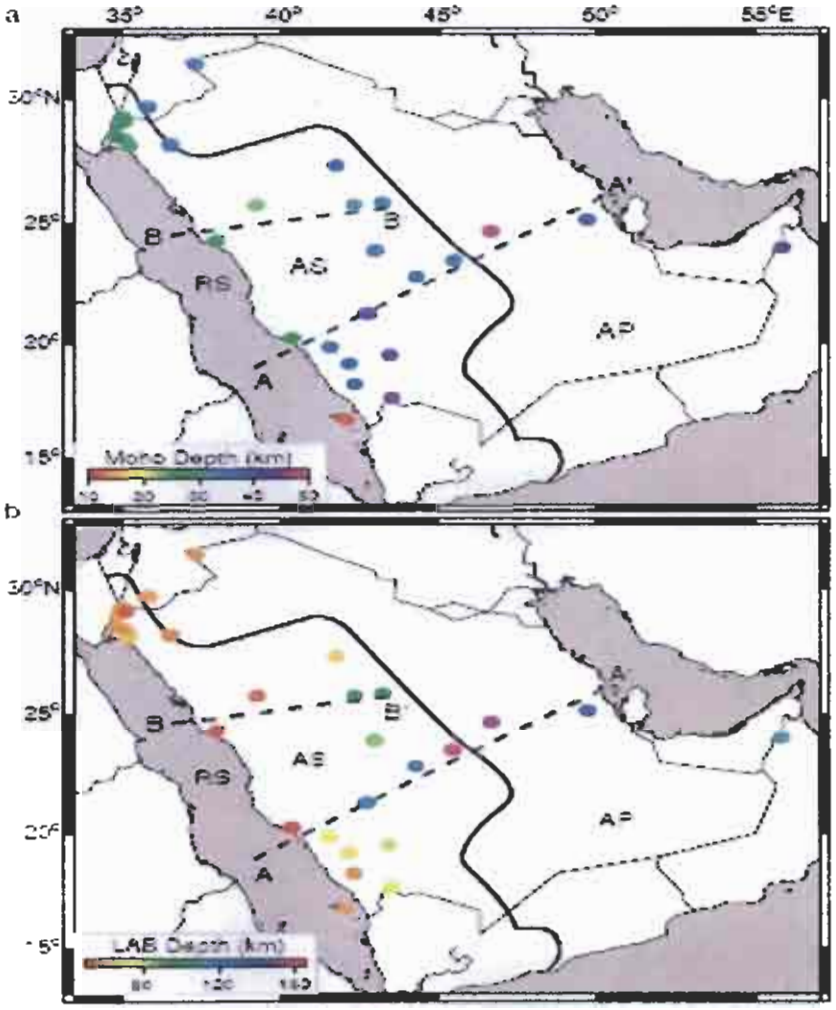

Figure 5.33. Maps showing the boundary depths beneath Arabia. The colored circles show the **a)** Moho and **b)** LAB depths beneath individual stations where warmer colors indicate shallower depths than cooler colors. The solid line marks the boundary between the Arabian Shield (AS) and the Arabian Platform (AP) while the two dashed lines mark the locations of cross-sectional profiles AA' and BB'. Shallow (40-60 km) LAB along Red Sea coast and Gulf of Aqabah Thickens (80-120 km) toward interior of Shield Step (20-40 km) across the Shield-Platform boundary (Hansen et al., 2007).

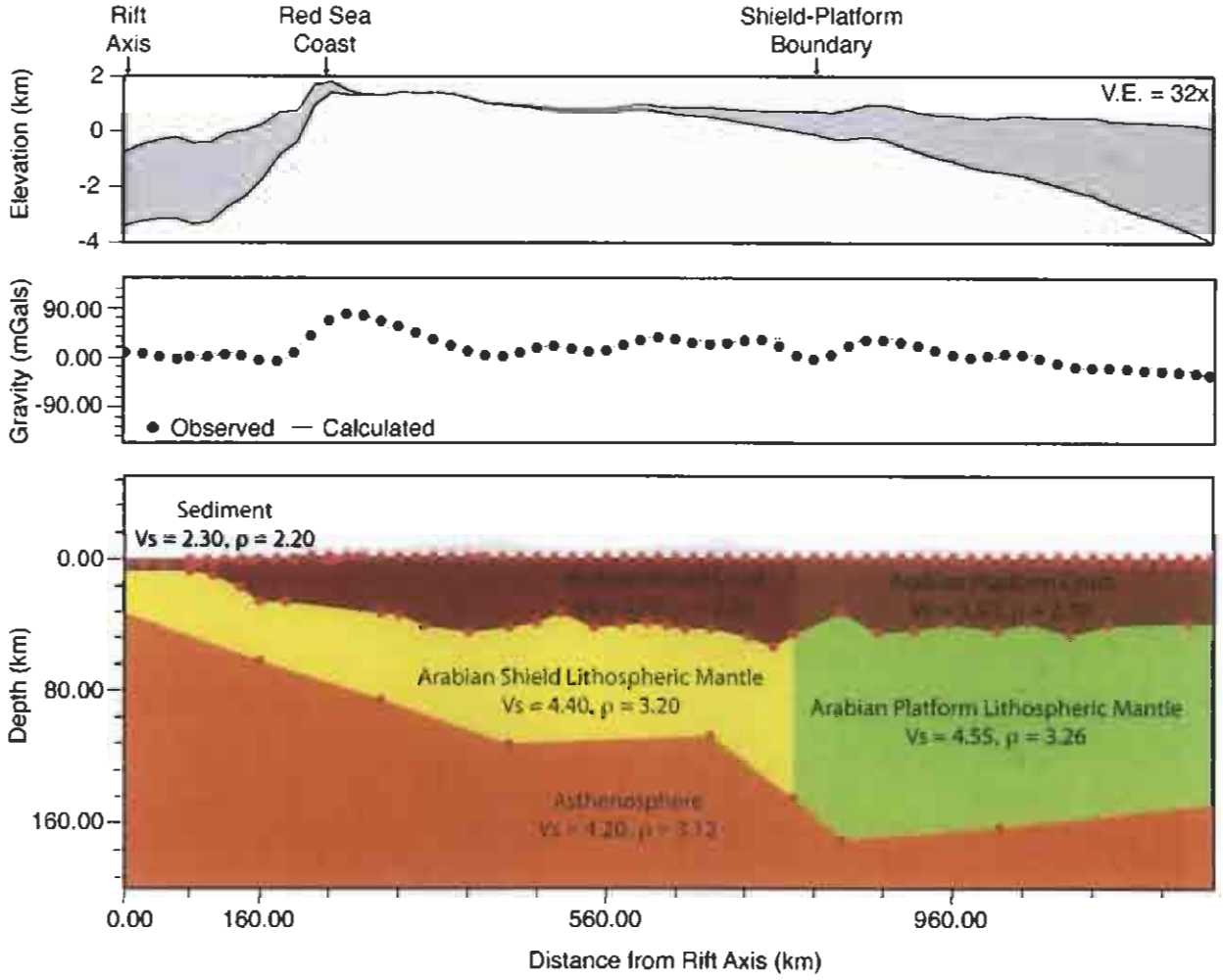

Figure 5.34. Topography, gravity signature, and lithospheric structure along cross-sectional profile AA' from Figure 5. **a** Topography along the profile plotted with a 32x vertical exaggeration (V.E.). The sediment thickness is shown by the grey shaded areas. **b** Comparison of the observed gravity data from the GRACE satellites (black dots) and the calculated gravity (grey line) resulting from the structural model shown in **c**. The S-wave velocities (Vs) in km/s and densities (ρ) in g/cm^3 of each layer are listed (Hansen et al.,2007).

Recent Crustal Structures

Al-Amri et al. (2004) performed the grid search using travel time data sets: (a) Pn and Pg; and (b) Pn, Pg and Sg. In order to select a single velocity model to be representative of the paths sampled, they made use of the results of a seismic refraction (*Ginzburg et al.*, 1979 ; El-Isa, 1990 and *Seber et al.*, 1997. Their grid search results with the thicker crusts (28-30 km) are consistent with these earlier studies. The preferred model has a crustal thickness of 28 km for the Gulf of Aqabah

Table 6.1 Velocity Model for the Gulf of Aqabah/Dead Sea Region

DEPTH (KM)	THICKNESS(KM)	V_P (KM/S)	V_S (KM/S)
0	2	4.50	2.60
2	5	5.50	3.18
7	10	6.10	3.52
17	11	6.20	3.60
28	∞	7.80	4.37

V_P and V_S are the P- and S-wave velocities, respectively.

Earlier work with waveform data from the 1995-1997 Saudi Arabian Broadband Deployment by the University of California, San Diego (UCSD) and King Saud University resulted in models for the Arabian Platform and Arabian Shield *(Rodgers et al.*, 1999). In that studied Love and Rayleigh wave group velocities were modeled to estimate average one-dimensional seismic velocity models of the two main geologic/tectonic provinces of Saudi Arabia. A grid search was used to quickly find a range of models that satisfactorily fit the dispersion data, then that range of models was explored to fit the three-component broadband (10-100 seconds) waveforms. The resulting models revealed significant differences between the lithospheric structure of the two regions.

Table 6.2 Velocity Model for the Arabian Shield Region

DEPTH (KM)	THICKNESS(KM)	V_P (KM/S)	V_S (KM/S)
0	1	4.0	2.31
1	15	6.20	3.58
16	20	6.80	3.93
36	∞	7.90	4.30

Table 6.3 Velocity Model for the Arabian Platform Region

DEPTH (KM)	THICKNESS(KM)	V_P (KM/S)	V_S (KM/S)
0	4	4.00	2.31
4	16	6.20	3.64
20	20	6.4	3.70
40	∞	8.10	4.55

To check the validity of the Arabian Platform, we measured Rayleigh and Love wave group velocities for a number of regional events from the Zagros Mountains and Turkish-Iranian Plateau. Paths from these events to the SANDSN stations sample the Arabian Platform.

Generally, we would suggest that low velocity beneath the Gulf of Aqabah and southern Arabian Shield and Red Sea at depths below 200 km are related to mantle upwelling and seafloor spreading. Low velocities beneath the northern Arabian Shield below 200 km may be related to volcanism. The low velocity feature near the eastern edge of the Arabian Shield and western edge of the Arabian Platform could be related to mantle flow effects near the interface of lithosphere of different thickness.

The results for crustal structure are consistent with previous studies where applicable. New results for the lithosphere suggest that the mantle lithosphere is thin and the LVZ is significant near the Red Sea, where rifting is active. The mantle lid thickens away from the Red Sea in the Arabian interior. Furthermore our results indicate the presence of polarization anisotropy in the lithospheric upper mantle, in the vicinity, as well as farther away from the Red Sea. Our modeling suggests $v_{SV} > v_{SH}$ in the southern part of the Red Sea, consistent with vertical flow, and $v_{SH} > v_{SV}$ in the northern part of the Red Sea and the continental interior, as is commonly reported in the continents. The Moho appears to be gradational, but the crustal thickness does not exceed 40 km, which is consistent with v_p/v_s analysis and inconsistent with a grid search analysis for receiver functions fits only. The mantle velocities are consistent with stable continental values.

Teleseismic shear-wave splitting along the Red Sea and across Saudi Arabia reveals that stations in the Gulf of Aqabah display fast orientations that are aligned parallel to the Dead Sea Transform Fault. However, our observations across Saudi Arabia show a consistent pattern of north-south oriented fast directions with delay times averaging about 1.4 s. While fossilized anisotropy related to the Proterozoic assembly of the Arabian Shield may contribute to our observations, we feel that the anisotropic signature is best explained by a combination of plate and density driven flow in the asthenosphere. Shear caused by the absolute plate motion, which is directed approximately 40° east of north at about 22 mm/yr, may affect the alignment of mantle minerals. Combining the northeast oriented flow associated with absolute plate motion with the northwest oriented flow associated with the mantle plume beneath Afar generates a north-south oriented resultant that matches our splitting observations.

RECOMMENDATIONS FOR FURTHER INVESTIGATIONS

In order to fully understand the detail geophysical, seismological and seismic hazard picture of the Arabian Peninsula, this study recommends an extensive research covering :

A. An expensive but potentially insightful line of research is to carry out a detailed seismic deep refraction and gravity profiles in the Arabian Platform and along the coast of the Gulf of Aqabah to obtain a precise bulk composition of crustal layers and improve velocity model.

B. Upgrading of the existing system at King Saud University from analog to digital broadband recordings is strongly recommended for getting better quality signals.

C. Linking of KACST and KSU seismic networks with the national seismographic network at the Saudi Geological Survey is of great importance for getting better and dense station coverage as well as in facilitating data exchanges.

D. Installation of strong motion accelerographs in various areas of the Arabian Shield to precisely estimate the attenuation characteristics of the region and to improve seismic hazard parameters.

E. Assessment of seismic hazard in seismically active zones by constructing a probabilistic ground-shaking hazard map. This map will provide an estimate of the level of ground shaking at all sites expected from earthquake sources throughout the region (both local and regional). The map integrates the seismicity, attenuation and sit response factors.

F. A comprehensive study of the geotechnical engineering aspects should be done to account for local site effects and soil amplification.

G. A comprehensive study of seismogenic and faulting sources is needed for seismic zonation and microzonation of the Arabian Penninsula.

REFERENCES

Al-Amri, A.M. (1995 b). Preliminary seismic hazard assessment of the southern Red Sea region, *J Europ. earthq. Eng.* 3, 33-38.

Al-Amri, A. M., F. R. Schult, and C. G. Bufe (1991). Seismicity and aeromagnetic features of the Gulf of Aqabah (Elat) region, *J Geophys. Res.* 96, 20179-20185.

Al-Amri, A. M. (1998). The crustal structure of the western Arabian Platform from the spectral analysis of long-period P-wave amplitude ratios, *Tectonophysics,* 290, 271-283.

Al-Amri, A. M. (1999). The crustal and upper-mantle structure of the interior Arabian platform, *Geophys. J. Int.,* 136,421-430.

Al-Amri, A. M., R. Mellors and F. Vernon (1999). Broadband seismic noise charateristics of the Arabian Shield, *The Arabian Journal for Science and Engineering*, 24, 2A, 99-113.

Al-Amri, M. S. and A. M. Al-Amri (1999). Configuration of the Seismographic networks in Saudi Arabia, *Seism. Res. Lett.*, 70, 322-331.

Al-Amri, A. M. (1998). The crustal structure of the western Arabian Platform from the spectral analysis of long-period P-wave amplitude ratios, *Tectonophysics,* 290, 271-283.

Al-Amri, A. M. (1999). The crustal and upper-mantle structure of the interior Arabian platform, *Geophys. J. Int.,* 136,421-430.

Al-Amri, M., and A. Al-Amri (1999). Configuration of the seismographic networks in Saudi Arabia, *Seism. Res. Lett.*, 70, 322-331.

Al-Amri, A., A. Rodgers and T. Alkhalifah, Improving Seismic Hazard Assessment in Saudi Arabia Using Earthquake Location and Magnitude Calibration (2004). *Proceedings of the Third Symposium on Scientific Research and Technological Development Outlook in the Arab World, Riyadh, Saudi Arabia.*

Al-Damegh, K, E. Sandvol and M. Barazangi (2005). Crustal structure of the Arabian plate : New constraints from the analysis of teleseismic receiver functions, *Earth and Planetary Science Letter,* 231, 177-196.

Ammon, C. J., G. E. Randall and G. Zandt (1990). On the non-uniqueness of receiver function inversions, *J. Geophys. Res.*, 95, 15303-15318.

Ammon, C. J.(1991). The isolation of receiver effects from teleseismic P waveforms, *Bull. Seismol. Soc. Am.,* 81, 2504-2510.

Badri, M. (1991). Crustal structure of central Saudi Arabia determined from seismic refraction profiling, *Tectonophysics,* 185, 357-374.

Ben-Menahem, A. (1979). Earthquake catalogue for the Middle East (92 BC - 1980 *AD).Boll. Geofisica Teor. Appl.* 21, 245-310.

Benoit, M., A. Nyblade, J. VanDecar and H. Gurrola (2003). Upper mantle P wave velocity structure and transition zone thickness beneath the Arabian shield, *Geophys. Res. Lett.*,80,*doi:10.1029/2002GL016436.*

Bohannon, R. G., C. W. Naeser, D .L. Schmidt, and R.A. Zimmerman (1989). The timing of uplift, and rifting peripheral to the Red Sea: a case for passive rifting? *J. Geophys. Res.*, 94, 1683-1701.

Bostock, M.G. (1996). Ps conversions from the upper mantle transition zone beneath the Canadian landmass, *J. Geophys. Res.*, 101, 8393-8402.

Camp, V. E., and M. J. Roobol (1992). Upwelling asthenosphere beneath western Arabia and its regional implications, *J. Geophys. Res.*, 97, 15255-15271.

Daradich, A., J. Mitrovica, R. Pysklywec, S.Willett, and A. Forte (2003). Mantle flow, dynamic topography, and rift-flank uplift of Arabia, *Geology*, 31, 901-904.

Debayle, E., J. J. Lévêque, and M. Cara (2001). Seismic evidence for a deeply rooted low-velocity anomaly in the upper mantle beneath the northeastern Afro/Arabian continent, *Earth Plan. Sci. Lett.*, 193, 423-436.

Du, Z. J. and G. R. Foulger (1999). The crustal structure beneath the northwest fjords, Iceland, from receiver functions and surface waves, *Geophys. J. Int.*, 139, 419-432.

Dueker, K.G., and A.F. Sheehan (1997). Mantle discontinuity structure from midpoint stacks of converted P to S waves across the Yellowstone hotspot track, *J. Geophys. Res.*, 102,8313-8327.

Ebinger, C., and N. Sleep (1998). Cenozoic magmatism throughout east Africa resulting from impact of a single plume, *Nature*, 395, 788-791.

Evans, J.R., and U. Achauer (1993). Teleseismic velocity tomography using the ACH-method: theory and application to continental scale studies, in *Seismic Tomography: Theory and Practice*, pp. 319-360, Chapman and Hall, London.

Gao, S., P. Davis, H. Liu, P. Slack, A. Rigor, Y. Zorin, V. Mordvinova, V. Kozhevnikov, and N. Logatchev (1997). SKS splitting beneath continental rift zones,*J. Geophys. Res.*, 102, 22,781-22,797.

Gettings, M., H. Blank, W. Mooney and J. Healey (1986). Crustal structure of southwestern Saudi Arabia, *J. Geophys. Res.*, 91, 6491-6512.

Gurrola, H., J.B. Minster, and T. Owens (1994). The use of velocity spectrum for stacking receiver functions and imaging upper mantle discontinuities, *Geophys. J. Int.*, 117, 427-440.

Gurrola, H., and J.B. Minster (1998). Thickness estimates of the upper mantle transition zone from bootstrapped velocity spectrum stacks of receiver functions, *Geophys. J. Int.*, 133, 31-41.

Hansen, S., S. Schwartz, A. Al-Amri, and A. Rodgers (2006).Combined plate motion and density-driven flow in the asthenosphere beneath Saudi Arabia: Evidence from shear-wave splitting and seismic anisotropy, *Geology*, 34, no.10, 869-872.

Hansen, S., A. Rodgers, S. Schwartz, and A. Al-Amri (2007). Imaging Ruptured Lithosphere Beneath the Red Sea and Arabian Peninsula. Accepted for publication in *Earth and Planetary Science Letter.*

Jackson, J., and T. Fitch (1981). Basement faulting and the focal depths of the larger earthquakes in the Zagros mountains (Iran), *Geophys. J. R. astron. Soc.*, 64, 561-586.

Julia, J., C.J. Ammon, R.B. Herrmann, and A.M. Correig (2000). Joint inversion of receiver function and surface wave dispersion observations, *Geophys. J. Int.*, 143, 99-112.

Karato, S. I. (1998). Seismic anisotropy in the deep mantle, boundary layers and the geometry of mantle convection, *Pure and Appl. Geophys.*, 151, 565-587.

Kennett, B. and E. R. Engdahl (1991). Travel times for global earthquake location and phase identification, *Geophys. J. Int.*, 105, 429-465.

Langston, C.A.(1979). Structure under Mount Rainier, Washington, inferred from teleseismic body waves, *J. Geophys. Res.*, 84, 4749-4762.

Levin, V., and J. Park (2000). Shear zones in the Proterozoic lithosphere of the Arabian Shield and the nature of the Hales discontinuity, *Tectonophysics*, 323, 131-148.

Levin, V., A. Henza, J.Park, and A. Rodgers (2006). Texture of mantle lithosphere along the Dead Sea Rift: recently imposed or inherited?, *Physics of the Earth and Planetary Interiors*, in press.

Li, A., K.M. Fisher, M.E. Wysession, and T.L. Clarke (1998). Mantle discontinuities and temperature under the North American continental keel, *Nature*, 395, 160-163.

Ligorría, J. P. and C. J. Ammon (1990). Iterative deconvolution and receiver function estimation, *Bull. Seismol. Soc. Am.*, 89, 1395-1400.

Mechie, J., C. Prodehl and G. Koptschalitsch (1986). Ray path interpretation of the crustal structure beneath Saudi Arabia, *Tectonophysics*, 131, 333-351.

Mellors, R. J., V. E. Camp, F. L. Vernon, A.M.S. Al-Amri, and A. Gharib (1999). Regional waveform propagation in the Arabian Peninsula, *J. Geophys. Res.*, 104, 20221-20235.

Menke, W., and V. Levin (2002). Anomalous seaward dip of the lithosphere-asthenosphere boundary beneath northeastern USA detected using differential-array measurements of Rayleigh waves, *Geophys. J. Int,* 149, *414-422.*

Mokhtar, T. and M. Al-Saeed (1994). Shear wave velocity structures of the Arabian Peninsula, *Tectonophysics,* 230, 105-125.

Mooney, W., M. Gettings, H. Blank and J. Healy (1985). Saudi Arabian seismic refraction profile: a traveltime interpretation of crustal and upper mantle structure, *Tectonophysics,* 111, 173-246.

Owens, T.J., G. Zandt and S.R. Taylor (1984). Seismic evidence for an ancient rift beneath the Cumberland Plateau, Tennessee: A detailed analysis of broadband teleseismic P waveforms, *J. Geophys. Res.,* 89, 7783-7795.

Owens, T. J., Nyblade, A. A., Gurrola, H., and Langston, C. A.(2000). Mantle transition zone structure beneath Tanzania, East Africa, *Geophys. Res. Lett.,* 27, 827-830.

Owens, T. J.(1987). Crustal structure of the Adirondacks determined from broadband teleseismic waveform modeling, *J. Geophys. Res.*, 92, 6391-6401.

Owens, T. J., S. R. Taylor, and G. Zandt (1987). Crustal structure at regional seismic test network stations determined from inversion of broadband teleseismic P waveforms, *Bull. Seism. Soc. Am.,* 77, 631-632.

Özalaybey, S., M. K. Savage, A. F. Sheehan, J. N. Louie and J. N. Brune (1997). Shear-wave velocity structure in the northern basin and range province from the combined analysis of receiver functions and surface waves, *Bull. Seismol. Soc. Am.*, 87, 183-189.

Park, Y., A. Nyblade, A. Rodgers and A. Al-Amri (2005). Tomographic Imaging of Upper Mantle P and S-wave Velocity Heterogeneity Beneath the Arabian Peninsula. UCRL-TR-214906.

Ritsema, J., H. J. van Heijst, J. H. Woodhouse (1999). Complex shear wave velocity structure beneath Africa and Iceland, *Science,* 286, 1925-1928.

Randall, G.(1994). Efficient calculation of complete differential seismograms for laterally homogeneous earth models, *Geophys. J. Int.,* 118, 245-254.

Rodgers, A., and S.Y. Schwartz (1998). Lithospheric structure of the Qiangtang Terrane, northern Tibetan Plateau, from complete waveform modeling: evidence for partial melt, *J. Geophys. Res.*, 103, 7137-7152.

Rodgers, A., Walter, W., Mellors, R., Al-Amri, A. and Y. Zhang (1999). Lithospheric structure of the Arabian Shield and Platform from complete regional waveform modeling and surface wave group velocities, *Geophys. J. Int.*, 138, 871-878.

Rodgers, A., A. Al-Amri, A. Ar-Rajehi, T. Al-Khalifah, M. Al-Amri, M. Al-Haddad and N. Al-Arifi (2001). Analysis of regional travel time data from the November 1999 Dead Sea explosions

observed in Saudi Arabia, Lawrence Livermore National Laboratory Informal Document, UCRL-ID-138770.

Rodgers, A,. Tkalcic, A., Nyblade, A., Park, A., Schwartz, S., and Hansen, S., (2005). Upper mantle structure beneath the Arabian Shield and Red Sea. Unpublished report. LLNL.

Rodgers, A. J., D. Harris, S. Ruppert, J. P. Lewis, J. O'Boyle, M. Pasyanos, A. Q. Fandi Abdallah, T. Al-Yazjeen and A. Al-Gazo (2003a). A broadband seismic deployment in Jordan, *Seism. Res. Lett.*, 74, 374-381.

Sandvol, E., D. Seber, M. Barazangi, F. Vernon, R. Mellors, and A. Al-Amri (1998). Lithospheric seismic velocity discontinuities beneath the Arabian Shield, *Geophys. Res Lett.*, 25, 2873-2876.

Sandvol, E., Ni, J., Ozalaybey, S., and J. Schlue (1992). Shear-wave splitting in the Rio Grande Rift, *Geophys. Res. Lett.*, 19, 2337-2340.

Sandvol, E., D. Seber, A. Calvert and M. Barazangi (1998). Grid search modeling of receiver functions: Implications for crustal structure in the Middle East and North Africa, *J. Geophys. Res.*, *103*, 26,899-26,917.

Savage, M. K., Silver, P.G., and R.P. Meyer (1990). Observations of teleseismic shear wave splitting in the Basin and Range from portable and permanent stations. *Geophys.Res. Lett.* 17, 21-24.

Schilling, J., R. Kingsley, B.Hanan, and B. McCully (1992). Nd-Sr-Pb isotopic variations along the Gulf of Aden: evidence for Afar mantle plume – continental lithosphere interaction, *Journal of Geophysical Research,* 97, 10,927-10,966.

Schmid, C., S. van der Lee and D. Giardini (2004). Delay times and shear wave splitting in the Mediterranean region, *Geophysical Journal International*, 159, 275-290.

Schmidt, D.L., D. G. Hadley, and D. B. Stoeser (1979). Late Proterozoic crustal history of the Arabian Shield, southern NaJd province, Kingdom of Saudi Arabia, evolution and mineralization of the Arabian-Nubian Shield, *I.A.G. Bull.*, 3, 41-58.

Schwartz, S. Y., Rodgers, A. and S. Russell (2000). Crustal and upper mantle structure beneath northeast Africa and the Red Sea Rift Zone, Institute of Geophysics and Planetary Physics-Lawrence Livermore National Laboratory 2000 Annual Report, F. J. Ryerson, K.H. Cook, and J. Tweed editors.

Seber, D., M. Vallve, E. Sandvol, D. Steer and M. Barazangi (1997). Middle East tectonics: applications of geographical information systems (GIS), *GSA Today,* February 1997, 1-5.

Shen, Y., S.C. Solomon, I. Bjarnason, and C. Wolfe (1998). Seismic evidence for a lower-mantle origin of the Iceland plume, *Nature,* 395, 62-65.

Silver, P., and W. Holt (2002). The Mantle Flow Field Beneath Western North America, *Science,* 295, 1,054-1,057.

Sodoudi, F.(2005). Lithospheric structure of the Aegean obtained from P and S receiver functions. *PhD Thesis*, Freie Universitat Berlin .
Stern, R. (1994). Arc assembly and continental collision in the neoproterozoic east African orogen: Implications for the consolidation of Gondwanaland, *Annual Reviews in Earth Planetary Sciences*, 22, 319-351.

Stoeser, D., and V. Camp (1985). Pan-African microplate accretion of the Arabian Shield, *Geological Society of America Bulletin*, 96, 817-826.

Thurber, C.H.(1983). Earthquake locations and three-dimensional crustal structure in the Coyote Lake area, central California, *J. Geophys. Res.*, 88, 8226-8236.

Tkalcic, H; M. Pasyanos,; A. Rodgers, A., R Gok, W. Walter and A. Al-Amri (2005). A multi-step approach in joint modeling of surface wave dispersion and teleseismic receiver functions: Implications for lithospheric structure of the Arabian Peninsula, UCRL-TR-214906.

Tkalčić, H., M. Pasyanos, A. Rodgers, R. Gök, W. Walter, A. Al-Amri, and A. Al-Enezi, A. (2005). Lithospheric structure of the Arabian Peninsula from Joint Inversion of Teleseismic Receiver Functions and Surface Waves, *EOS Transactions AGU, 86(52)*, Fall Meeting Supplemental, T13A-0449.

VanDecar, J. C.(1991). Upper mantle structure of the Cascadia subduction zone from non-linear teleseismic travel time inversion, Ph.D. thesis, Univ. of Wash., Seattle.

VanDecar, J. C., and R. S. Crossen (1990). Determination of teleseismic relative phase arrival times using multi-channel cross-correlation and least-squares, *Bull. Seismol. Soc. Am.*, 80, 150-161.

Vernon, F. and J. Berger (1997). Broadband seismic characterization of the Arabian Shield, Final Scientific Technical Report, Department of Energy Contract No. F 19628-95-K-0015, 36 pp.

Vernon, F., R. Mellors, J. Berger, A. Edelman, A. Al-Amri, J. Zollweg, and C. Wolfe (1996). Observations from regional and teleseismic earthquakes recorded by a deployment of broadband seismometers in the Saudi Arabian Shield, *Eos Trans, AGU*, 77, 46, 478.

Vinnik, L.P., L.I. Makeyeva, A. Milev, and A. Y. Usenko (1992). Global patterns of azimuthal anisotropy and deformations in the continental mantle, *Geophys. J. Int.*, 111, 433-447.

Wolfe, C. J., F. L. Vernon, and A. Al-Amri (1999). Shear-wave splitting across western Saudi Arabia: The pattern of mantle anisotropy at a Proterozoic shield, *Geophys. Res. Lett.*, 26, 779-782.

GLOSSARY

المصطلحات اللاتينية وترجمتها العربية

Arabian Plate	الصفيحه العربيه
Arabian Platform	الرصيف العربي
Arabian Shield	الدرع العربي
Asthenosphere	الغلاف الوهن
Azimuth	الإتجاه الزاوي
Broadband Stations	محطات واسعة المدى
Correlation Coefficient	معامل المضاهاه
Crustal Structure	التركيب القشري
Crustal Thickness	السمك القشري
Comprehensive Test Ban Treaty Organization (CTBTO)	منظمة معاهدة حظر التجارب النوويه الشامل
Delay Time	زمن التأخير
Epicenter	المركز السطحي للزلزال
Focal Mechanism Solutions	حلول ميكانيكية البؤرة
Fast Polarization	الإستقطاب السريع
Focal Depth	العمق البؤري
Group Velocities	السرع الجماعية
International Association of Seismology & Physics of the Earth (Iasp91)	نموذج حساب معدل السرعه
Frequency	التردد
Latitude (N)	خط العرض
Layer	طبقه
Lithosphere	الغلاف الصخري
Long period Spectral Ratios	نسب السعه العموديه للموجات الطوليه
Long Period Station	محطة رصد ذات فتره دوريه طويلة المدى
Longitude (E)	خط الطول
Lower Crust	القشره السفلي
Magnitude	القدر الزلزالي
Mantle	الوشاح (لحاء)
Miocene	فترة الميوسين
Moho Discontinuity	إنقطاع موهو
Monthly Listing	النشرة الزلزاليه الشهريه

Neotectonic	البنيه الحديثه
Observatory	مرصد
Origin Time	زمن حدوث الزلزال عند البؤره
Preliminary Determination of Epicenters (PDE)	التحديد المبدئي لمراكز الزلازل
Plate Tectonics	حركة الصفائح
Polar Projection	إسقاط قطبي
Primary Wave Velocity (Vp)	سرعة الموجات الطوليه
Quaternary	العصر الرابع
Receiver Function	دالة المستقبل
Response Curve	منحني الإستجابه
Review Events Bulletin (REB)	نشرة الأحداث المراجعه
Rock Density	الكثافه الصخريه
SANDSN	الشبكه السعودية الوطنيه الرقمية للزلازل
Seismic Analysis Code (SAC)	كود التحليل الزلزالي
Seismic Attenuation	التعتيم الزلزالي
Seismic Hazards	خطر زلزالي
Seismic Noise	الضوضاء السيزميه
Seismic Tomography	زلزالية ثلاثية الأبعاد
Seismic Waves	الموجات الزلزاليه
Seismogram	سجل زلزالي
Shear Wave Velocity (Vs)	سرعة موجات القص
Shear Wave Splitting	فصل موجات القص
Spectral Amplitude	السعة الطيفيه
Spectral Analysis	التحليل الطيفي
Surface Wave dispersion	تشتت الموجة السطحي
Surficial Sediments	رواسب سطحيه
Synthetic Waveform	الشكل الموجي المركب
Take-off Angle	زاوية خروج الشعاع عند بؤرة الزلزال
Teleseismic Earthquakes	الزلازل البعيده
Tertiary	العصر الثالث
Theoretical Spectral Rations	النسب الطيفيه النظريه
Thickness	السماكه
Transition Zone	منطقة إنتقاليه
Travel Times	أزمنة المسار
Upper Crust	القشره العلويه
Wave Propagation	الإنتشار الموجي
Waveform Modeling	نمذجة الشكل الموجي